

# Numerical Simulations of Three-Dimensional Instabilities in Cavity Flows

Thesis by  
Guillaume A. Brès

In Partial Fulfillment of the Requirements  
for the Degree of  
Doctor of Philosophy



California Institute of Technology  
Pasadena, California

2007

(Defended April 13, 2007)

© 2007

Guillaume A. Brès

All rights Reserved

## Acknowledgements

First, I would like to thank my advisor, Prof. Tim Colonius, for his support and guidance throughout my studies at Caltech. I am truly grateful to him, and to all the members of the Computational Flow Physics Group, for their help and invaluable contributions to this work. In particular, I want to mention my fellow graduate students Eric Johnsen and Kunihiro (Sam) Taira, who showed great patience in so many productive discussions, and the “masters” of the Beowulf clusters, Jeff Krimmel and Jennifer Franck.

It is hard to believe that this has been almost five years in the making. It may seem like a long time, but it really did not feel like it. One might say that there are two different time scales in the flow of a Ph.D. thesis. I simply think that this has a lot to do with a group of great friends who made Caltech and Los Angeles such truly enjoyable places. I want to express my appreciation to all of them and especially thank my dear friends Lisa Goggin, Alan Hampton, Hannes Helgason, Corinne Ladous, and Angel Ruiz Angulo.

I would also like to thank Guillaume “Pom” Marche and all my childhood friends from Montréal, Alexandre Garneau, and Les Centraliens, Matthieu de Linares, Eric d’Hanens and Damien Micheneau. Having lived so far away, for so long, I cannot be grateful enough for their lasting friendship.

Finally, I could not have come this far without the constant love and support of my family, to whom this thesis is dedicated.

# Numerical Simulations of Three-Dimensional Instabilities in Cavity Flows

by

Guillaume A. Brès

In Partial Fulfillment of the  
Requirements for the Degree of  
Doctor of Philosophy

## Abstract

Direct numerical simulations are performed to investigate the stability of compressible flow over three-dimensional open cavities for future control applications.

First, the typical self-sustained oscillations, commonly referred as “shear-layer (Rossiter) modes,” are characterized for two-dimensional cavities over a range of flow conditions. A linear stability analysis is then conducted to search for three-dimensional global instabilities of the 2D mean flow for cavities that are homogeneous in the spanwise direction. The presence of such instabilities is reported for a range of cavity configurations. For cavities of aspect ratio (length to depth) of 2 and 4, the three-dimensional mode has a spanwise wavelength of approximately 1 cavity depth and oscillates with a frequency about one order of magnitude lower than two-dimensional Rossiter (flow/acoustics) instabilities. A steady mode of smaller spanwise wavelength is also identified for square cavities. The linear results indicate that the instability is hydrodynamic (rather than acoustic) in nature and arises from a generic centrifugal instability mechanism associated with the mean recirculating vortical flow in the downstream part of the cavity. These three-dimensional instabilities are related to centrifugal instabilities reported in flows over backward-facing steps, lid-driven cavity flows, and Couette flows.

Results from three-dimensional simulations of the nonlinear compressible Navier–Stokes equations are also reported. The formation of oscillating (and, in some

cases, steady) spanwise structures is observed inside the cavity. The spanwise wavelength and oscillation frequency of these structures agree with the linear analysis predictions. When present, the shear-layer (Rossiter) oscillations experience a low-frequency modulation that arises from nonlinear interactions with the three-dimensional mode. These results are consistent with observations of low-frequency modulations and spanwise structures in previous experimental and numerical studies on open cavity flows.

# Contents

<b>1</b>	<b>Introduction</b>	<b>1</b>
1.1	Motivation and review of previous work . . . . .	1
1.1.1	Rossiter mode . . . . .	1
1.1.2	Wake mode . . . . .	3
1.1.3	Self-sustained versus forced oscillations . . . . .	4
1.1.4	Flow control . . . . .	4
1.1.5	Three-dimensionality in cavity flow . . . . .	5
1.2	Overview of present work . . . . .	7
<b>2</b>	<b>Numerical Methods and Stability Theory</b>	<b>10</b>
2.1	Direct numerical simulations . . . . .	10
2.2	Linear stability theory . . . . .	15
2.3	Residual method and L2 fitting routines . . . . .	16
2.4	ARPACK . . . . .	17
2.5	Validation . . . . .	19
<b>3</b>	<b>Linear Stability Results</b>	<b>21</b>
3.1	Two-dimensional simulations . . . . .	21
3.1.1	Shear-layer mode . . . . .	22
3.1.2	Neutral stability curves . . . . .	26
3.2	Three-dimensional linear stability . . . . .	31
3.2.1	Three-dimensional mode properties . . . . .	31
3.2.2	Parameter dependence . . . . .	33

3.2.3	Eigenmode structure . . . . .	39
<b>4</b>	<b>Centrifugal Instability</b>	<b>43</b>
4.1	Instability mechanism . . . . .	43
4.1.1	Rayleigh's circulation criterion . . . . .	43
4.1.2	Rayleigh discriminant . . . . .	44
4.2	Connection with other centrifugal instabilities . . . . .	47
4.2.1	Flow past a backward-facing step . . . . .	47
4.2.2	Lid-driven cavity flows . . . . .	48
4.2.3	Couette flow . . . . .	49
<b>5</b>	<b>Nonlinear Three-Dimensional Simulations</b>	<b>54</b>
5.1	Subcritical conditions . . . . .	55
5.1.1	3D mode oscillation . . . . .	55
5.1.2	Flow structure . . . . .	55
5.1.3	Time-averaged flow . . . . .	58
5.2	Supercritical conditions . . . . .	60
5.2.1	Unsteady flow structure . . . . .	60
5.2.2	Oscillation frequencies . . . . .	62
5.2.3	Shear-layer spreading rate . . . . .	66
5.2.4	Time-averaged flow properties . . . . .	68
5.2.5	Discussion of the change in oscillation frequency . . . . .	73
5.3	Multiple three-dimensional modes . . . . .	76
5.3.1	Oscillation frequencies . . . . .	76
5.3.2	Evidence of the steady three-dimensional mode . . . . .	80
5.3.3	Time-averaged flow . . . . .	80
<b>6</b>	<b>Connection with Previous Experimental and Numerical Results</b>	<b>83</b>
6.1	General remarks on cavity flow experiments . . . . .	83
6.2	Interpretation of low-frequency modulation in experiments . . . . .	86
6.2.1	Water channel experiments . . . . .	88

6.2.2	Moderate Mach number experiments . . . . .	89
6.3	Visual evidence of the three-dimensional mode . . . . .	90
6.4	Connection with previous numerical simulations . . . . .	94
6.4.1	Large eddy simulations . . . . .	94
6.4.2	Proper orthogonal decomposition results . . . . .	95
<b>7</b>	<b>Concluding Remarks</b>	<b>97</b>
7.1	Summary . . . . .	97
7.2	Potential applications for flow control . . . . .	99
<b>A</b>	<b>Simulation Parameters</b>	<b>101</b>
<b>B</b>	<b>Linear Stability Experiments</b>	<b>106</b>
B.1	Influence of the Mach number . . . . .	107
B.2	Influence of the Reynolds number . . . . .	108
<b>C</b>	<b>Extension of the Linear Stability to Supercritical Conditions</b>	<b>111</b>
C.1	Two-dimensional simulation of Rockwell experiment . . . . .	111
C.2	Linear stability results . . . . .	115
<b>D</b>	<b>Preliminary Results on 3D Wake Mode</b>	<b>119</b>
D.1	Two-dimensional wake mode . . . . .	119
D.2	Three-dimensional simulations . . . . .	122
D.2.1	Flow field without spanwise disturbances . . . . .	122
D.2.2	Flow field with spanwise disturbances . . . . .	125

## List of Figures

1.1	Schematic of open cavity oscillations in compressible flows . . . . .	2
2.1	Basic configuration of the computational domain . . . . .	13
2.2	Visualisation of the computational grid . . . . .	14
2.3	Comparison of linear stability result with ARPACK solution . . . . .	19
3.1	Vorticity field for run 2M06 (shear-layer mode) . . . . .	23
3.2	Velocity field for run 2M06 (shear-layer mode) . . . . .	24
3.3	Acoustic field for run 2M06 (shear-layer mode) . . . . .	25
3.4	Vorticity contours and streamlines of the 2D steady base flow for different cavity aspect ratios . . . . .	26
3.5	Neutral stability curve and oscillation frequencies for run series H1	27
3.6	Neutral stability curve and oscillation frequencies for run series 2M	28
3.7	Neutral stability curve and oscillation frequencies for run series TK2	29
3.8	Neutral stability curve and oscillation frequencies for run series TK4	30
3.9	Long-time linear response of the cavity to 3D perturbations of dif- ferent spanwise wavelengths for run 2M0325 . . . . .	32
3.10	3D linear stability results for run series 2M . . . . .	34
3.11	3D linear stability results for run series TK2M . . . . .	35
3.12	3D linear stability results for run series H1 . . . . .	36
3.13	Vorticity contours for 2D steady and time-averaged base flows . . . . .	38
3.14	Visualisation of the unstable eigenfunction of spanwise wavelength $\lambda/D = 1$ for the 3D linear run 2M0325 . . . . .	41

3.15	3D visualisation of the flow for the unstable mode of spanwise wavelength $\lambda/D = 1$ for the 3D linear run 2M0325 . . . . .	42
4.1	Streamlines and Rayleigh discriminant of 2D steady and time-averaged base flows . . . . .	45
4.2	Properties of the 2D steady base flow in run H1Re140 for comparison with Couette flow . . . . .	51
5.1	Time trace of normal velocity for runs 2M0325 and 2M0325-3D . . .	57
5.2	Spectrum of the normal velocity for runs 2M0325 and 2M0325-3D . .	57
5.3	Spanwise velocities for run 2M0325-3D . . . . .	59
5.4	Time-averaged velocity field for runs 2M0325 and 2M0325-3D . . . .	60
5.5	Spanwise velocities for run 2M06-3D . . . . .	61
5.6	Time trace of streamwise velocity for runs 2M06 and 2M06-3D . . .	63
5.7	Time trace of pressure for runs 2M06 and 2M06-3D . . . . .	63
5.8	Time trace of spanwise velocity for run 2M06-3D . . . . .	64
5.9	Power spectra of the streamwise velocity and pressure for runs 2M06 and 2M06-3D . . . . .	65
5.10	Power spectra of the spanwise velocity for run 2M06-3D . . . . .	66
5.11	Shear-layer spreading rates . . . . .	67
5.12	Reynolds stresses $\sqrt{u'u'}/U$ , $\sqrt{v'v'}/U$ , and $\sqrt{w'w'}/U$ for runs 2M06 and 2M06-3D . . . . .	69
5.13	Reynolds stress $\overline{u'v'}/U^2$ for runs 2M06 and 2M06-3D . . . . .	70
5.14	2D time-averaged velocity field for runs 2M06 and 2M06-3D . . . . .	71
5.15	Sound pressure levels for runs 2M06 and 2M06-3D . . . . .	72
5.16	Vorticity fields for run 2M0325-3D . . . . .	74
5.17	Vorticity fields for run 2M06-3D . . . . .	75
5.18	Time trace of streamwise velocity for runs H1Re300 and H1Re300-3D	77
5.19	Power spectra of the streamwise velocity for runs H1Re300 and H1Re300-3D . . . . .	77
5.20	Time trace of spanwise velocity for run H1Re300-3D . . . . .	79

5.21	Power spectra of the spanwise velocity for run H1Re300-3D . . . . .	79
5.22	Spanwise velocities for run H1Re300-3D . . . . .	81
5.23	Time-averaged velocity and vorticity field for run H1Re300-3D . . . . .	82
6.1	Experimental visualisation of the spanwise structures by Rockwell & Knisely (1980) . . . . .	85
6.2	Visualisation of the slot cavitation by Ward (1973) . . . . .	87
6.3	Flow types in the slot cavitation experiment by Ward (1973) . . . . .	88
6.4	Experimental visualisation of the primary vortex by Faure <i>et al.</i> (2007) . . . . .	92
6.5	Experimental visualisation of the spanwise structures by Faure <i>et al.</i> (2007) . . . . .	93
6.6	Visualisation of the spanwise structures for run H1Re300-3D . . . . .	94
C.1	Vorticity fields for run Rkw . . . . .	113
C.2	Time trace at $(x, y) = (0.5L, 0)$ for run Rkw . . . . .	114
C.3	2D time-averaged velocity field for run Rkw . . . . .	115
C.4	Streamlines and Rayleigh discriminant of the 2D time-averaged base flow for run Rkw . . . . .	116
C.5	Schematics of the flow by Rockwell & Knisely (1980) . . . . .	117
D.1	Time trace of the pressure and velocities for run 4M06wake . . . . .	120
D.2	Spectrum of the normal velocity for run 4M06wake . . . . .	121
D.3	Time trace of the drag coefficient for wake and shear-layer mode . . . . .	122
D.4	Time-averaged velocity fields and streamlines for wake and shear- layer modes . . . . .	123
D.5	Evolution of the spanwise vorticity for run 4M06wake-3D . . . . .	124
D.6	Evolution of the vorticity for run 4M06-3D . . . . .	126
D.7	Time trace of the pressure and velocities for run 4M06-3D . . . . .	127
D.8	Time trace of the spanwise velocity for run 4M06-3D . . . . .	127
D.9	Spectrum of the normal and spanwise velocity for run 4M06-3D . . . . .	128

## List of Tables

4.1	Critical conditions of the 3D centrifugal instability for flows over a backward-facing step, lid-driven cavity, Couette, and open cavity flows . . . . .	53
5.1	Comparison of the dominant mode prediction for 2D and 3D runs with $L/D = 2$ . . . . .	56
5.2	Comparison of the dominant mode prediction for 2D and 3D runs with $L/D = 1$ . . . . .	78
A.1	Parameters and stability for the run series H1 . . . . .	102
A.2	Parameters and stability for the run series 2M . . . . .	103
A.3	Parameters and stability for the run series TK2 . . . . .	104
A.4	Parameters and stability for the run series TK4 . . . . .	105
A.5	Parameters and stability for the run series 4M . . . . .	105
B.1	Parametric study of the Mach number influence on the 3D linear stability . . . . .	108
B.2	Parametric study of the Reynolds number influence on the 3D linear stability . . . . .	109

## Nomenclature

### Roman characters

$a$	Speed of sound
$c_p$	Specific heat at constant pressure
$D$	Cavity depth
$e$	Energy
$k$	Thermal conductivity
$L$	Cavity length
$M$	Mach number
$N_x$	Number of computational grid points in the streamwise direction
$N_y$	Number of computational grid points in the normal direction
$N_z$	Number of computational grid points in the spanwise direction
$P$	Pressure
$Pr$	Prandtl number
$\mathbf{q}$	Vector of the conservative variables
$Re$	Reynolds number
$Re_D$	Reynolds number based on $D$
$Re_L$	Reynolds number based on $L$
$Re_\theta$	Reynolds number based on $\theta$
$St_D$	Strouhal number based on $D$
$St_L$	Strouhal number based on $L$
$T$	Temperature
$t$	Time

$U$	Freestream velocity
$u$	Streamwise velocity
$\mathbf{u}$	Velocity vector
$v$	Normal velocity
$w$	Spanwise velocity
$x$	Streamwise direction
$y$	Normal direction
$z$	Spanwise direction

## Greek characters

$\alpha$	Phase delay in Rossiter formula
$\beta$	Spanwise wavenumber
$\gamma$	Ratio of specific heats
$\delta_\omega$	Shear-layer vorticity thickness
$\eta$	Rayleigh discriminant
$\theta$	Shear-layer momentum thickness
$\kappa$	Average convection speed of vortical disturbances in Rossiter formula
$\Lambda$	Spanwise extent of the cavity
$\lambda$	Spanwise wavelength of the 3D instability
$\mu$	Dynamic viscosity
$\nu$	Kinematic viscosity
$\rho$	Density
$\sigma$	Growth/damping rate of the 3D instability
$\chi$	Merit function
$\Omega$	Complex eigenvalue of the 3D instability
$\omega$	Oscillation frequency of the 3D instability
$\omega_z$	Spanwise vorticity
$\boldsymbol{\omega}$	Vorticity vector

## Superscripts

- Time-averaged quantity
- ' Perturbation quantity
- d* Dimensional quantity

## Subscripts

- $\infty$  At infinity
- 0 At initial condition

# Chapter 1

## Introduction

### 1.1 Motivation and review of previous work

From the canonical rectangular cut-out to more complicated shapes with internal structures, resonant cavity instabilities are endemic to a number of aircraft components including weapon bays, landing gear wells, and instrumentation cavities. Self-sustained oscillations and intense acoustic loading inside the cavity can lead to structural damage, optical distortion, and store separation problems. In particular, weapons bay noise suppression has been a major motivation for recent work on cavity flow, including active flow control to replace traditional passive devices such as spoilers, ramps, rakes, etc.

#### 1.1.1 Rossiter mode

Dating back to the early work of Rossiter (1964), cavity oscillations in compressible flow are typically described as a flow-acoustic resonance mechanism, as shown in figure 1.1: small instabilities in the shear layer interact with the downstream corner of the cavity and generate acoustic waves, which propagate upstream and create new disturbances in the shear layer. For incompressible flow, the upstream influence is instantaneous, while there is an acoustic delay for compressible flow. Resonance occurs at a given frequency when the disturbances lead to reinforcement and ultimately saturation. This type of instability is referred to as shear-layer (or

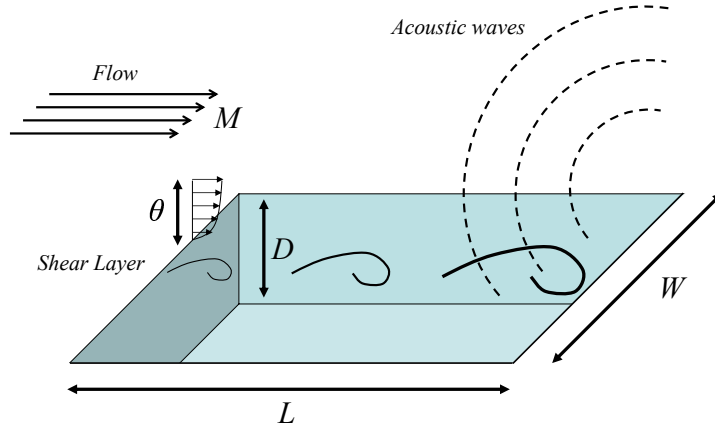


Figure 1.1: Schematic of open cavity oscillations in compressible flows

Rossiter) mode, and can be distinguished from pure acoustic resonance where frequency selection depends only on the sound speed and geometrical parameters.

Rossiter (1964) performed an extensive set of experiments for two-dimensional rectangular cavities of different length to depth ratio, at different Mach numbers, which identified a series of discrete frequencies of oscillation. He used the idea of the feedback process to develop a semi-empirical formula to predict the resonant frequencies:

$$St_n = \frac{f_n L}{U} = \frac{n - \alpha}{M + \frac{1}{\kappa}} \quad n = 1, 2, 3, \dots \quad (1.1)$$

where  $St_n$  is the Strouhal number corresponding to the  $n$ -th mode frequency,  $f_n$ . The empirical constants  $\kappa$  and  $\alpha$  correspond to the average convection speed of the vortical disturbances in the shear layer, and a phase delay (typically  $1/\kappa = 1.75$  and  $\alpha = 0.25$ ), respectively.

Data from a large number of experiments and simulations over the years show reasonable agreement with equation 1.1, but with significant scatter. The scattering is mainly due to the discrepancies between experimental conditions, as different cavity and flow parameters ( $L/D$ ,  $L/\theta_0$ ,  $Re_\theta$ ) were used. These parameters

can have a significant influence on the resonant frequencies and do not appear in Rossiter’s formula. Additionally, equation 1.1 does not give any indication of whether such self-sustained oscillations do occur and, if so, which of several possible modes are present and if a particular mode (if any) is dominant.

### 1.1.2 Wake mode

Apart from the instability mechanism proposed by Rossiter, other modes of oscillation have been observed in cavity flows. In their incompressible experiment for an axisymmetric cavity, Gharib & Roshko (1987) observed a significant change in the behavior of the cavity oscillation when the ratio of the cavity length relative to the upstream boundary layer momentum thickness was increased. Direct numerical simulations by Rowley *et al.* (2002*b*) showed similar results for a two-dimensional rectangular cavity. In this mode, the flow is characterized by a large-scale vortex shedding from the cavity leading edge, similar to that observed behind bluff bodies, hence the term “*wake mode*” used to describe the resulting flow regime. As the large vortex (dimension of the cavity depth) forms near the leading edge, free stream fluid enters the cavity and impinges on the cavity bottom. The vortex is then shed from the leading edge and is violently ejected from the cavity, the all process resulting in a drastic increase in drag.

The wake mode transition has been observed in several two-dimensional numerical simulations (e.g., Fuglsang & Cain, 1992; Cain *et al.*, 2000; Rowley *et al.*, 2002*b*; Larsson *et al.*, 2004), but experimental evidence of this mode is fairly limited. Three-dimensionality has been shown to play a role in suppressing the wake mode. Large eddy simulations by Shieh & Morris (2000) showed that two-dimensional cavities in wake mode return to shear-layer mode when three-dimensional disturbances are present in the incoming boundary layer. Similarly, recent work by Suponitsky *et al.* (2005) showed that the development of a three-dimensional flow field, generated by the introduction of the random inflow disturbance into a two-dimensional cavity oscillating in wake mode, yielded the transition to the shear-layer mode, regardless of the amplitude and shape of the inflow disturbance. These studies

highlight how a better understanding of the fundamental three-dimensional features of cavity flows is crucial to accurately connect numerical results, experiments and practical applications.

### 1.1.3 Self-sustained versus forced oscillations

There are additional acoustic resonances of typical cavity geometries that lead, especially at lower Mach numbers and in confined laboratory experiments (e.g., wind tunnel resonance) to additional complications in the identification of cavity resonance mechanisms. Purely acoustic resonance can lead to a “detuning” and/or reinforcement of the flow/acoustic shear layer modes. Rowley *et al.* (2006) showed that oscillations observed in experiments are not always of the self-sustaining type envisioned by Rossiter . Indeed, in many cases it appears that the cavity oscillations are actually forced by boundary layer turbulence or other external sources of noise. This clarification has major implications for the design of feedback controllers (e.g., Rowley *et al.*, 2002*a*). Recent models by Alvarez *et al.* (2004; 2005) showed that there can be strong interactions with wind tunnel resonances, and confirm analytically that oscillations are not always self-sustaining.

### 1.1.4 Flow control

Over the past decades, two-dimensional cavity flows have received significant attention (see for instance review articles from Rockwell & Naudascher, 1978; Colonius, 2001; Rowley & Williams, 2006), including several experimental and numerical studies at the California Institute of Technology (e.g., Krishnamurty, 1956; Sarohia, 1975; Gharib, 1983; Rowley, 2001). Aside from numerical benchmarking, the main motivations for studying cavity flow are noise reduction and flow control. Fundamental research has been conducted recently to examine how active (open and closed-loop) flow control can be use to replace traditional passive devices such as spoilers, ramps and rakes (e.g., Cattafesta III *et al.*, 1999; Alvarez *et al.*, 2004; Rowley *et al.*, 2006; Rowley & Williams, 2006). Model-based closed-loop control, in particular, promises efficient (low energy input) tone suppression, while passive

devices may be more effective for broadband noise reductions.

In analyzing the behavior of the shear layer oscillations, most investigators have implicitly assumed that the shear layer behavior can be described in isolation, i.e., as if it were a free shear layer. In recent refinements to this model, Alvarez *et al.* (2004; 2005) have developed linear theory that couples the shear layer dynamics and acoustic behavior of the cavity (essentially using an unsteady Kutta condition at the cavity leading and trailing edges), but non-parallel shear layer effects and, in particular, the coupling of the flow inside the cavity have not been studied.

An alternative analysis of the global instability modes is to consider the basic, steady flow as two- or even three-dimensional. This viewpoint requires high-fidelity steady flow solutions of the Navier-Stokes equations as input, and then solves a partial-derivative eigenvalue problem for 2D and 3D instabilities of the basic flow. The underlying theory and methodology for extracting these bi- and tri-global instabilities are described by Theofilis (2003) in a recent review paper. Early efforts have concentrated on incompressible flows, including backward-facing step, lid-driven cavities, laminar separation bubbles, etc. A significant accomplishment of the present work has been to extend this effort to compressible flows where in many cases (including the cavity) small amplitude acoustic radiation is an important aspect of the instabilities and must be treated with high-order-accurate numerics in order to avoid spurious oscillations or numerical dissipation of the relevant instabilities.

### 1.1.5 Three-dimensionality in cavity flow

Recently, some aspects of the three-dimensional cavity flow have been investigated using Large Eddy Simulation (LES) methods (Rizzetta & Visbal, 2003; Larchevêque *et al.*, 2004; Chang *et al.*, 2006) and Proper Orthogonal Decomposition (POD) (Podvin *et al.*, 2006). These studies have been mainly focused on the frequencies of oscillation and coherence of the (two-dimensional) Rossiter modes, and the extent to which there is agreement with experimental measurements of

mean flow and spectra. Some observations regarding the three-dimensionality of the large-scale turbulent structures are also reported but do not figure prominently in these studies. Such LES data could be useful in future to examine the instabilities identified in this study at higher values of Reynolds number.

Likewise, three-dimensional experimental data is fairly limited but several researchers have reported observations of three-dimensionality in cavity flows. Ahuja & Mendoza (1995) conducted an extensive set of experiments on the effect of cavity dimensions, boundary layer, and temperature on cavity noise for subsonic flows with turbulent boundary layer upstream of the cavity. They determined that the parameter  $L/W$ , the cavity length to width ratio, provided a transition between two- and three-dimensional flow. For  $L/W < 1$ , the cavity is classified as two-dimensional, as the flow was found to be uniform over much of the span, with a coherent shear layer spanning most of the cavity width. The cavity is said to be three-dimensional for  $L/W > 1$ , as the flow cannot maintain a coherent shear layer across its width because of the end-effects that cause significant spillage of flow over the cavity side into the cavity. In that case, they reported three-dimensionality in the mean flow, and much lower (about 15 dB) acoustic loads than the predominately two-dimensional flow. However, Ahuja and Mendoza's classification of wide cavities as two-dimensional is based on a time-averaged view of the flow field, and the three-dimensionality is not related to the 3D instability we identify in our present work.

Three-dimensional flow features have also been observed for wide cavities in early wind tunnel experiments at low subsonic velocities by Maull & East (1963). Using oil flow visualisation of surface streamlines at the bottom of the cavity and surface static-pressure distributions, they showed the existence, under certain conditions, of nearly steady spanwise cellular pattern within the cavity. They observed that the width of each cell remained essentially independent of the total cavity span but that the most regular pattern existed when the cavity span was an integral number of preferred cell-width. Rockwell & Knisely (1980) also observed three-dimensional pattern in a water channel experiment for a wide rectangular

cavity with laminar boundary layer upstream. A hydrogen bubble technique was used to visualise the spanwise structure in the cavity. More evidence of three-dimensional structures in cavity flows have been presented in the recent work of Faure *et al.* (2007). The physics of these features has yet to be fully understood.

In conclusion, while observations of three-dimensionality in cavity flow have been reported, the physics of these features has yet to be fully understood. As a result, past efforts on cavity flow control have typically ignored non-parallel and three-dimensional effects. These approaches may, on one hand, reduce the effectiveness of model-based control, or on the other hand disregard important three-dimensional mechanisms that could be exploited in passive ways to reduce broadband noise.

## 1.2 Overview of present work

The focus of the present work is therefore to characterize the basic instabilities of three-dimensional open cavity flows. Because the basic (steady or time-averaged) cavity flow is complex and non-parallel, our stability analysis is focused on extracting global instabilities from Direct Numerical Simulations (DNS) of the full and linearized compressible Navier–Stokes equations.

From the start, it must be acknowledged that accurate computation of realistic, unsteady, three-dimensional aircraft cavities, at realistic flight Reynolds numbers, is well beyond current computer resources. While realizable parameter regimes (especially small scale experiments) may be reached with LES, such computations are sufficiently time consuming that they prohibit a significant portion of parameter space from being investigated. By focusing our attention on low Reynolds number direct numerical simulations of 2D and 3D spanwise periodic flows, we are able to examine a large parameter space (Mach number, cavity dimensions, boundary layer thickness). In inflectional shear layers, the instabilities of compressible flows are inviscid. This observation has led, for example, to modeling of two-dimensional

shear layer oscillations in cavity flows using inviscid parallel flow stability. Models and computations at low Reynolds numbers display the same instabilities as the inviscid analysis.

As we show that the principle effect of the Reynolds number is to damp the instabilities, any instabilities observed here are likely to be at play at full-scale Reynolds numbers. Thus the low Reynolds number analysis and simulations can bracket the behaviors that exist in experiments and flight conditions, and at the same time understand in detail the instabilities and their parametric variations. In general, simulations of simpler (even two-dimensional) flows can lead to insights into the flow physics that directly carry over to full-scale complex flows, and provide data for control and modeling efforts.

In the present work, we consider two- and three-dimensional instabilities to basic cavity flows that are homogeneous in the spanwise direction, for low to moderate Reynolds numbers. Chapter 2 gives an overview of the numerical methods and the linear stability theory used in this study.

First, the onset of two-dimensional cavity instability is characterized as a function of Reynolds number, Mach number, cavity aspect ratio, and incident shear-layer thickness. The two-dimensional modes are consistent, both in terms of oscillation frequency and eigenfunction structure with the typical Rossiter flow/acoustic resonant modes that have been observed in many cavity experiments and flight tests. For basic cavity flows that are two-dimensionally stable, we then search for three-dimensional instabilities of the steady base flow, and identify, for the first time, the presence of such instabilities. The 2D and 3D modes, and their properties, are discussed in chapter 3.

For cavity length-to-depth ratios of 1, 2, and 4 considered here, the instability appears to arise from a generic centrifugal instability mechanism associated with the *internal* recirculation vortical flow that occupies the downstream part of the cavity. The three-dimensional instabilities are related to centrifugal instabilities reported in flows over backward-facing steps, lid-driven cavity flows, and Couette flows. The instability mechanism is presented in chapter 4.

A few selected three-dimensional numerical simulations of the full compressible Navier–Stokes equations are then performed. To our knowledge, this is the first time that strict DNS of three-dimensional compressible cavity flows have been reported. The results, in chapter 5, exhibit three-dimensional features in good agreement with the linear analysis predictions, both in terms of spanwise structures and oscillation frequencies.

In chapter 6, we discuss the connections between the 3D instabilities we report here and observations of three-dimensionality in previous numerical studies and experiments. Our numerical results are consistent with low-frequency modulations and spanwise structures reported in previous studies on open cavity flows. In particular, visual evidence of the 3D mode is found in recent low Reynolds number experiments.

## Chapter 2

# Numerical Methods and Stability Theory

### 2.1 Direct numerical simulations

Following previous work of Rowley *et al.* (2002b) on cavity flows, we develop a DNS code to solve the full compressible Navier–Stokes (NS) equations and study the flow over three-dimensional open cavities. The equations are solved directly, meaning that no turbulence model is used and all the scales of the flow are resolved. The Navier–Stokes equations are written in conservative form as follows:

$$\begin{aligned}
 \frac{\partial \rho}{\partial t} + \frac{\partial}{\partial x_j}(\rho u_j) &= 0 \\
 \frac{\partial \rho u_i}{\partial t} + \frac{\partial}{\partial x_j}(\rho u_i u_j + P \delta_{ij}) &= \frac{1}{Re} \frac{\partial}{\partial x_j} \left( \frac{\partial u_i}{\partial x_j} + \frac{\partial u_j}{\partial x_i} - \frac{2}{3} \frac{\partial u_k}{\partial x_k} \delta_{ij} \right) \\
 \frac{\partial e}{\partial t} + \frac{\partial}{\partial x_j}((e + P)u_j) &= \frac{1}{Re} \frac{\partial}{\partial x_j} \left( u_i \left( \frac{\partial u_i}{\partial x_j} + \frac{\partial u_j}{\partial x_i} - \frac{2}{3} \frac{\partial u_k}{\partial x_k} \delta_{ij} \right) \right) + \frac{1}{Re} \frac{1}{Pr} \frac{\partial^2 T}{\partial x_k \partial x_k}
 \end{aligned} \tag{2.1}$$

with the equation of state

$$P = \frac{\gamma - 1}{\gamma} \rho T,$$

where  $\rho$ ,  $P$ , and  $T$  are the density, pressure, and temperature, and  $u_i$  is the velocity in the direction of the Cartesian coordinate  $x_i$ . The energy  $e$  is defined by  $e = \rho(E + |u|^2/2)$ , where  $E$  is the internal energy per unit mass. The usual compressible formulation is used to nondimensionalise these equations, where the superscript  $d$  refers to the dimensional quantity, and the subscript  $\infty$  denotes the

freestream property.

$$\begin{aligned} \rho &= \frac{\rho^d}{\rho_\infty} & P &= \frac{P^d}{\rho_\infty a_\infty^2} & T &= \frac{T^d c_p}{a_\infty^2} & e &= \frac{e^d}{\rho_\infty a_\infty^2} \\ u_i &= \frac{u_i^d}{a_\infty} & x_i &= \frac{x_i^d}{D} & t &= \frac{t^d a_\infty}{D} \end{aligned}$$

Here,  $\gamma$  is the ratio of specific heats,  $c_p$  the specific heat at constant pressure,  $a$  the speed of sound, and  $D$  the cavity depth. The Prandtl number and the Reynolds numbers are defined respectively as

$$Pr = \frac{c_p \mu_\infty}{k} \quad Re = \frac{\rho_\infty a_\infty D}{\mu_\infty} \quad Re_\theta = \frac{\rho_\infty U_\infty \theta_0}{\mu_\infty},$$

where  $k$  is the thermal conductivity,  $\mu$  the dynamic viscosity and  $\theta_0$  the initial boundary layer momentum thickness at the cavity leading edge.

A linearized version of the equations is also implemented: we assume that the flow field  $\mathbf{q} = [\rho u, \rho v, \rho w, \rho, e]^T$  can be decomposed into  $\mathbf{q} = \bar{\mathbf{q}} + \mathbf{q}'$ , where  $\bar{\mathbf{q}}$  is a steady solution of the equations and the perturbation field  $\mathbf{q}'$  verifies  $\mathbf{q}' \ll \bar{\mathbf{q}}$ . The Navier–Stokes equations are then linearised about  $\bar{\mathbf{q}}$  by neglecting higher-order terms in  $\mathbf{q}'$  to give a first-order approximation. The perturbation field now satisfies

$$\begin{aligned} \frac{\partial \rho'}{\partial t} + \frac{\partial}{\partial x_j} (\bar{\rho} u'_j + \rho' \bar{u}_j) &= 0 \\ \frac{\partial}{\partial t} (\bar{\rho} u'_i + \rho' \bar{u}_i) + \frac{\partial}{\partial x_j} (\bar{\rho} (\bar{u}_i u'_j + u'_i \bar{u}_j) + \rho' \bar{u}_i \bar{u}_j + P' \delta_{ij}) &= \frac{1}{Re} \frac{\partial}{\partial x_j} \left( \frac{\partial u'_i}{\partial x_j} + \frac{\partial u'_j}{\partial x_i} - \frac{2}{3} \frac{\partial u'_k}{\partial x_k} \delta_{ij} \right) \\ \frac{\partial e'}{\partial t} + \frac{\partial}{\partial x_j} ((\bar{e} + \bar{P}) u'_j + (e' + P') \bar{u}_j) &= \frac{1}{Re} \frac{\partial}{\partial x_j} \left( \bar{u}_i \left( \frac{\partial u'_i}{\partial x_j} + \frac{\partial u'_j}{\partial x_i} - \frac{2}{3} \frac{\partial u'_k}{\partial x_k} \delta_{ij} \right) \right. \\ &\quad \left. + u'_i \left( \frac{\partial \bar{u}_i}{\partial x_j} + \frac{\partial \bar{u}_j}{\partial x_i} - \frac{2}{3} \frac{\partial \bar{u}_k}{\partial x_k} \delta_{ij} \right) \right) \\ &\quad + \frac{1}{Re} \frac{1}{Pr} \frac{\partial^2 T'}{\partial x_k \partial x_k} \end{aligned} \tag{2.2}$$

The existing DNS code can solve linear or nonlinear NS equations for both two-dimensional and three-dimensional flows. The equations are solved on a structured mesh, using a sixth-order compact finite-difference scheme for spatial discretization in the x- and y-direction (Lele, 1992), and a fourth-order Runge-Kutta algorithm for time-marching. The cavity is supposed homogeneous (periodic) in the spanwise direction (z-direction) and the derivatives are computed using Fast Fourier Transform (FFT) method with subroutines provided by the FFTW library (Frigo & Johnson, 1997-2007). The boundary conditions are non-reflective for the inflow and outflow, no slip, and constant temperature ( $T = T_\infty$ ) at the walls (Thompson, 1990; Poinsoot & Lele, 1992). In addition, a buffer zone is implemented at the inflow, outflow, and normal computational boundaries to reduce acoustic reflections (Colonus *et al.*, 1993; Freund, 1997). Unless stated otherwise, the simulations are initiated with a Blasius flat-plate boundary layer spanning the cavity and zero flow within the cavity.

The code can handle any type of block geometry and is fully parallelized using Message-Passing Interface (MPI). The simulations were performed on high-performance Beowulf clusters at the California Institute of Technology. Additional computer resources were provided by the Air Force Office of Scientific Research (AFOSR) and the Army Research Laboratory (ARL).

The cavity configuration and flow conditions are controlled by the following parameters: the cavity aspect ratio  $L/D$  and spanwise extent  $\Lambda/D$ , the ratio of the cavity length to the initial boundary layer momentum thickness at the leading edge of the cavity  $L/\theta_0$ , the Reynolds number  $Re_\theta = U\theta_0/\nu$ , and the freestream Mach number  $M = U/a_\infty$  (see figure 2.1). As temperature differences are expected to remain small, the transport properties are assumed constant: we set  $Pr = 0.7$  and  $\gamma = 1.4$ , the values for air.

Typical grid sizes ranged from a few hundred thousand to several million grid points. Each spanwise wavenumber is discretized on a stretched Cartesian grid, with clustering of points near the walls and the shear layer spanning the cavity. Numerical probes are set up to record all the flow field variables  $u$ ,  $v$ ,  $\rho$ ,  $P$  (and

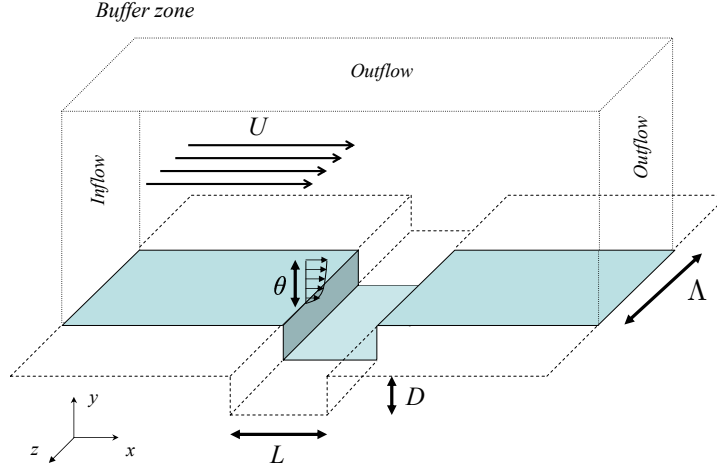


Figure 2.1: Basic configuration of the computational domain

$w$  in 3D) at every time step. For 2D simulations, three approximately equi-spaced probes are located in the shear layer at  $y = 0$ , and three more at the same stream-wise positions inside the cavity at  $y = -0.5D$ . Additional probes in the spanwise cross-section  $z = 0.5\Lambda$  and equally spaced along the span in the shear layer at  $(x, y) = (0.5L, 0)$  are considered for 3D simulations. Figure 2.2 shows a typical 3D grid and the location of the probes.

On a side note, we also report that the numerical code we developed has been successfully used to investigate other problems than cavity flows. Gudmundsson & Colonius (2006) adapted the code to study jet noise and the linear stability characteristics of the mean velocity profiles produced by chevron nozzles. Burnes & Colonius (2007) are implementing a Large Eddy Simulation version of the code to investigate the mixing and flame-holding characteristics of cavity flows at high Reynolds numbers. Future applications of the code also include simulations of ultrasonically absorptive coating for hypersonic laminar flow control.

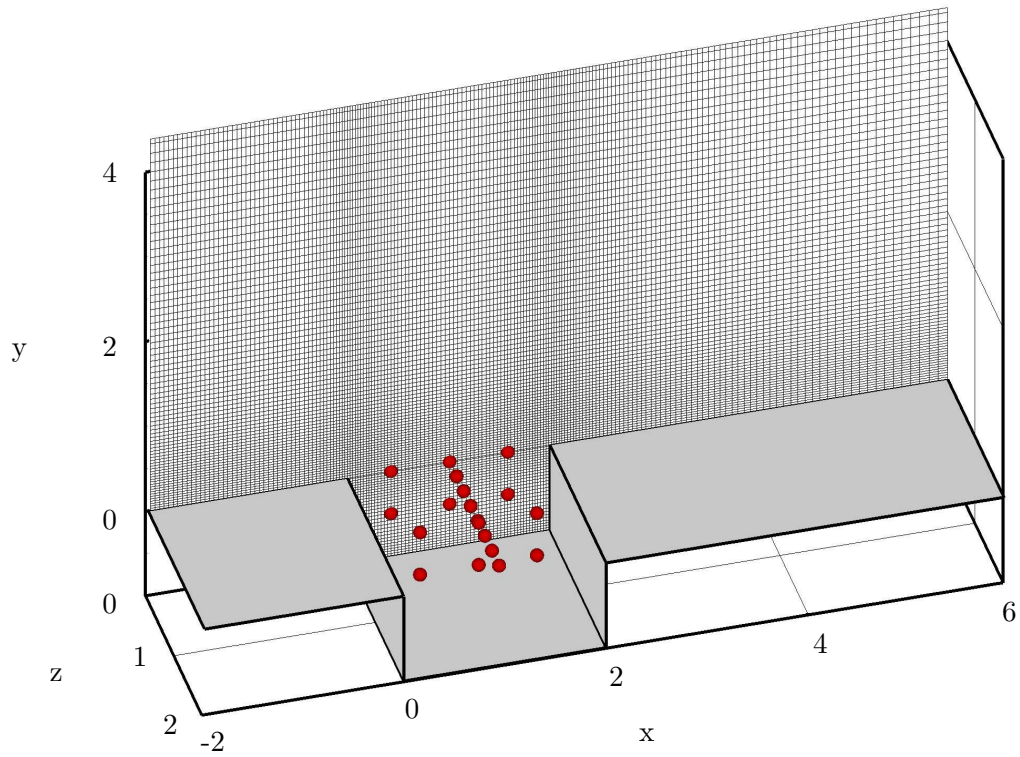


Figure 2.2: Visualisation of the computational grid. Only the mesh in the spanwise cross-section  $z = 0$  is represented (shown every other point). The red spheres indicate the location of the probes inside the cavity and in the shear layer.

## 2.2 Linear stability theory

Based on the assumption that the shear layer may be decoupled from the acoustic scattering and recirculating flow in the cavity, the classical approach to study the stability of cavity flow uses the theory of linear stability of parallel shear flow. The equations of motions are linearized about a parallel mean flow (known basic flow, only function of one spatial direction) and the fluctuations are written in normal mode form. In general, this formulation leads to an eigenvalue problem and a dispersive relation, which relates frequencies of the perturbations to their corresponding wavenumber. For the classical approach, non-parallel effects are only included through the introduction of a quasi-parallel (or Parabolized) stability approach that cannot account for the effects of the leading and trailing cavity edges (and their acoustic coupling to the hydrodynamic disturbances). Recent work by Alvarez *et al.* (2004; 2005) has extended the parallel flow stability analysis to include the scattering/receptivity/acoustic feedback by using a Weiner-Hopf technique, but non-parallel and three-dimensional effects have not been considered.

An alternative analysis, called bi-global linear stability theory, has been used for non-parallel flows (Theofilis & Colonius, 2003; Theofilis *et al.*, 2004; Theofilis, 2003). In this approach, the transient solution of the equations of motion  $\mathbf{q} = [\rho u, \rho v, \rho w, \rho, e]^T$  is decomposed into

$$\mathbf{q}(x, y, z, t) = \bar{\mathbf{q}}(x, y) + \mathbf{q}'(x, y, z, t), \quad (2.3)$$

where  $\bar{\mathbf{q}}(x, y)$  is the unknown steady two-dimensional basic flow and  $\mathbf{q}'(x, y, z, t)$  an unsteady three-dimensional perturbation with  $\|\mathbf{q}'\| \ll \|\bar{\mathbf{q}}\|$ . As the domain is homogeneous in the spanwise direction, a general perturbation can be decomposed into Fourier modes with spanwise wavenumbers  $\beta$ . At linear order, modes with different wavenumbers are decoupled and the following eigenmode Ansatz can be introduced:

$$\mathbf{q}'(x, y, z, t) = \sum_n \hat{\mathbf{q}}_n(x, y) \exp[i(\beta z - \Omega_n t)] + c.c., \quad (2.4)$$

where the parameter  $\beta$  is taken to be a real and prescribed spanwise wavenumber, related to a spanwise wavelength in the cavity by  $\lambda = 2\pi/\beta$ ,  $\hat{\mathbf{q}}_n$  and  $\Omega_n = \omega_n + i\sigma_n$  are the unknown complex eigenmodes and corresponding complex eigenvalues, both dependent on  $\beta$ . Complex conjugation is required in equation (2.4) since  $\mathbf{q}'$  is real. The frequency and the growth/damping rate of the mode are given by  $\omega_n$  and  $\sigma_n$ , respectively. The long-time behavior of the linear solution will be dictated by the mode with the eigenvalue  $\Omega = \omega + i\sigma$  of largest imaginary part. The flow is said to be subcritical (stable) if  $\sigma$  is strictly negative, neutrally stable if  $\sigma = 0$ , and supercritical (unstable) if  $\sigma > 0$ .

Eventually, the determination of the least damped (or most unstable) modes for a given wavelength  $\beta$  amounts to finding the eigenvalue  $\Omega$  and corresponding eigenvector by integrating the governing equations directly in the time domain.

### 2.3 Residual method and L2 fitting routines

To determine the least-damped eigenvalue practically, a least-squares fitting method (Press *et al.*, 1992) is applied to the data time history when exponential decay or growth was reached: given the long-time evolution of the vector field  $q'$  at any location  $(x_0, y_0, z_0)$  and an initial guess for the unknown parameters  $\bar{\mathbf{q}}(x_0, y_0, z_0)$ ,  $\hat{\mathbf{q}}_r(x_0, y_0, z_0)$ ,  $\hat{\mathbf{q}}_i(x_0, y_0, z_0)$ ,  $\omega$ , and  $\sigma$ , a set of “best-fit” parameters is computed such that the “merit function”  $\chi$ , which measures the agreement between the data and the model (with a particular choice of parameters), is minimized. In our case, the model depends nonlinearly on a set  $(a_k, k = 1, 2, \dots, M)$  of unknown parameters and the “merit function”  $\chi$  is defined as

$$\chi^2 = \sum_{i=1}^{N_{fit}} \left[ \frac{data_i - X(a_1, a_2, \dots, a_M, t_i)}{\sigma_i} \right]^2,$$

where  $(data_i, t_i)$  is the set of  $N_{fit}$  data point to fit,  $X$  is a fixed function of  $t$  and the parameters  $a_k$ , and  $\sigma_i$  is the measurement error (standard deviation) on the  $i$ -th data point. Since the measurement errors are not known,  $\sigma_i$  is set to 1.

Following equation (2.4), the “merit function” takes the form

$$\chi^2 = \sum_{i=1}^N \left[ \mathbf{q}'(x_0, y_0, z_0, t_i) - (a_1 + (a_4 \cos a_2 t_i - a_5 \sin a_2 t_i) e^{a_3 t_i}) \right]^2.$$

Note that the method is sensitive to the initial guess (same order of magnitude as the “best-fit” parameters needed for accurate results) and the length of data to fit (namely, if  $N$  is too large and the data still contains transient components, the fit may not be successful). Upon convergence, the mode frequency  $\omega = a_2$  and growth/damping rate  $\sigma = a_3$ , which are independent of the location  $(x_0, y_0, z_0)$ , can be recovered.

With the eigenvalue determined, equation (2.4) may be written at three different times,  $t_1$ ,  $t_2 = t_1 + \Delta t$ , and  $t_3 = t_1 + 2\Delta t$  as a linear system of three unknowns  $\bar{\mathbf{q}}$ ,  $\hat{\mathbf{q}}_r$ , and  $\hat{\mathbf{q}}_i$ . With the transient solution  $\mathbf{q}_n = \mathbf{q}(x, y, z, t_n)$  available at these times, the system can be solved to deliver the steady-state solution  $\bar{\mathbf{q}}$  and the spatial structure  $(\hat{\mathbf{q}}_r, \hat{\mathbf{q}}_i)$  of the linear eigenmode:

$$\bar{\mathbf{q}} = \frac{\mathbf{q}_1 e^{2\sigma\Delta t} - 2\mathbf{q}_2 e^{\sigma\Delta t} \cos \omega\Delta t + \mathbf{q}_3}{e^{2\sigma\Delta t} - 2e^{\sigma\Delta t} \cos \omega\Delta t + 1} \quad (2.5)$$

$$\hat{\mathbf{q}}_r = \frac{s_1(\mathbf{q}_2 - \bar{\mathbf{q}}) - s_2(\mathbf{q}_1 - \bar{\mathbf{q}})}{c_2 s_1 - c_1 s_2} \quad (2.6)$$

$$\hat{\mathbf{q}}_i = \frac{c_1(\mathbf{q}_2 - \bar{\mathbf{q}}) - c_2(\mathbf{q}_1 - \bar{\mathbf{q}})}{c_2 s_1 - c_1 s_2} \quad (2.7)$$

where

$$c_1 = e^{\sigma t_1} \cos \omega t_1 \quad c_2 = e^{\sigma t_2} \cos \omega t_2 \quad s_1 = e^{\sigma t_1} \sin \omega t_1 \quad s_2 = e^{\sigma t_2} \sin \omega t_2.$$

## 2.4 ARPACK

To validate the linear stability results, a direct approach was also considered, where the eigenmodes are directly searched for using an Arnoldi method developed in the ARPACK software (Lehoucq *et al.*, 1996–2007), rather than isolated

through long-time integration. Following the nomenclature introduced in §2.2, for a given wavenumber  $\beta$ , the three-dimensional linearized NS equations can be written symbolically in matrix notation as

$$\frac{\partial \mathbf{q}'}{\partial t} = \mathcal{A} \left( \frac{\partial}{\partial x}, \frac{\partial}{\partial y}, \bar{\mathbf{q}} \right) \mathbf{q}', \quad (2.8)$$

where  $\mathbf{q}'$  is the vector of the perturbed conservative variables and  $\mathcal{A}$  is a spatial differential operator depending on the base flow and cavity parameters (aspect ratio, spanwise wavenumber,  $Re$ , etc.). Once the equations are spatially discretized, we may represent this equation as:

$$\frac{\partial \mathbf{q}'}{\partial t} = A \mathbf{q}', \quad (2.9)$$

where now  $\mathbf{q}'$  is the discretized solution vector (length  $5N$  where  $N$  is the number of grid points), and  $A$  is a constant real  $5N$  by  $5N$  matrix. In this discrete approach, the matrix  $A$  is a function of the (discretized) known steady flow  $\bar{\mathbf{q}}$  and the simulation parameters. The stability of this ordinary differential equation depends on the eigensystem of  $A$ . The eigenvalues ( $\lambda_n, n = 1, N$ ) are  $N$  not necessarily distinct solutions of  $\det(A - \lambda I) = 0$ , and the corresponding eigenvectors  $x_n$  are the linearly independent solutions of  $Ax_n = \lambda_n x_n$ . For the non-defective cases where there are  $N$  linearly independent eigenvectors,  $X^{-1} = [x_1, x_2, \dots, x_N]^{-1}$  exists and the solution can be written symbolically as

$$\mathbf{q}' = e^{At} \mathbf{q}'_0, \quad (2.10)$$

where  $\mathbf{q}'_0$  is the initial perturbation and

$$e^{At} = X \text{diag}[e^{\lambda_1 t}, e^{\lambda_2 t}, \dots, e^{\lambda_N t}] X^{-1}. \quad (2.11)$$

Therefore, for any initial condition, the long-time decay or growth of the solution will be dictated by the eigenvalue  $\lambda_m$  with the largest real part, and the same

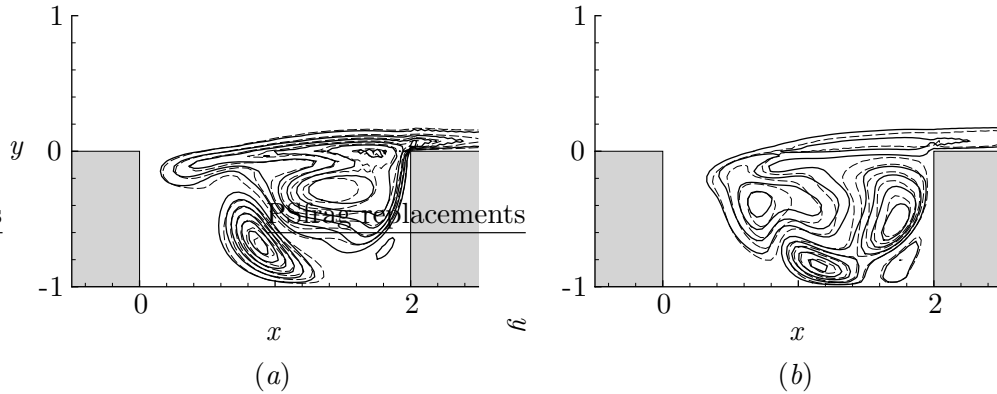


Figure 2.3: Contours of the streamwise velocity  $u'/U$  for the dominant eigenmode of spanwise wavelength  $\lambda/D = 1$  for run 2M0325: ( - - - - ) ARPACK solution; ( — ) Linear stability result; (a) real part; (b) imaginary part

conclusion stands if the system is defective. Comparison of equations (2.4) and (2.11) reveals that the continuous and discrete formalisms are simply related by  $\lambda_m = -i\Omega$ . Given a cavity configuration and flow conditions, the eigenvalue of  $A$  with largest real part (i.e., the least damped or fastest growing three-dimensional mode) could theoretically be directly computed using ARPACK, as well as the corresponding eigenvector, to visualise the shape of the instability.

In practice, the use of ARPACK was significantly limited by the size and complexity of our problem. The software was therefore only used here to validate our time-domain methods. As expected, the dominant eigenmode and corresponding eigenvalue computed with ARPACK for the same test case were in excellent agreement with the results of the linear stability analysis, as shown in figure 2.3. Both methods predicted three-dimensional instabilities with less than 1% difference on the mode growth rate and frequency.

## 2.5 Validation

Throughout this study, several test cases were set to validate the method and its implementation. The DNS code was successfully tested through comparison with

simple acoustic problems and previous validated numerical results from Rowley *et al.* (2002*b*). The two-dimensional basic flow calculations are performed on fine grids (about half a million to a million grid points) and for supercritical cases, the oscillation frequencies are in good agreement with Rossiter mode frequencies, as further discussed in § 3.1.2).

Additionally, the 2D simulation 2M06-K reproduces one of the experimental configurations of Krishnamurty (1956) with laminar incoming boundary layer. The flow parameters ( $L/D = 2$ ,  $M = 0.6$ ,  $L/\theta_0 = 80$ ,  $Re_D = 1500$ ) match the conditions of the experiment (apart from the Reynolds, which is higher by about a factor 20 in the experiment). We find good qualitative agreement between the structure of the radiated acoustic field and schlieren pictures from the experiment. The measured frequency is  $f \approx 29\,000$  Hz, which corresponds to a Strouhal number  $St_L = fL/U \approx 0.73$ . This result matches the oscillation frequency  $St_L = 0.723$  in our numerical simulation (see appendix A). Using optical interferometry, Krishnamurty (1956) estimated the sound pressure levels (SPL) to approximately 163 dB for different cavity configurations. This value is similar to the SPL we measure and report in chapter 5.

For the stability analysis, it is particularly important to verify that the modes observed are physical and not generated by any numerical artifact. Several initial conditions with disturbances at different locations in the cavity were considered in order to perturb the linear equations and study the flow response. Similarly, to demonstrate grid convergence of the three-dimensional stability computations, simulations were performed on a finer grid for the same test case. As expected for a global instability, the dominant three-dimensional mode is independent of the initial perturbation and grid spacing, as both the nondimensionalised frequency  $St_D = \omega D/(2\pi U)$  and growth rate  $\sigma D/U$  are identical in all cases.

## Chapter 3

### Linear Stability Results

As described in chapter 2, the three-dimensional linear stability analysis relies on the existence of subcritical conditions with a steady two-dimensional basic flow  $\bar{\mathbf{q}}(x, y)$ , an exact solution of the 2D NS equations. However, for most experiments and realistic flight conditions, the flow parameters would be such that Rossiter modes do occur and eventually saturate into a periodically oscillating flow. It must be acknowledged that the presence of three-dimensional instabilities is likely to alter the two-dimensional basic flow on which the present linear analysis is based. With this in mind, our approach here is to investigate the three-dimensional linear stability of a given base flow, regardless of potential interactions. Such approach has been widely used to predict the stability and growth rate of boundary layers, for instance. As discussed in chapter 5 and chapter 6, the features observed in the linear results are in fact relevant to full nonlinear simulations and experiments. Potential extension of the linear stability analysis to supercritical conditions is presented in appendix C.

#### 3.1 Two-dimensional simulations

The first step of the linear stability analysis is to characterize the onset of two-dimensional cavity instability. We review here the general properties of the shear-layer (Rossiter) oscillations in compressible flows over open cavities.

### 3.1.1 Shear-layer mode

As discussed in the introduction, the shear-layer (Rossiter) mode is characterized by a flow-acoustic feedback process. Small disturbances in the shear layer are amplified as they advect downstream through the shear layer and generate acoustic waves upon impingement on the downstream edge of the cavity. These acoustic waves propagate back upstream and interact with the shear layer to excite further instabilities.

This mechanism is clearly observed in the 2D simulations. The vorticity, velocity and acoustic fields for run 2M06 ( $L/D = 2$ ,  $L/\theta_0 = 52.8$ ,  $M = 0.6$ ,  $Re_D = 1500$ ) are shown in figures 3.1, 3.2, and 3.3 respectively. They are representative of all the simulations with shear-layer mode oscillations. As mentioned in the validation section in § 2.5, good qualitative agreement is obtained between the density fluctuations observed in the simulations and schlieren pictures from experiments (e.g., Krishnamurty, 1956). In the present case, the roll-up of vorticity in the shear layer can be observed, but there is no shedding of vortical disturbances before impingement at the downstream cavity edge. In general, the velocity magnitude inside the cavity is only a fraction of the freestream velocity (less than 10% for subcritical conditions and up to 30% for supercritical conditions) and the internal flow is relatively weak.

One important feature of the cavity flow is the recirculating vortical flow (also commonly referred as primary vortex) in the downstream half of the cavity. This vortex is present in the steady state for subcritical conditions and in a time-averaged sense for supercritical conditions. Figure 3.4 shows the 2D steady base flow for different cavity configurations. As further discussed in § 3.2, the recirculating region plays a key role in the development of the three-dimensional instabilities.

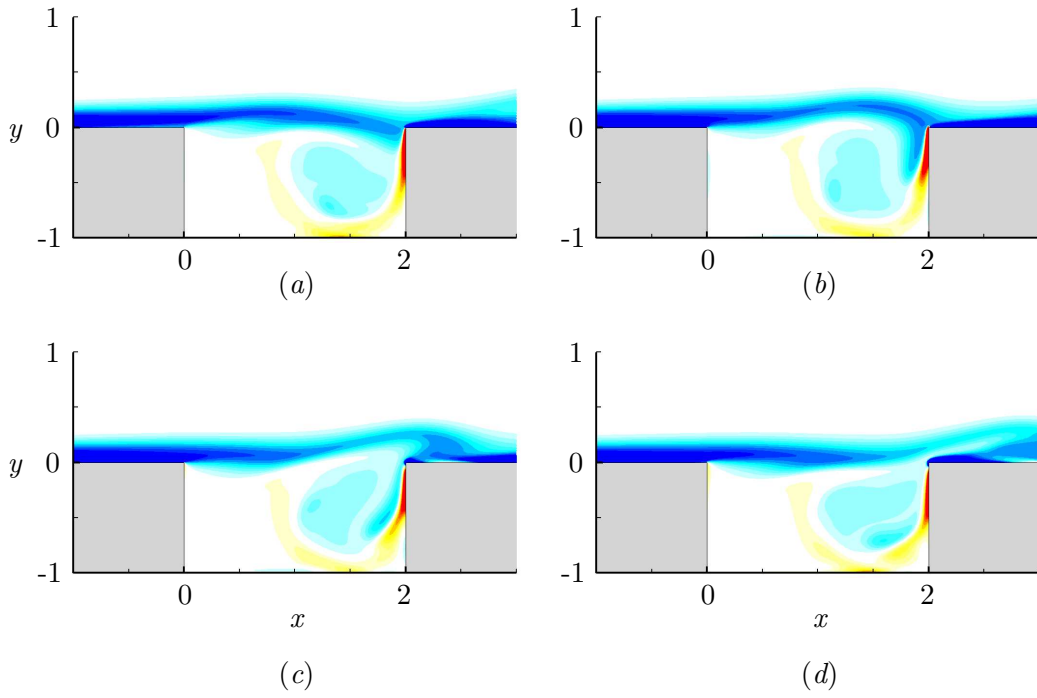


Figure 3.1: Vorticity field for the shear-layer mode (run 2M06) at four different times (*a-d*) corresponding to approximately a quarter of a period of oscillation; 21 equi-spaced contours of the vorticity are shown between  $\omega_z D/U = -5$  and 5.

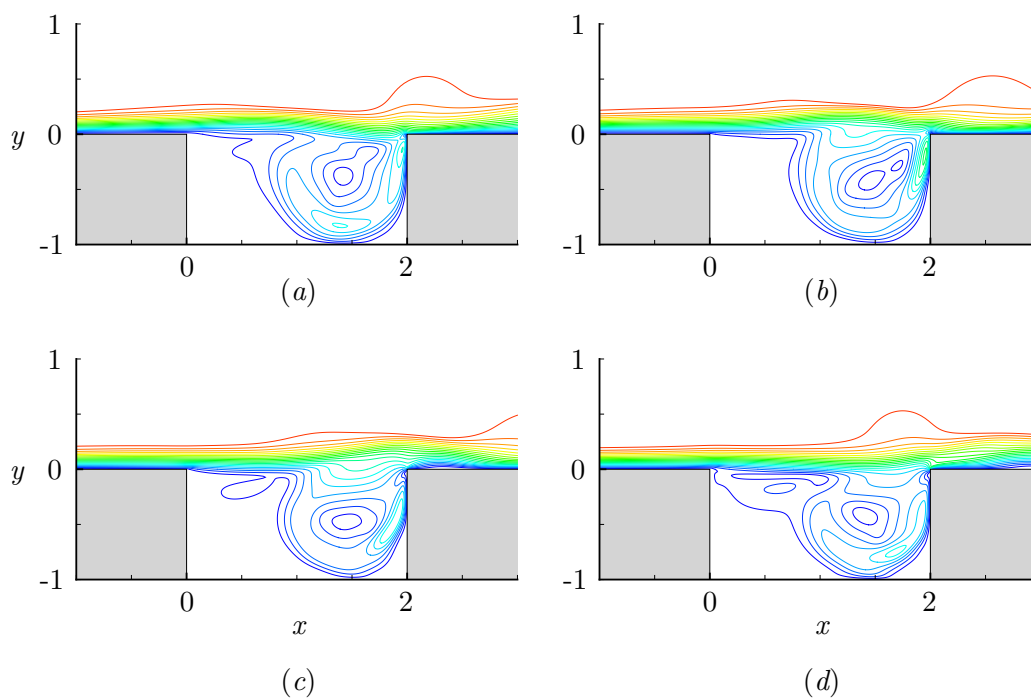


Figure 3.2: Velocity field for the shear-layer mode (run 2M06) at four different times (*a-d*) (same times as in figure 3.1); 19 equi-spaced contours of the velocity magnitude are shown between  $\|\mathbf{u}\|/U = 0.05$  and  $0.95$ .

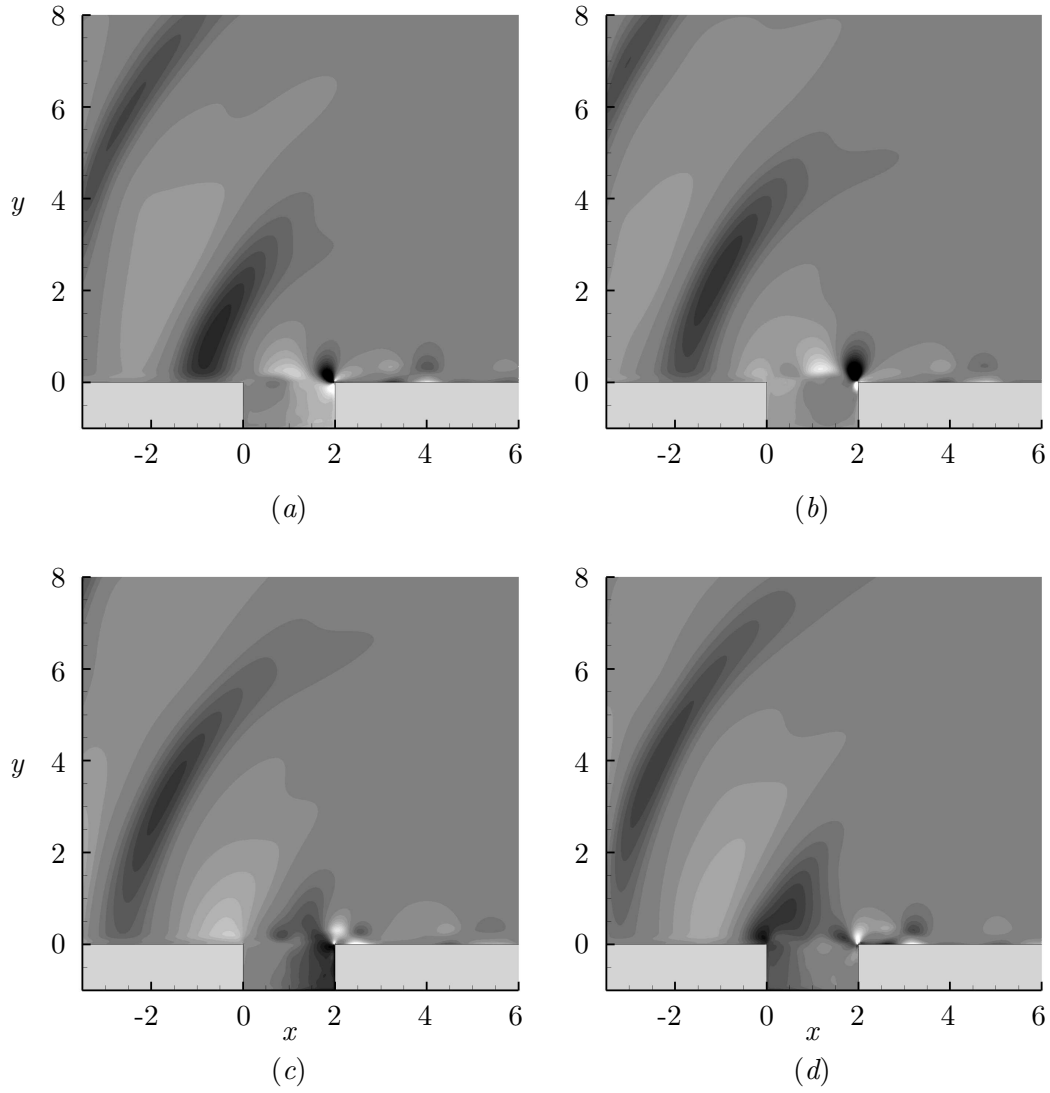


Figure 3.3: Visualisation of the acoustic field for the shear-layer mode (run 2M06) at four different times (*a-d*) (same times as in figure 3.1); 21 equi-spaced contours of the dilatation are shown between  $\nabla u D/U = -0.05$  and  $0.05$ .

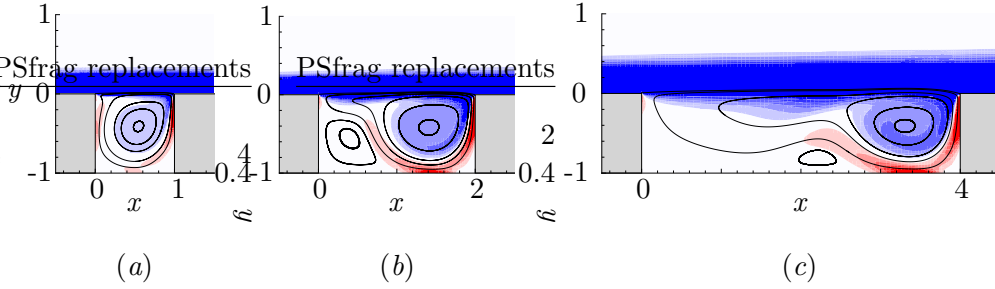


Figure 3.4: Vorticity contours and streamlines of the two-dimensional steady base flow; Ten equally-spaced contours between  $\omega_z D/U = -1$  and 1 are shown: (a) run H1Re200; (b) run 2M03; (c) run TK4M03Re65. In each case, the shear-layer and the primary vortex within the cavity are clearly identified.

### 3.1.2 Neutral stability curves

While Rossiter’s formula in equation 1.1 provides reasonable predictions for the frequency of oscillations that occur in self-sustained oscillations, it says nothing about *whether* such oscillations do occur and, if they do, which of many possible unstable modes is selected, and at what amplitude such oscillations would saturate. For the most part, it can be presumed that at realistic flight-values the parameters  $M$ ,  $Re_\theta$ ,  $L/D$ , and  $L/\theta$  would be such that oscillations do indeed occur. The critical values of, for example, the Reynolds at which the flow first becomes unstable is quite low. Nevertheless, it turns out that understanding the behaviour of the instability near this critical transition has important consequences for cavity oscillations at realistic Reynolds numbers.

The parameters for the different runs and the stability results are tabulated in appendix A. Given a cavity configuration and different flow conditions, several two-dimensional simulations are performed to construct the estimated neutral stability curve for the two-dimensional instabilities of the basic cavity flow (e.g., figures 3.5, 3.6, 3.7, and 3.8(a)). The DNS results are classified according to whether the flow is two-dimensionally stable (and thus a steady-state solution can be obtained) or whether the flow results in self-sustaining oscillations. The oscillation frequencies are computed for all the runs in shear-layer mode and are shown in these figures.

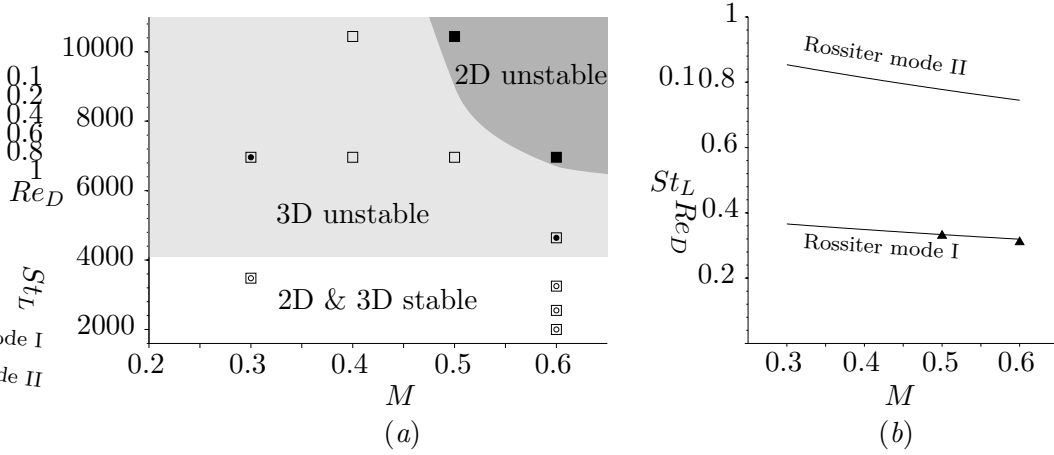


Figure 3.5: Results for cavity run series H1 ( $L/D = 1$ ,  $L/\theta_0 = 23.2$ ): (a) Schematic of the neutral stability curve from 2D nonlinear simulations (2D stable (□) and unstable (■)) and from the 3D linear analysis in § 3.2 (3D stable (○) and unstable (●)); (b) Strouhal numbers  $St_L = fL/U$  for the supercritical conditions in (a), compared to equation 1.1. Only one dominant mode (▲) is present in this case.

The results of the three-dimensional linear stability analysis from § 3.2 are also presented in figures 3.5, 3.6, 3.7, and 3.8(a). The different shaded regions indicate the approximate stability transitions. The critical conditions are estimated by linear interpolation between stable and unstable conditions. Here, it must be acknowledged that these figures represent a general stability trend rather than precise computation of critical conditions. Also, the 3D stability is based on linear results and is therefore not available for supercritical conditions (i.e., the region of 2D instability). However, the results of our nonlinear simulations, discussed in chapter 5, tend to indicate that the critical conditions for the onset of the 3D instability are similar on both sides of the 2D stability transition.

The two-dimensional results are consistent with the typical flow/acoustic resonant modes that have been observed in many cavity experiments (e.g., Krishnamurty, 1956; Rossiter, 1964; Sarohia, 1975; Heller & Bliss, 1975; Tam & Block, 1978; Ahuja & Mendoza, 1995) and numerical simulations (e.g., Fuglsang & Cain, 1992; Rowley *et al.*, 2002b; Gloerfelt *et al.*, 2003). In all the cases, the two-

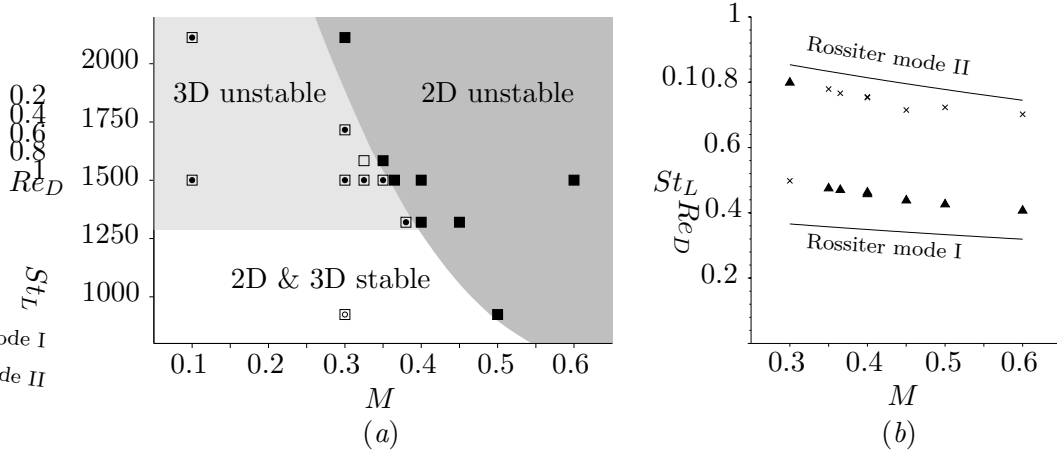


Figure 3.6: Results for cavity run series 2M ( $L/D = 2$ ,  $L/\theta_0 = 52.8$ ): (a) Schematic of the neutral stability curve from 2D nonlinear simulations (2D stable (  $\square$  ) and unstable (  $\blacksquare$  )) and from the 3D linear analysis in § 3.2 (3D stable (  $\circ$  ) and unstable (  $\bullet$  )); (b) Strouhal numbers  $St_L = fL/U$  for the supercritical conditions in (a), compared to equation 1.1: (  $\blacktriangle$  ) dominant mode, (  $\times$  ) subdominant mode

dimensional instability is essentially of the Rossiter type, wherein Kelvin-Helmholtz instabilities in the shear layer spanning the cavity are coupled to acoustic feedback and receptivity at the trailing and leading edges, respectively. Frequencies of oscillation are found to be predicted by Rossiter’s formula to within the experimental scatter of measurements that have been made over the years for cavities with laminar and turbulent boundary layers.

The onset of Rossiter mode as a function of the parameters is typically summarized qualitatively as follows: there is a critical value of  $M$ ,  $Re_\theta$ , and  $L/\theta$  beyond which oscillations occur. There does *not* appear to be any critical value of  $L/D$  in the range of parameters considered  $1 < L/D < 6$ . The stability results from the two-dimensional simulations are consistent with these general trends. For low Reynolds number and Mach number, the flow is subcritical and ultimately reaches a steady state. As these parameters, or the ratio of the cavity length to the initial boundary layer momentum thickness  $L/\theta_0$ , are increased, the flow becomes supercritical and oscillates in shear-layer (Rossiter) mode.

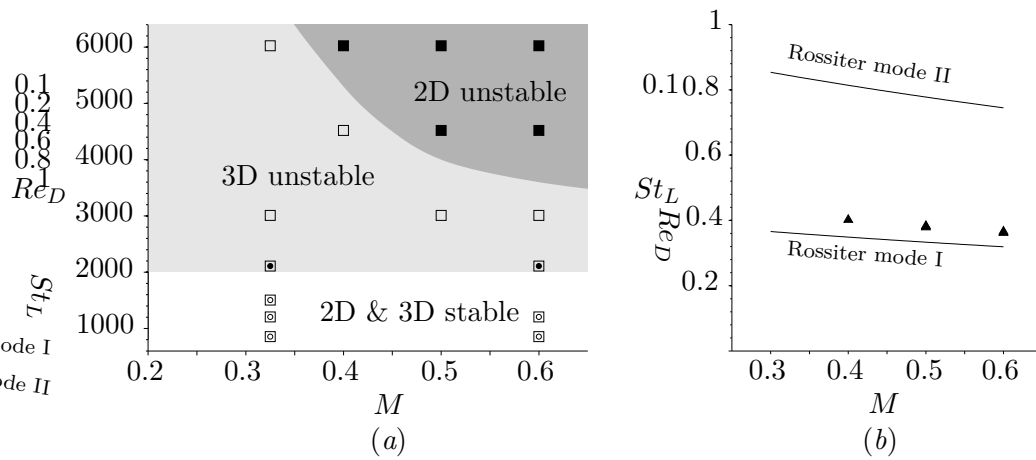


Figure 3.7: Results for cavity run series TK2 ( $L/D = 2$ ,  $L/\theta_0 = 30.12$ ): (a) Schematic of the neutral stability curve from 2D nonlinear simulations (2D stable (□) and unstable (■)) and from the 3D linear analysis in § 3.2 (3D stable (○) and unstable (●)); (b) Strouhal numbers  $St_L = fL/U$  for the supercritical conditions in (a), compared to equation 1.1. Only one dominant mode (▲) is present in this case.

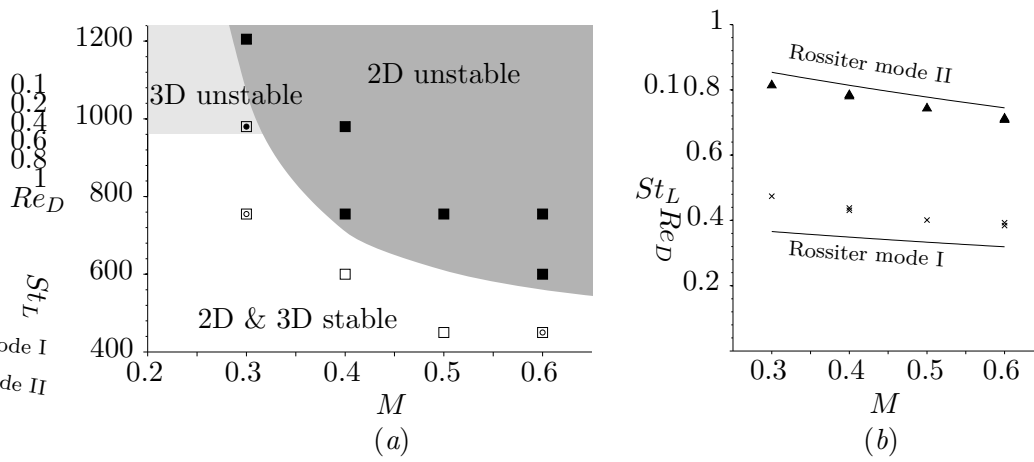


Figure 3.8: Results for cavity run series TK4 ( $L/D = 4$ ,  $L/\theta_0 = 60.24$ ): (a) Schematic of the neutral stability curve from 2D nonlinear simulations (2D stable ( $\square$ ) and unstable ( $\blacksquare$ )) and from the 3D linear analysis in § 3.2 (3D stable ( $\circ$ ) and unstable ( $\bullet$ )); (b) Strouhal numbers  $St_L = fL/U$  for the supercritical conditions in (a), compared to equation 1.1: ( $\blacktriangle$ ) dominant mode, ( $\times$ ) subdominant mode

As mentioned in the previous section, the parameters  $L/D$ ,  $L/\theta_0$ , and  $Re_\theta$  affect the oscillation frequencies, and in particular the selection of a particular resonant frequency. For instance, in figure 3.6, the flow is stationary for run 2M03 at  $M = 0.3$  and  $Re_D = 1500$ . The regime of shear-layer oscillations can be reached by either increasing the Reynolds number (i.e., run 2M03Re80) or the Mach number (i.e., run 2M04). Here, the resonant frequency corresponds to a Rossiter mode II in the first case and mode I in the latter. In general, higher Rossiter modes are observed for larger  $L/\theta_0$  and higher Mach number (see appendix A).

## 3.2 Three-dimensional linear stability

The neutral stability curves presented in the previous section (3.1) are the starting point of the *three-dimensional* linear stability analysis: the goal here is to investigate whether or not 3D instability takes place before the onset of 2D instabilities.

For subcritical cases, the two-dimensional steady flow  $\bar{q}$  is extracted from the DNS and used as base flow for the linear three-dimensional simulations: as initial condition, a perturbation of given wavelength  $\lambda$  (therefore looking at one  $\beta$ -mode at a time) is added to  $\bar{q}$  and the 3D linearised Navier–Stokes equations are solved. The least damped (or most unstable) eigenmode (e.g., figure 3.14) and the corresponding eigenvalue  $\Omega = \omega + i\sigma$  are then determined from the long-time response of the cavity (e.g., figure 3.9). The nondimensionalised growth/damping rate  $\sigma D/U$  and Strouhal number  $St_D = \omega D/2\pi U$  are computed in each case for a set a discrete spanwise wavelength (e.g., figure 3.10) and the stability of the three-dimensional mode is reported back on the stability curve.

### 3.2.1 Three-dimensional mode properties

Figures 3.10, 3.11, and 3.12 show the growth/damping rate and frequency of the dominant three-dimensional mode as a function of the spanwise wavelength, for different cavity configurations and flow conditions. The plots in these three figures have much the same character and are representative of the results for cavities of

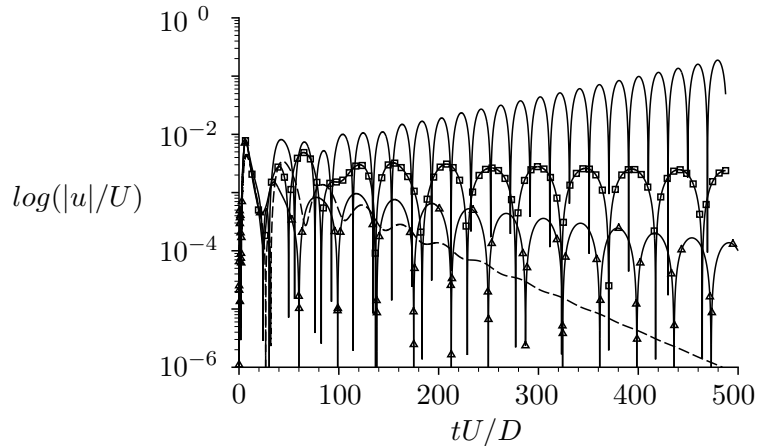


Figure 3.9: Long-time linear response of the cavity to three-dimensional perturbations of different spanwise wavelengths for run 2M0325 at  $(x, y, z) = (L/2, 0, 0)$ : ( ---- )  $\lambda/D = 0.5$ , ( ——— )  $\lambda/D = 1$ , (  $\square$  )  $\lambda/D = 1.5$ , (  $\triangle$  )  $\lambda/D = 2$ . This figure is a typical output of the linear stability simulations. Here, the disturbance of spanwise wavelength  $\lambda/D = 1$  is growing exponentially while the disturbances at other wavelengths are damped.

aspect ratio  $L/D = 1$ ,  $L/D = 2$ , and  $L/D = 4$  considered here (see appendix A)

For a band of spanwise wavelengths around the size of the cavity depth ( $\lambda/D \approx 1$ ), the dominant mode has a positive growth rate under certain conditions. This unstable mode (referred as Mode *ii*) is unsteady and the oscillation frequency based on the cavity depth  $D$  are comparable in all cases. This suggests that  $D$ , rather than  $L$  or  $\theta_0$ , is the most appropriate length scale to characterize the three-dimensional instability. By contrast, the two-dimensional unstable Rossiter mode has frequency  $fL/U$  scaling with the cavity length: in this feedback process, the resonant frequencies are directly connected to the times for vortical structures and radiated sound to travel downstream and upstream across the cavity of length  $L$ . For the three-dimensional instabilities, the frequency is found to be strongly associated with the two-dimensional base flow and its recirculating vortical flow within the cavity, which is about dimension  $D$  in all cases. Details about the recirculating flow and the mode frequency are further discussed in § 3.2.3.

Aside from this oscillatory mode, the presence of other three-dimensional modes is suggested in figures 3.10, 3.11, and 3.12. In particular, the linear stability of the shortest cavity  $L/D = 1$  differs from the other cases. As the Reynolds number is increased, the first mode to become unstable is steady ( $St_D = 0$ ) and has a smaller spanwise wavelength ( $\lambda/D \approx 0.5$ ). A similar steady mode (referred as Mode *i*) is observed for cavities of larger aspect ratio but is not amplified. We argue that the specific properties of the three-dimensional mode for the square cavity are related to the recirculating vortical flow that occupies the whole cavity in that particular configuration. These features are discussed in more detail in chapter 4.

Finally, the linear stability results also suggest the presence of another unsteady mode of larger spanwise wavelength  $\lambda/D \geq 1.5$ . However, this mode *iii* does not have the largest linear growth rate at any of the conditions considered here, and is not observed in the three-dimensional nonlinear simulations we performed. For several cases, a more extensive set of spanwise wavelength was also considered ( $0.1 \leq \lambda/D \leq 32$ ), but did not lead to any additional instabilities.

### 3.2.2 Parameter dependence

As mentioned previously, the parameters  $L/D$ ,  $L/\theta_0$ ,  $Re_D$ , and  $M$  control the onset of the shear-layer (Rossiter) oscillation and whether the steady two-dimensional flow needed for the linear analysis exists or not. Within the domain of 2D stability, our linear results show that the flow parameters affect the properties of the three-dimensional modes in four aspects. First, as discussed above, the cavity aspect ratio controls which mode (namely *i* or *ii*) is the dominant mode; secondly, the Reynolds number has a *direct* effect on the growth rate as viscosity plays a stabilizing role; thirdly, a change in certain parameters (e.g.,  $L/\theta_0$  and  $Re$ ) modifies the strength of the recirculating region in the two-dimensional base flow and *indirectly* the mode growth rate and frequency; and finally, the Mach number has little influence on the mode properties.

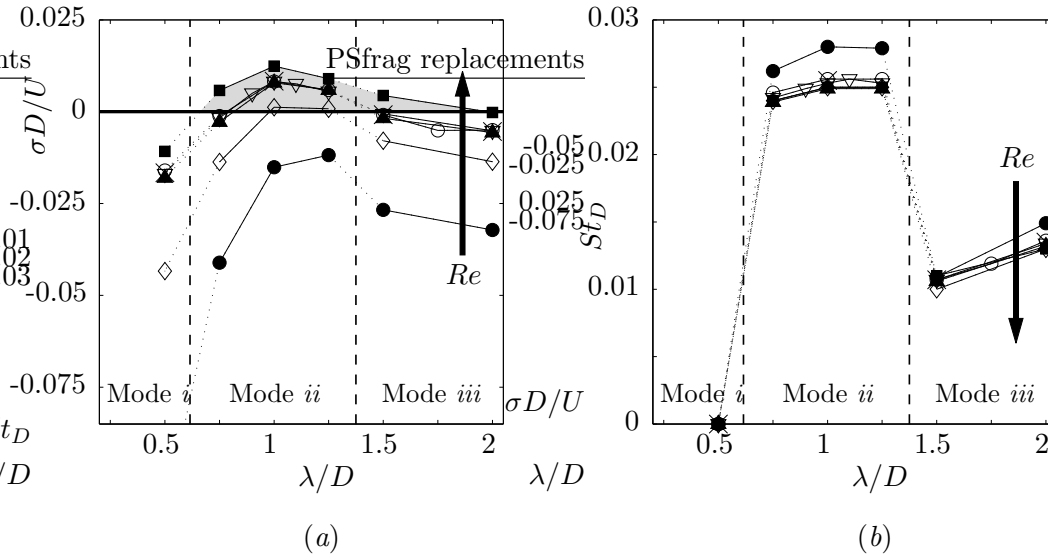


Figure 3.10: 3D linear stability results for run series 2M ( $L/D = 2, L/\theta_0 = 52.8$ ) as a function of the spanwise wavelength  $\lambda/D$ , for increasing Reynolds number (as indicated by the arrow) and different Mach numbers:  $0.1 < M < 0.38$  for runs 2M01 ( $\times$ ), 2M0325 ( $\nabla$ ), 2M035 ( $\circ$ ) and 2M038Re50 ( $\diamond$ );  $M = 0.3$  for runs 2M03Re35 ( $\bullet$ ), 2M03 ( $\blacktriangle$ ) and 2M03Re65 ( $\blacksquare$ ). The thick solid line represents the stability transition  $\sigma_D = 0$  and the region of positive growth rate is shaded; different modes of instability are suggested. (a) Growth/damping rate, (b) Frequency

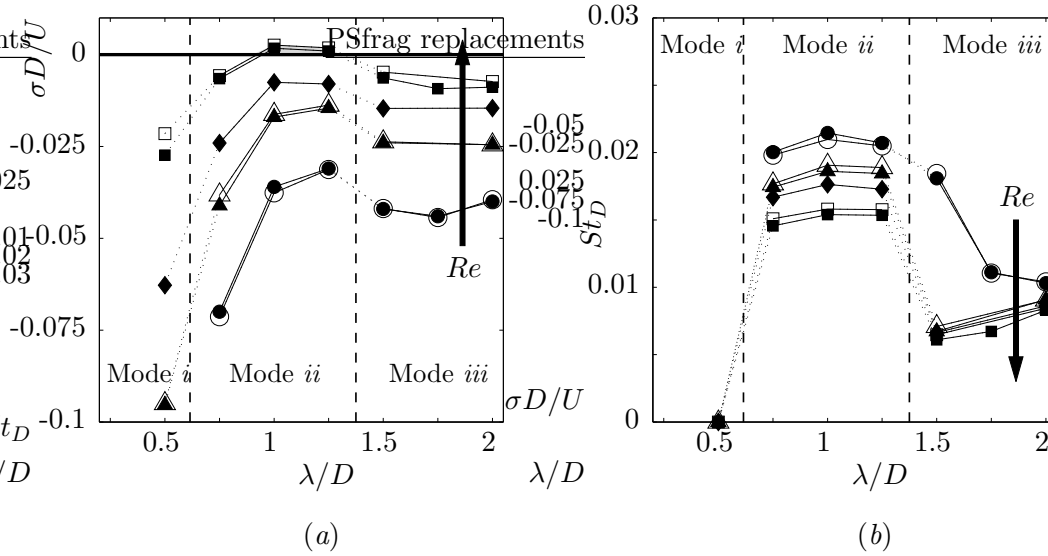


Figure 3.11: 3D linear stability results for run series TK2M ( $L/D = 2, L/\theta_0 = 30.12$ ) as a function of the spanwise wavelength  $\lambda/D$ , for increasing Reynolds number (as indicated by the arrow). Two sets of Mach numbers are considered:  $M = 0.6$  for runs TK2M06 ( $\circ$ ), TK2M6Re80 ( $\triangle$ ) and TK2M06Re140 ( $\square$ );  $M = 0.325$  for runs 2M0325 ( $\bullet$ ), 2M0325Re80 ( $\blacktriangle$ ), 2M0325Re100 ( $\blacklozenge$ ) and 2M0325Re140 ( $\blacksquare$ ). The thick solid line represents the stability transition  $\sigma_D = 0$  and the region of positive growth rate is shaded; different modes of instability are suggested. (a) Growth/damping rate, (b) Frequency

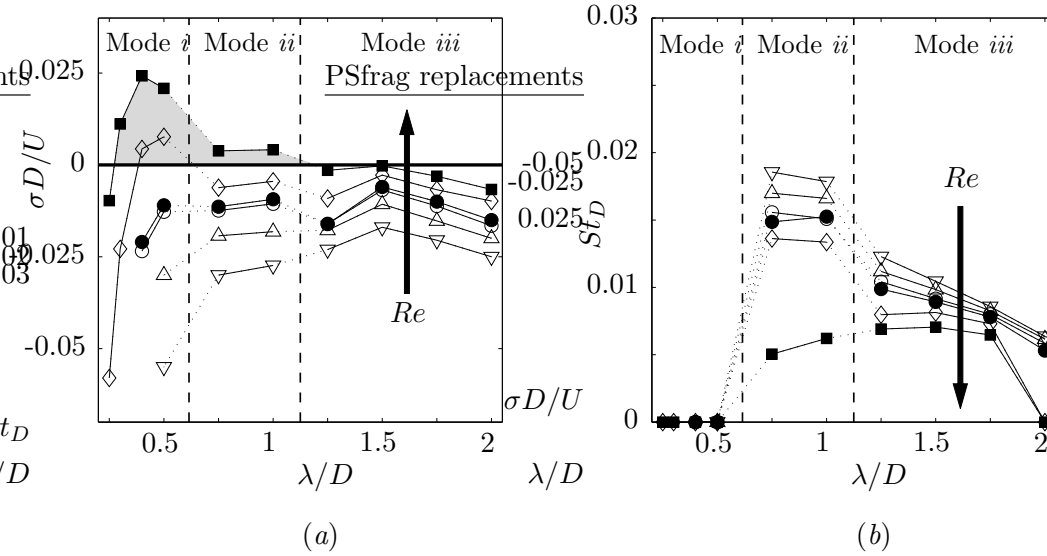


Figure 3.12: 3D linear stability results for run series H1 ( $L/D = 1, L/\theta_0 = 23.2$ ) as a function of the spanwise wavelength  $\lambda/D$ , for increasing Reynolds number (as indicated by the arrow). Two sets of Mach numbers are considered:  $M = 0.6$  for runs H1 ( $\nabla$ ), H1Re110 ( $\triangle$ ), H1Re140 ( $\circ$ ) and H1Re200 ( $\diamond$ );  $M = 0.3$  for runs H1M03Re150 ( $\bullet$ ) and H1M03Re300 ( $\blacksquare$ ). The thick solid line represents the stability transition  $\sigma_D = 0$  and the region of positive growth rate is shaded; different modes of instability are suggested. (a) Growth/damping rate, (b) Frequency

### Reynolds number

As indicated by the arrows in figures 3.10, 3.11, and 3.12, an increase in Reynolds number has two effects on the properties of the instability: it significantly increases the growth rate and moderately decreases the oscillation frequency (see details in § 3.2.3). To fully ascertain the effect of  $Re$  on the onset of three-dimensional mode, we performed a set of numerical experiments in which the base flow was artificially held constant as  $Re$  was increased (for details, see appendix B). The results confirmed that the growth rate of the dominant mode is directly driven by the Reynolds number. Viscosity damps the instability and there is a critical Reynolds number, above which the flow becomes three-dimensionally unstable. Since the Reynolds numbers considered in this study are low, the three-dimensional unstable modes are likely to exist for high Reynolds number flows in practical applications.

Additionally, for the run series TK4M06 with a cavity of aspect ratio  $L/D = 4$  (see appendix A), three-dimensional instabilities do not occur before the onset of the two-dimensional shear-layer oscillation. These results can be interpreted also in terms of critical Reynolds number; that is, the Rossiter mode has a lower critical Reynolds number than the three-dimensional mode for  $L/D = 4$  under these conditions, and vice versa for shorter cavities.

### Boundary layer thickness

Our results show that the parameter  $L/\theta_0$  controls whether the base flow permits three-dimensional instability, and impacts the oscillation frequency (see details in § 3.2.3). A closer inspection of the three-dimensional linearized Navier–Stokes equations reveals that the influence of this parameter should be limited to its effect on the base flow. Comparisons between the subcritical runs TK2M0325Re100 (figure 3.13(a)) and 2M0325 (figure 3.13(b)) show that, when the initial boundary layer momentum thickness is reduced while keeping the other parameters  $Re_D$ ,  $M$  and  $L/D$  constant, the strength of the recirculating region in the 2D base flow increases. In the latter case, three-dimensional instabilities eventually develop.

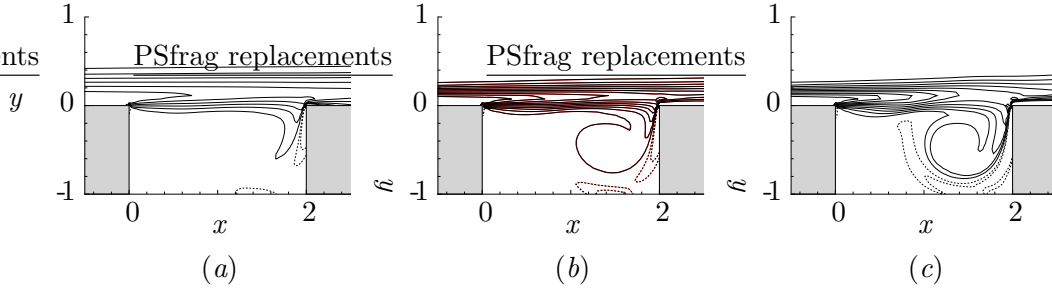


Figure 3.13: Vorticity contours for 2D steady and time-averaged base flows. Equally spaced contours between  $\omega_z D/U = -5$  and 1 are shown. Positive contours are dashed; (a) run TK2M0325Re100. The thick initial boundary layer leads to a weaker recirculating vortical flow within the cavity and no three-dimensional mode; (b) (—) run 2M01, (—) run 2M0325. The difference between the two solutions is less than 1%. Both simulations exhibit identical three-dimensional instabilities; (c) run 2M06. The supercritical case exhibits a similar base flow in a time-averaged sense.

These observations suggest again that a critical strength of recirculating flow in the two-dimensional steady base flow needs to be reached for the presence of 3D instabilities.

### Mach number

From figures 3.10 and 3.11, it is clear that properties of the dominant three-dimensional mode are essentially independent of the Mach number for subcritical conditions over subsonic speed up to 0.6. A set of numerical experiments, presented in appendix B, confirmed this result. This is a substantially different behaviour than the Rossiter modes. It indicates that the instability is unrelated to acoustic waves and other effects of compressibility. It is also consistent with the observation that the 3D instability is active in the recirculating region within the cavity where the flow speed is much lower than the freestream value.

As a result, the critical conditions for the onset of the 3D instability are expected to be nearly independent of the Mach number, at least up to  $M = 0.6$ .

In figure 3.6, the critical Reynolds number  $Re_D \approx 1300$  is estimated at  $M = 0.3$  from the run series 2M03, and is assumed to remain constant for the range of Mach number  $0 < M < 0.4$ , up to the limit of two-dimensional stability.

These results also suggest that the proper scaling for the velocity may not be the freestream velocity but rather some characteristic velocity inside the cavity. Alternate scalings are considered in § 4.2.

### 3.2.3 Eigenmode structure

The unstable eigenfunction for run 2M0325 is depicted in figure 3.14 and is representative of all the three-dimensional unsteady instabilities. A cycle of growth and decay of the disturbance can be observed, as it rotates around the primary vortex of the two-dimensional base flow in the downstream half of the cavity. Starting from the cavity trailing edge, a zone of strong growth exists near the downstream wall where the shear layer impinges the cavity corner. As the fluid in the cavity recirculates upstream and towards the bottom of the cavity, the disturbance amplitude decays slightly, before growing again when moving away from the bottom wall and toward the shear layer. In the shear layer, the perturbation is then damped and convected downstream until it reaches the cavity corner and starts this cycle again. Overall, a larger growth rate than decay rate in this process leads to reinforcement of the disturbance and ultimately instability.

For visualisation purposes, two spanwise periods of the unstable mode of wavelength  $\lambda/D = 1$  are shown in figure 3.15. The perturbation velocity in the  $z$ -direction  $w'/U$  is represented by the iso-surfaces. In general, the spanwise structure of the flow is reminiscent of the cellular pattern observed in experiments and in oil flow visualisations (e.g., Maull & East, 1963).

Another distinctive characteristic of the three-dimensional instability is that the oscillation frequency is about an order of magnitude smaller than the typical frequency of the two-dimensional shear-layer (Rossiter) mode. A detailed inspection of the base flow properties shows that the mode frequency is related to the closed streamlines in the primary vortex. The time for a disturbance to advect

around the recirculating flow is computed for a discrete set of streamlines, and the corresponding nondimensionalised frequencies are compared to the instability frequency from the linear stability analysis. Under most conditions, there is a region in the primary vortex where the frequency computed from the streamline matches the mode frequency. Such streamline is presented in figure 3.14 and shows good agreement with the motion of the disturbances. The smaller average velocity along these streamlines (typically 5 to 10% of the freestream velocity, as shown in figure 4.2(b)) also accounts for the low frequency measured.

This feature of the base flow also sheds light on the dependence of the predicted instability frequency with the flow parameters. In figures 3.10, 3.11, and 3.12, similar trends are observed when the base flow is modified through an increase of the Reynolds number or of the incoming boundary layer thickness: that is, the oscillation frequency decreases for higher  $Re$  or smaller  $L/\theta_0$ . In all these cases, the strength of the recirculating region in the cavity decreases, so the travel time of disturbances in the primary vortex increases, leading to higher 3D mode frequencies. We note that this effect is, however, moderate and it is not expected that the oscillation frequency would be significantly altered for supercritical conditions. In the range of conditions considered, the properties of the two-dimensional steady and time-averaged base flow for sub- and supercritical cases were comparable.

Additionally, our linear results suggest that there could be a significant interaction between the shear layer and the three-dimensional instabilities in practical flows. In figure 3.14, it is clear that the three-dimensional disturbances affect a large portion of the shear layer, even beyond the cavity downstream corner, as the dotted line represents the limit of the shear-layer thickness in the base flow. The extent of these nonlinear interactions in high Reynolds number flows is largely unknown at this stage. Nevertheless, one can speculate that they could potentially be used to design a controller that would tap into the three-dimensional instability to control the shear-layer mode oscillation.

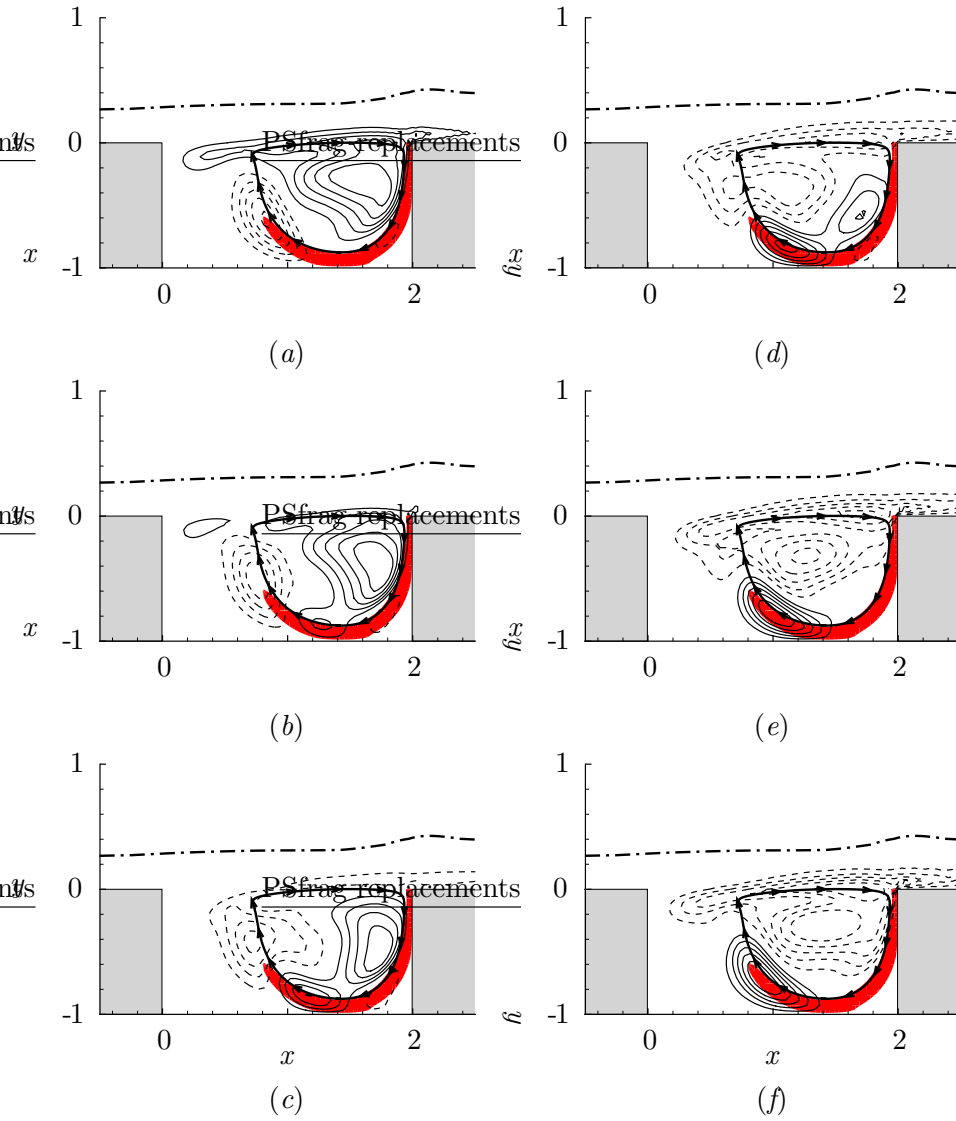


Figure 3.14: Contours of the linearized perturbation velocity  $u'/U$  for the unstable eigenfunction of spanwise wavelength  $\lambda/D = 1$  for run 2M0325. Six times (a-f) are shown, corresponding to half a time period of the 3D instability. The velocity levels are arbitrary and the negative contours are dashed. The red flooded region indicates the zone of potential centrifugal instability discussed in chapter 4. Other features of the 2D base flow: ( $\rightarrow$ ) streamline, (— —) shear-layer thickness

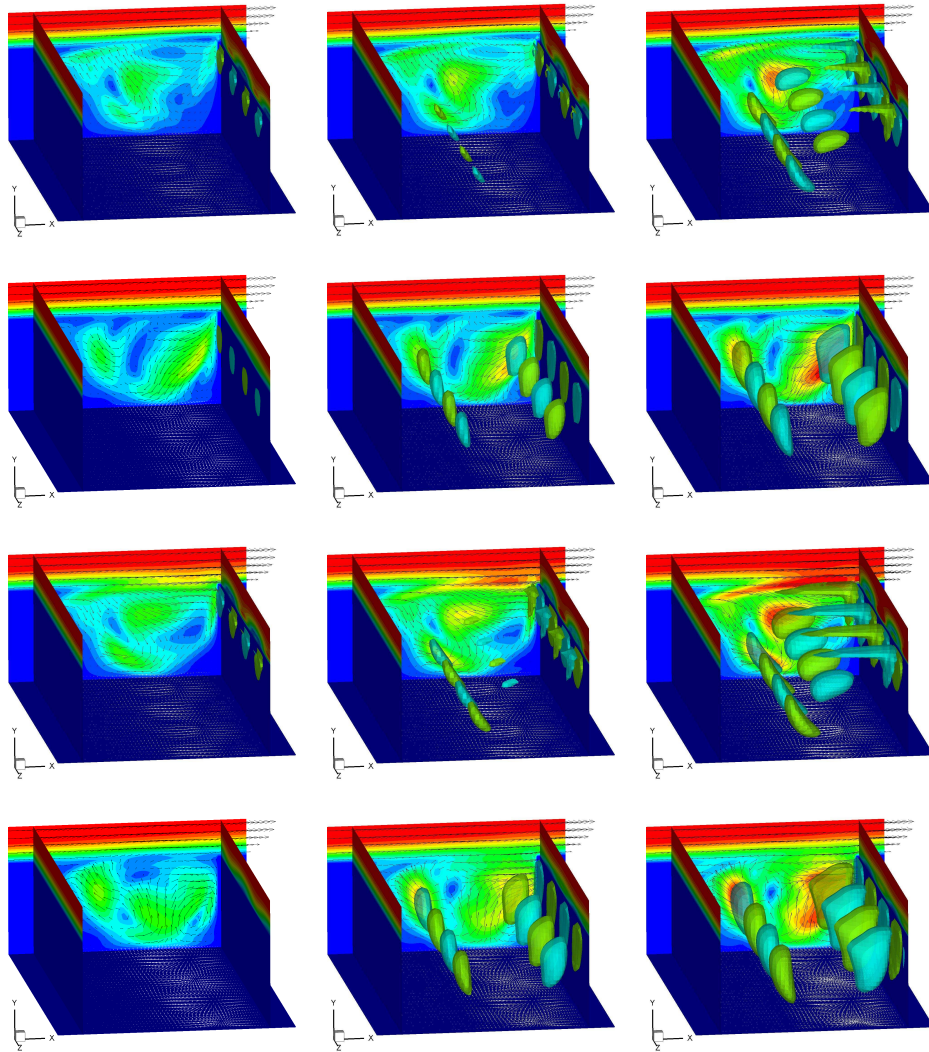


Figure 3.15: 3D visualisation of three periods of the unstable mode of spanwise wavelength  $\lambda/D = 1$  for run 2M0325. For visualization purposes, the amplitude of the 3D linear mode is increased to approximately 20% of the freestream amplitude and was added to the basic steady state flow. The color contours represent the total (steady flow and perturbation) velocity magnitude, and velocity vectors are shown on the streamwise cross section at  $z = 0$  and on the bottom of the cavity. On each plot, two spanwise periods of the unstable mode are shown and the spanwise perturbation velocity  $w'/U$  is represented by the iso-surfaces. One time period of the instability is shown on each column, with time increasing from top to bottom, and left to right.

## Chapter 4

### Centrifugal Instability

#### 4.1 Instability mechanism

We now address the mechanisms of three-dimensional instability. The linear results indicate that the instability depends on the strength of the recirculating region in the downstream half of the cavity. We argue here that the instability mechanism is the generic centrifugal instability associated with the closed streamlines in the recirculating vortical flow near the downstream cavity wall.

##### 4.1.1 Rayleigh's circulation criterion

The centrifugal instability problem was first considered for swirling inviscid flow by Rayleigh, who derived the now celebrated Rayleigh's circulation criterion for stability (e.g., Drazin & Reid, 1981). The classical theory for circular streamlines was generalized to two-dimensional inviscid flow by Bayly (1988). For the centrifugal instability to occur, a sufficient condition is that the magnitude of the angular velocity decreases outward in some region of the flow with closed streamlines. Barkley *et al.* (2002) applied this theory to three-dimensional instability in the flow over a backward-facing step. Following their notation, the Rayleigh discriminant is defined as

$$\eta(x, y) = -\frac{\partial \|\mathbf{r}(x, y) \times \bar{\mathbf{u}}(x, y)\|^2}{\partial r}, \quad (4.1)$$

where  $\mathbf{r}(x, y) = (x - x_c, y - y_c)$ , with  $(x_c, y_c)$  the center about which the angular velocity is defined, and  $r = \|\mathbf{r}(x, y)\|$ . The velocity is simply  $\bar{\mathbf{u}}(x, y) = (\bar{u}, \bar{v})$ . In practice, the center  $(x_c, y_c)$  was chosen to be the approximate location of the minimum velocity inside the recirculating region inside the cavity. The discriminant  $\eta$  is actually only weakly dependent on the choice of the center of rotation: computations with  $\pm 10\%$  error on  $(x_c, y_c)$  lead to similar results. The flow is centrifugally unstable in the inviscid limit where  $\eta > 0$ .

### 4.1.2 Rayleigh discriminant

Figure 4.1 shows the Rayleigh discriminant of the 2D steady (or time-averaged) base flow for different cavity configurations. The contours represent only the region where  $\eta$  is greater than 5% of its maximum value. Additionally, the streamlines are plotted to visualise the flow. The zone where the angular velocity decreases radially corresponds to the downstream part of the recirculating flow near the cavity wall. It also corresponds to the region of maximum growth of the disturbance, as discussed in the previous section. The fluid in the recirculating flow experiences a regime similar to solid-body rotation, with velocity and circulation along the streamlines increasing linearly with the distance to the center of rotation (see figure 4.2). Intuitively, the presence of the downstream and bottom walls forces a rapid decrease in momentum at the outer streamlines. Because of the wall, the fluid is driven in the spanwise direction to form the structures observed in figure 3.15. As the walls are an intrinsic part of all configurations, any cavity flow should be inherently unstable because of the centrifugal instability mechanism, and our simulations do show regions of positive Rayleigh discriminant even for three-dimensional stable cases. However, the centrifugal stability criterion is only a sufficient condition for inviscid flow. As the parametric study of the Reynolds number effect showed, viscosity plays a stabilizing role. In general, simulations with a higher  $Re$  lead to larger values and broader zones of positive Rayleigh discriminant. This result is consistent with the higher linear growth rate of the instability measured in these cases.

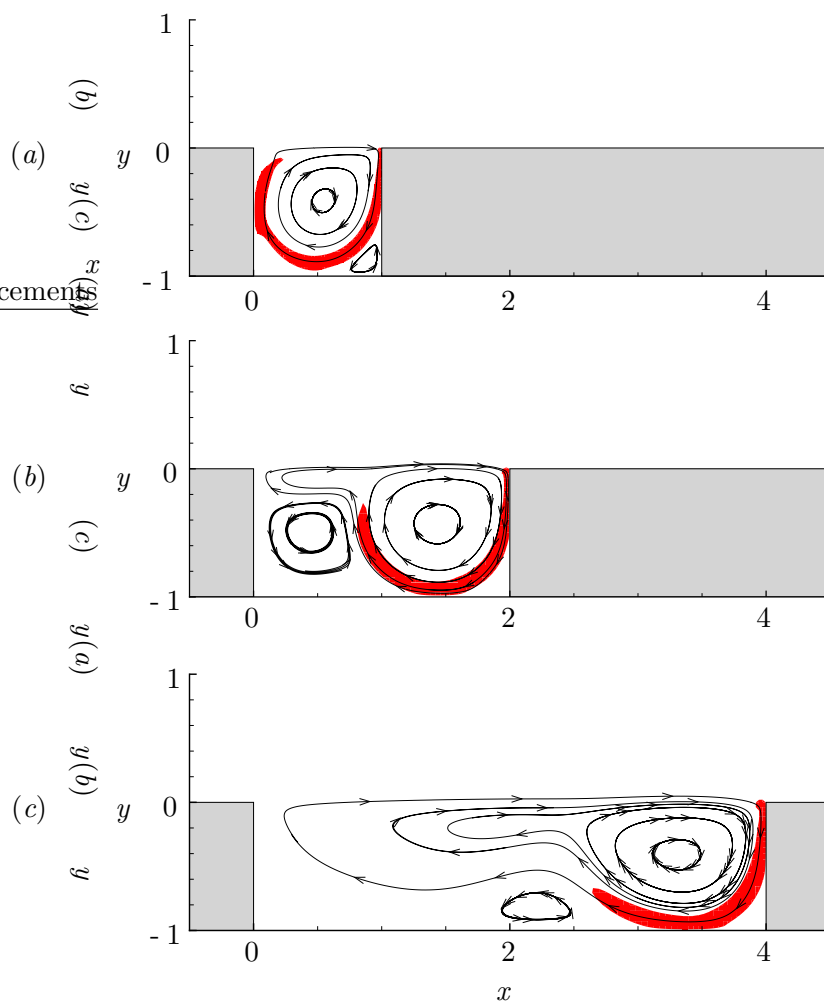


Figure 4.1: Streamlines and Rayleigh discriminant of two-dimensional steady (or time-averaged) base flow. The red flooded region indicates where  $\eta$  is greater than 5 % of its maximum value. (a) run H1Re200; (b) run 2M06; (c); run TK4M03Re65. Cases (a),(c) are 2D subcritical and (b) is supercritical.

Likewise, two-dimensional time-averaged base flows at supercritical conditions exhibit similar regions of potential centrifugal instability. Comparison of the Rayleigh discriminant between the subcritical run 2M0325 in figure 3.14 and the supercritical run 2M06 in figure 4.1(b) shows comparable results, with a slight increase in the levels and extent of the instability zone in the latter case. This observation suggests again that the centrifugal instability mechanism is relevant for cavity flow vortices (in a time-averaged sense) at higher Reynolds numbers.

As mentioned previously, cavities with aspect ratio  $L/D = 1$  feature slightly different characteristics. The recirculating vortical flow now occupies the whole cavity and the motion of disturbances in that vortex is affected not only by the downstream and bottom walls, but by the upstream wall as well. The computation of the Rayleigh discriminant reflects these distinctive features. It is clear in figure 4.1(a) that the region of potential centrifugal instability is much larger, covering the outward streamlines of the primary vortex from the trailing edge of the downstream wall all the way around back to the shear layer. The influence of the upstream wall is believed to be the main explanation for the differences in the instability spanwise wavelength and oscillation frequency observed between cavities of smaller and larger aspect ratio.

Rayleigh's circulation criterion can also be interpreted in terms of circulation along the closed streamlines. In that case, the flow is centrifugally unstable if the circulation magnitude decreases in the outward direction. To validate our results, the circulation on the closed streamlines around the primary vortex were computed as a function of the distance to the center of rotation. Both independent methods lead to the same result: in the inviscid limit, the flow will develop a three-dimensional centrifugal instability in the primary recirculating vortical flow inside the cavity near the downstream wall.

## 4.2 Connection with other centrifugal instabilities

While this is the first time, to our knowledge, that three-dimensionality connected to centrifugal instabilities has been reported for open cavity flows, past studies of global instabilities did shed some light on that mechanism for similar flow configurations. Most of these studies focused on critical flow conditions for the onset of centrifugal instability and the properties of the resulting three-dimensional mode. To enable direct comparison with our linear results for cavity flows, the critical parameters are linearly interpolated whenever conditions of both sides of the three-dimensional stability transition are available.

### 4.2.1 Flow past a backward-facing step

Barkley *et al.* (2002) considered incompressible flow over a spanwise homogeneous backward-facing step geometry, which can be related with that of a wide cavity at appropriate parameter ranges. The run series TK4M03 for our longest cavity of aspect ratio  $L/D = 4$  at low Mach number  $M = 0.3$  are set up to match the range of Reynolds number and the laminar boundary layer momentum thickness of the step simulations. Barkley *et al.* (2002) discovered the existence of amplified large-scale spanwise-periodic vortical structures in this flow. They argued that the source of the three-dimensionality was the centrifugal instability mechanism within the closed recirculation bubble formed between the lip and the downstream floor of the backward-facing step. Much like our linear stability analysis of the cavity flow, they showed that the flow was linearly unstable to three-dimensional disturbances over a finite range of spanwise wavelengths. The reported critical Reynolds number for the instability  $Re_h = Uh/\nu = 748$  is of the same order as  $Re_D = 960$  for the run series TK4M03 (here  $h$  is the step height similar to the cavity depth  $D$ ). However, their critical three-dimensional mode is steady with a spanwise wavelength  $\lambda/h = 6.9$ , and therefore quite different from the cavity flow result (see table 4.1).

As the three-dimensionality in both cases is believed to arise from the recir-

culating flows in the step separation zone and downstream half of the cavity, a possible source of these discrepancies is the differences between the closed streamlines in both flows. For the run series TK4M03, the characteristic dimension of the recirculation vortical flow inside the cavity is again the cavity depth  $D$  and, for the most part, the closed streamlines are approximately circular. In contrast, the streamlines in the step separation zone in the simulations by Barkley *et al.* (2002) are elliptical, with minor axis of dimension  $h = D$  and a much larger major axis  $13h$  corresponding approximately to the reattachment point of the flow, which is a linearly increasing function of the Reynolds. This significant change of geometry could be the cause of the variations in the 3D mode properties.

#### 4.2.2 Lid-driven cavity flows

The lid-driven cavity (LDC) also features three-dimensional centrifugal instabilities (e.g., Albensoeder *et al.*, 2001). While cavity flows exhibit a much richer variety of fluid dynamic processes (shear-layer instabilities, vortex-surface interaction, acoustic waves propagation) compared to traditional incompressible bounded lid-driven flows, the two-dimensional steady base flows obtained from simulations of subcritical cavity flows are in fact similar to the corresponding LDC basic flow. Numerous representations of the two-dimensional streamlines in lid-driven cavity configurations at different Reynolds numbers are available in the literature (see Ramanan & Homsy (1994); Ding & Kawahara (1999) for square cavity; and Albensoeder *et al.* (2001) for cavity of aspect ratio 4). These results can be related to the basic cavity flows in figure 4.1. Because of the presence of a comparable recirculating region in both flows, similar trends can be expected for the stability of LDC and cavity flows. Several experimental and numerical studies have reported three-dimensional modes in square LDC flow and measured the corresponding critical conditions. Additionally, for lid-driven cavities of aspect ratio 1, 2, and 4, detailed linear stability analysis were conducted by Albensoeder *et al.* (2001) and Theofilis *et al.* (2004). All the results are presented in table 4.1.

However, since there is no direct correspondence between the Reynolds number

$Re_D = UD/\nu$  defined for the cavity flow and  $Re_{lid} = U_{lid}D/\nu$  for the lid-driven flow, comparisons remain qualitative. A different scaling than the freestream velocity is considered here, to enable a closer comparison with LDC results. The average streamwise velocity along the cavity mouth at  $y = 0$  is computed for each two-dimensional steady basic flow field, and is interpolated from the critical conditions. The critical Reynolds numbers and frequencies are then rescaled using that average velocity  $U_{lid}$  and are shown in table 4.1. While the traditional nondimensionalisation leads to a range of critical conditions strongly dependent on the cavity aspect ratio and the initial boundary layer momentum thickness, the rescaled results have the same order of magnitude, independently of the cavity configuration. The average velocity  $U_{lid}$  is typically 5 to 15% of the freestream velocity, which accounts for the lower critical Reynolds number  $Re_{lid}$  and higher corresponding frequency  $St_{lid}$ . There is also a closer agreement between the LDC and cavity flow results.

### 4.2.3 Couette flow

Another alternative scaling for the velocity is based on the observation that the recirculating vortical flow inside the cavity exhibits characteristics similar to a solid-body rotation away from the walls (as confirmed by PIV measurements from Chatellier *et al.*, 2006). This feature suggests that the cavity flow could be compared to the special case of Couette flows where the inner cylinder of radius  $R_1$  rotates with constant angular velocity  $\Omega_1$  while the outer cylinder of radius  $R_2$  is at rest. This is particularly relevant for the square cavity, where the recirculating flow occupies the whole cavity and plays the role of the inner cylinder while the cavity walls correspond to the stationary outer cylinder. The stability of such flow has been widely studied and is often mentioned as a classical example of centrifugal instabilities.

DiPrima *et al.* (1984) computed the critical values of the Reynolds number and corresponding axial wavenumber as a function of the radius ratio  $R_1/R_2$  for axisymmetric stationary modes. Note that their results were made dimensionless

by scaling length with the gap width  $d = R_2 - R_1$  and velocity with the inner cylinder velocity  $\Omega_1 R_1$ . To enable comparison with the Couette flow stability results, closed streamlines inside the recirculating flow are extracted and the average velocity along each streamline is computed. From figure 4.2(b), it is clear that the fluid in the vortex rotates with nearly constant angular velocity, as the average velocity along the inner streamlines is proportional to the distance from the center of rotation until the influence of the solid wall is felt, leading to the approximate definition of the convective velocity scale  $U_C = \Omega_1 R_1$ . Note that the objective here is only to achieve qualitative comparison, as it is not possible to unambiguously define  $R_1$  and  $R_2$  for the cavity flow.

We estimated the radius ratio for run H1Re140, which is the last available condition from our linear stability analysis before the stationary mode of wavelength  $\lambda = 0.5$  becomes unstable. From DiPrima *et al.* (1984), the corresponding critical Reynolds number and wavenumber are 317 and 0.46 respectively, in units of  $D$  and  $U_C$ . These values are comparable to the square cavity flow data in table 4.1, highlighting once more the centrifugal character of the 3D instabilities. Similarly to the previous nondimensionalisation inspired by the LDC flows, the rescaled results for the different cavity configurations have the same order of magnitude.

The stability results for the LDC and Couette flow also shed light on the particular properties of the instability in cavities of aspect ratio 1, that is the critical conditions correspond to a stationary mode of smaller spanwise wavelength, about  $0.5D$ . Based on the Couette flow analogy, these results suggest that this stationary mode is amplified in the particular configuration where the recirculating region occupies the whole cavity and interacts with all the cavity walls. Hence the unstable non-oscillatory mode of wavelength 0.4 reported in our linear stability analysis for  $L/D = 1$  cavities, and not for cavities of larger aspect ratio.

Finally, while this analysis makes clear the role of centrifugal instability in cavity flows, we note that it is not predictive in the sense that  $U_{lid}$ ,  $U_C$ ,  $R_1$ , and  $R_2$  have to be estimated from the 2D steady (or time-averaged) base flow.

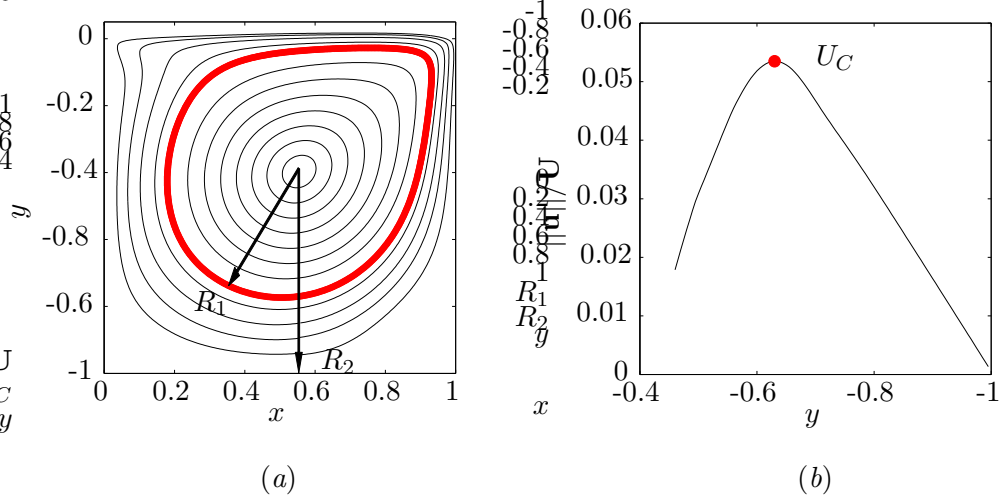


Figure 4.2: Properties of the 2D steady base flow in run H1Re140 for comparison with Couette flow: (a) Streamlines (only one streamline out of 5 is shown); (b) Magnitude of the average velocity  $\|\mathbf{u}\|/U$  along the streamline going through  $(x_c = 0.55, y)$ ; (•) end of the solid-body rotation regime. The corresponding Couette flow cylinder radius  $R_1$  and  $R_2$ , as well as the new velocity scale  $U_C$ , are shown.

$L/D = 1$		$\lambda/D$	$Re$	$Re_{lid}$	$Re_C$	$St_D$	$St_{lid}$	$St_C$
LDC	Albensoeder <i>et al.</i> (2001)	0.408	-	786	-	-	0	-
	Albensoeder <i>et al.</i> (2001)†	0.398	-	810	-	-	0	-
	Theofilis <i>et al.</i> (2004)	0.409	-	782	-	-	0	-
Couette	DiPrima <i>et al.</i> (1984)	0.46	-	-	317	-	-	0
OC	run series H1	0.5	4120	382	209	0	0	0
	run series H1M03	0.4	4060	377	208	0	0	0
LDC	Aidun <i>et al.</i> (1991)††	$\approx 1$	-	875	-	-	0.111	-
	Ramanan & Homsy (1994)	1.047	-	730	-	-	0.100	-
	Ding & Kawahara (1999)	0.849	-	920	-	-	0.079	-
	Albensoeder <i>et al.</i> (2001)	0.848	-	933	-	-	0.078	-
	Theofilis <i>et al.</i> (2004)	0.849	-	922	-	-	0.079	-
OC	run series H1M03	1	5900	452	277	0.010	0.130	0.213

$L/D = 2$		$\lambda/D$	$Re$	$Re_{lid}$	$Re_C$	$St_D$	$St_{lid}$	$St_C$
LDC	Albensoeder <i>et al.</i> (2001)	1.182	-	353	-	-	0.092	-
	Theofilis <i>et al.</i> (2004)	1.102	-	360	-	-	0.093	-
OC	run series 2M03	1	1300	200	144	0.026	0.169	0.235
	run series TK2M0325	1	2000	198	133	0.016	0.160	0.237
	run series TK2M06	1	1990	198	140	0.017	0.166	0.235

*continued on next page*

	$L/D = 4$	$\lambda/D$	$Re$	$Re_{lid}$	$Re_C$	$St_D$	$St_{lid}$	$St_C$
LDC	Albensoeder <i>et al.</i> (2001)	1.220	-	288	-	-	0.091	-
	Theofilis <i>et al.</i> (2004)	1.257	-	290	-	-	0.090	-
OC	run series 4M03	1.25	2370	176	118	0.012	0.158	0.236
	run series TK4M03	1.25	960	146	110	0.026	0.172	0.229
BFS	Barkley <i>et al.</i> (2002)	6.9	750	-	-	0	-	-

Table 4.1: Critical conditions of the 3D centrifugal instability for flows over a backward-facing step (BFS), lid-driven cavity (LDC), Couette and open cavity (OC) flows for different aspect ratio. For  $L/D = 1$ , critical conditions for both steady and unsteady modes are reported. The Reynolds number and nondimensionalised frequency are defined as  $U_*D/\nu$  and  $fD/U_*$ , where different velocity scales  $U_*$  are considered for the cavity flows: the freestream velocity  $U$ , the average velocity  $U_{lid}$  along the cavity at  $y = 0$ , and the maximum average velocity  $U_C$  along the closed streamlines of the two-dimensional base flow vortex, as defined in § 4.2.3. † Experimental results ‡ Mode frequency estimated by Benson & Aidun (1992).

## Chapter 5

### Nonlinear Three-Dimensional Simulations

To investigate the effect of these instabilities on real flows, full three-dimensional nonlinear simulations are performed. Both subcritical (run 2M0325-3D) and supercritical conditions (runs 2M06-3D and H1Re300-3D) are considered. For the 3D simulations, the steady (or time-averaged) basic state  $\bar{q}(x, y)$  extracted from the two-dimensional DNS data is perturbed by small disturbances of spanwise wavelength  $\lambda/D = 2$  and  $\lambda/D = 1$ , corresponding to the first two spanwise wavenumbers in the 3D simulation. The full NS equations are then numerically solved on a homogeneous three-dimensional cavity of spanwise extent  $\Lambda/D = 2$ . As the linear stability results suggest that the spanwise wavelength of the dominant 3D mode is in the range  $0.4 \leq \lambda/D \leq 1.25$ , such cavity aspect ratio is expected to be sufficient to capture all the flow physics.

For the cavity of aspect ratio  $L/D = 2$ , the grid contains about seven and a half million grid points, with  $(Nx = 120, Ny = 60, Nz = 128)$  points across the cavity in the streamwise, depth and spanwise directions, respectively. The grid size is reduced to about three million grid points, with  $(Nx = 60, Ny = 60, Nz = 128)$  for the cavity of smaller aspect ratio  $L/D = 1$ . In each case, the computational domain extends several cavity depths upstream, downstream, and above the cavity. For validation purposes, some cases were also performed on a coarser mesh with different initial conditions, and led to identical results.

## 5.1 Subcritical conditions

### 5.1.1 3D mode oscillation

The first configuration considered is again the subcritical run 2M0325, for a cavity of aspect ratio  $L/D = 2$  at low Mach and Reynolds number ( $M = 0.325$ ,  $Re_D = 1500$ ,  $L/\theta_0 = 53$ ). The two-dimensional simulation shows that the flow is initially oscillating at a frequency  $St_D = fD/U = 0.241$  close to Rossiter first mode, with exponentially decaying amplitude, and ultimately converges to a steady state. This result is confirmed by the stability analysis. By setting  $\beta = 0$  in equation 2.4, the linear stability of the steady base flow can be investigated for perturbation of spanwise wavelength  $\lambda/D = \infty$  (i.e., two-dimensional perturbations). In that case, the linear growth/damping rate and frequency of the dominant Rossiter mode are recovered. For run 2M0325, the mode is damped and the frequency is  $St_D = 0.240$  (see table 5.1).

Figure 5.1 shows a portion of the time-history of the velocity  $v/U$  for both two- and three-dimensional simulations at approximately the same location in the middle of the cavity. Initially, the three-dimensional flow oscillates at a frequency corresponding to the 2D Rossiter mode. This frequency and its first harmonic are evident in the spectrum in figure 5.2. After a transition period, the 2D modes decay while the 3D mode grows and saturates. The final frequency of oscillation is  $St_D = 0.025$  corresponding to the frequency of the most unstable three-dimensional mode from the linear stability analysis (see table 5.1).

### 5.1.2 Flow structure

The visualisation of the flow structures over half a time-period is presented in figures 5.3 and 5.16. As the shear-layer oscillations are damped and eventually die out, the three-dimensional instability associated to the centrifugal mechanism is the only unsteady feature remaining in the flow: the growth and decay of disturbances rotating around the primary vortex can be observed in the cavity, as can the formation of a cellular pattern similar to the linear stability results. As predicted,

Run	2M0325			2M06		
	2D subcritical			2D supercritical		
$L/D$	2			2		
$Re_D$	1500			1500		
$L/\theta_0$	52.3			52.3		
$M$	0.325			0.6		
	$St_D$	Mode	$\lambda/D$	$St_D$	Mode	$\lambda/D$
Rossiter prediction	0.181	I	$\infty$	0.160	I	$\infty$
	0.422	II	$\infty$	0.372	II	$\infty$
2D DNS	0.241†	I	$\infty$	0.204	I	$\infty$
3D Linear Stability	0.025	$ii$	1	n.a.		
	0.240†	I	$\infty$	n.a.		
3D DNS	0.025	$ii$	1	0.026	$ii$	1
	0.240†	I	$\infty$	0.352	II	$\infty$

Table 5.1: Comparison of the dominant mode prediction for 2D and 3D runs with  $L/D = 2$ . Only the most energetic frequencies  $St_D = fD/U$  for the cavity flows are presented, along with the spanwise wavelength  $\lambda/D$  of the instability. The original values from Rossiter ( $1/\kappa = 1.75$ ,  $\alpha = 0.25$ ) were used in the semi-empirical formula. † For subcritical conditions, the Rossiter modes are damped but the oscillation frequency can still be measured from the early times. The linear stability results are not available (n.a.) for supercritical conditions.

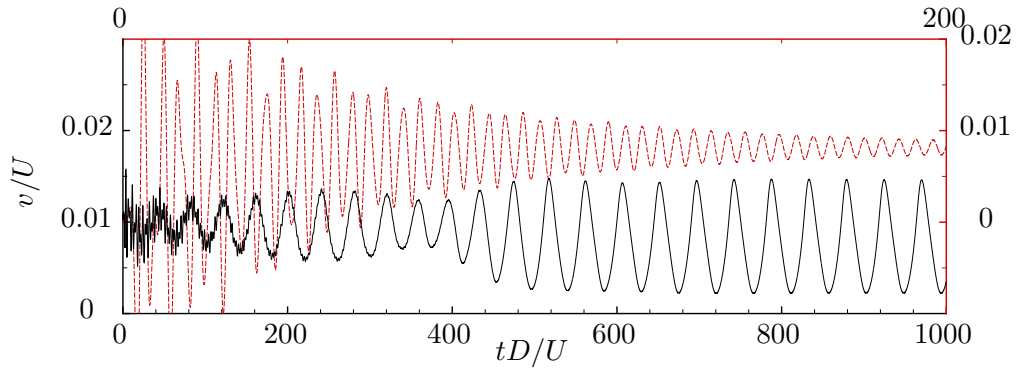


Figure 5.1: Time trace of normal velocity at  $(x, y) = (0.5L, 0)$  for 2D run 2M0325 (---) and 3D run 2M0325-3D (—) at  $z = 0$ . The other flow variables exhibit the same characteristics. To show all the data clearly, the bottom and left axes correspond to the 3D simulation, and the top and right axes to the 2D run.

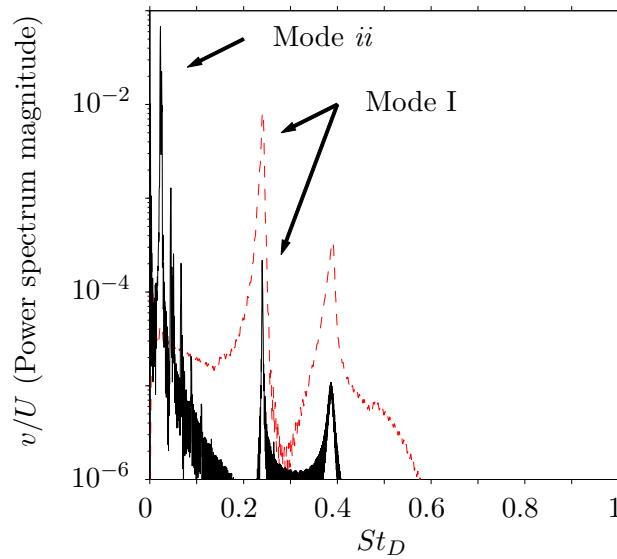


Figure 5.2: Spectrum of the normal velocity presented in figure 5.1: 2D run 2M0325 (---); 3D run 2M0325-3D (—). The different modes are identified and their harmonics can also be observed

the spanwise wavelength of the three-dimensional instability is equal to one cavity depth. Spectral analysis in the spanwise direction shows that the energy spreads to all the other wavelengths (including harmonics) because of the nonlinear terms in the NS equations, but  $\lambda/D = 1$  remains the dominant wavelength.

Most of the three-dimensionality is confined to the internal flow inside the cavity, where the velocities remain small (up to 10% and 15% of the freestream value for the streamwise and normal velocities, respectively). The spanwise velocities in figure 5.3 correspond to only 1% of the freestream velocity. The instantaneous maxima of  $w/U$  are located near the downstream wall inside the cavity and reach about 2.5%. Even smaller levels of spanwise velocity are measured in the shear layer, which remains mostly two-dimensional and stationary, despite the presence of the centrifugal instability. The shear-layer spreading rates for run 2M0325 and 2M0325-3D are shown in figure 5.11: both 2D and 3D simulations exhibit identical linear growth along the whole cavity. The shear layer properties and the measurement of the spreading rate are discussed in more details in § 5.2.3.

### 5.1.3 Time-averaged flow

Because the three-dimensional mode is oscillating about the mean flow, its contribution cancels out in a time-averaged sense: that is, the time-averaged flow does not exhibit the spanwise modulation of wavelength  $\lambda/D = 1$  like the instantaneous flow field does. Figure 5.4 compares the time-averaged velocity field of the 2D run 2M0325 and 3D run 2M0325-3D (also spanwise-averaged). Here, the 3D results deviate from the two-dimensional predicted steady state by less than 2% of the freestream quantities.

In conclusion, the three-dimensional mode predicted by the linear stability analysis is observed in the nonlinear simulation. Under the present conditions, the instability remains weak and is mainly active in the recirculating region within the cavity. The interaction with the shear layer is also weak and mostly limited to a low-frequency, small-amplitude oscillation.

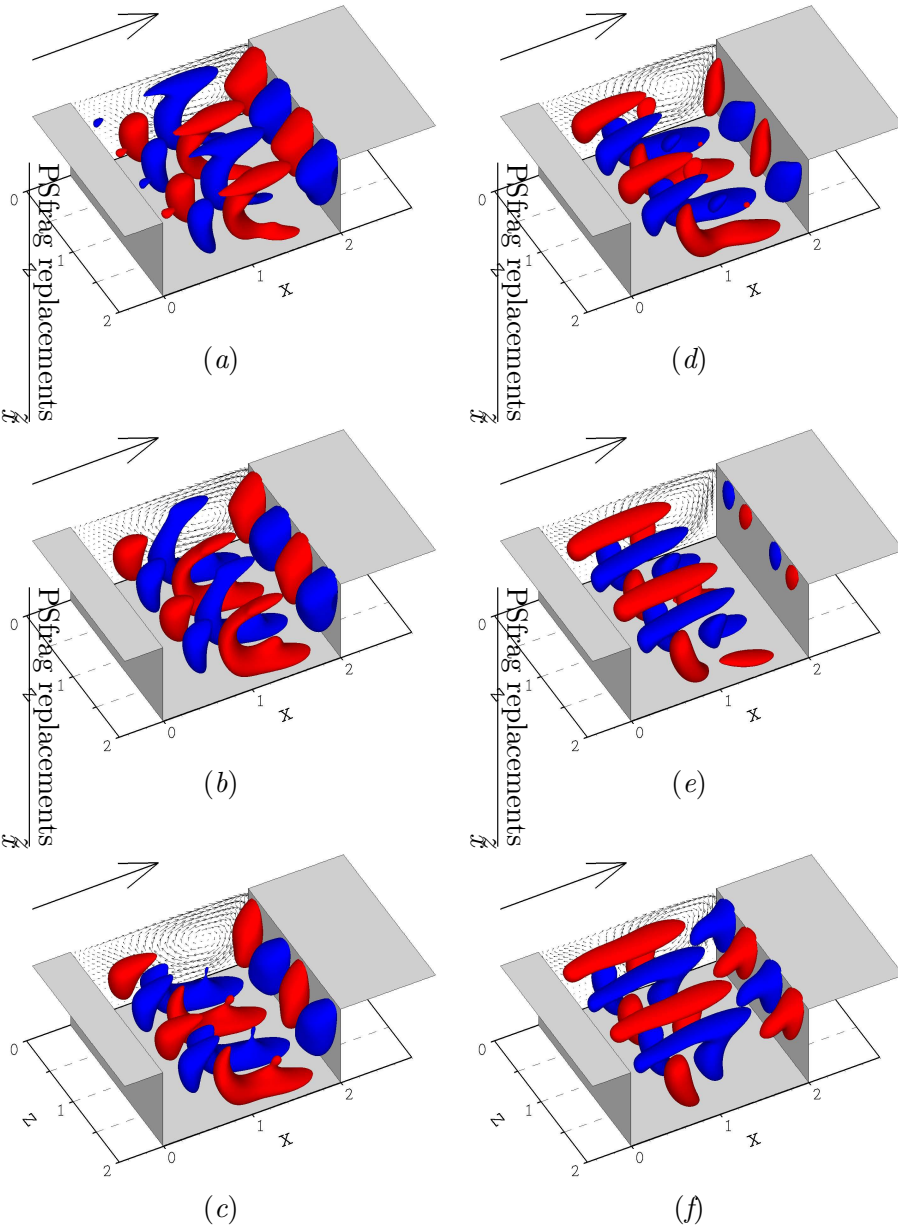


Figure 5.3: Visualisation of the spanwise structures in 3D run 2M0325-3D. Six different times (*a-f*) are shown, corresponding to approximately one-sixth phase intervals of a half-period of the 3D instability. The iso-surfaces represent the spanwise velocity levels  $w/U = -0.01$  and  $w/U = 0.01$ . The whole spanwise extent of the cavity is shown and the wavelength  $\lambda/D = 1$  of the instability can clearly be observed. The velocity vectors in the streamwise cross-section at  $z = 0$  are shown inside the cavity and once in the freestream for comparison.

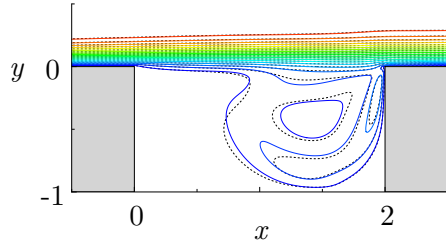


Figure 5.4: Time-averaged velocity field for 2D run 2M0325 (color contours) and 3D run 2M0325-3D ( ---- ). Nineteen equi-spaced contours of the velocity magnitude between  $\|\mathbf{u}\|/U = 0.05$  and  $0.95$  are represented. The spanwise average of the field is shown for the 3D case.

## 5.2 Supercritical conditions

Supercritical conditions were obtained from the previous simulations by simply increasing the Mach number from  $M = 0.325$  to  $M = 0.6$  while keeping the other parameters constant. In run 2M06, the two-dimensional flow exhibits disturbances of growing amplitude and eventually saturates into a periodic oscillating flow of frequency corresponding to the Rossiter mode I. In this case, a time-averaged steady state  $\bar{q}$  is extracted by averaging the periodic data and the 3D nonlinear simulation is performed following the same procedure as the subcritical case.

### 5.2.1 Unsteady flow structure

The flow structure is shown in figure 5.5 for comparison with the subcritical case 2M0325-3D. Both flows exhibit identical three-dimensional features in terms of cellular pattern inside the cavity and oscillation frequency (see § 5.2.2). The velocity field in the cavity is stronger in this case: the maxima of the instantaneous velocity magnitude are between 15 and 25% of the freestream value for the streamwise and normal velocities, and up to 10% for the spanwise velocity. This increase leads to larger iso-surfaces in figure 5.5 compared to figure 5.3, but the dominant spanwise wavelength is still  $\lambda/D = 1$ . Here, the 3D instability can again be identified with mode *ii*.

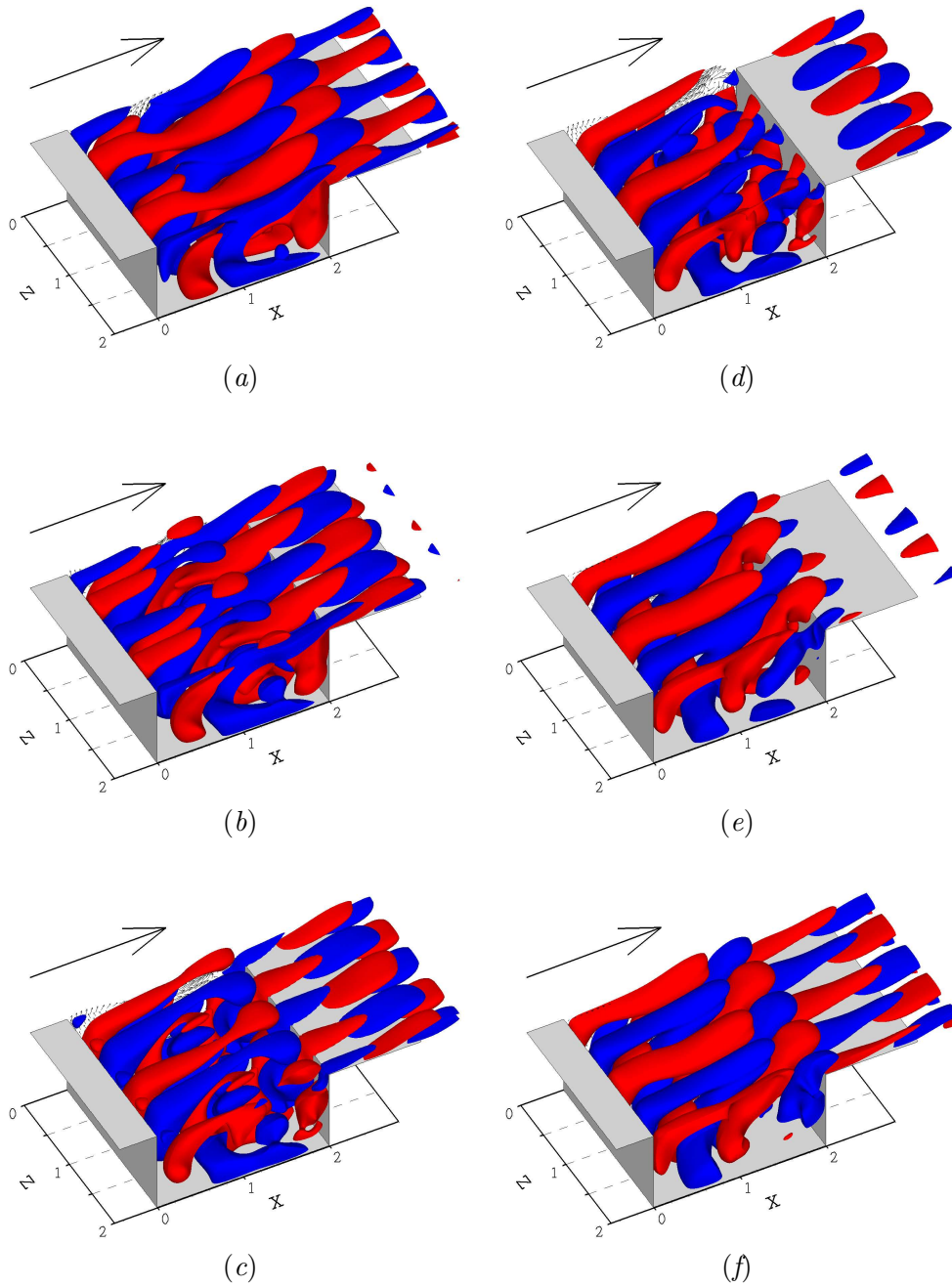


Figure 5.5: Visualisation of the spanwise structures for 3D run 2M06-3D. Six different times (*a-f*) are shown, corresponding to approximately one-sixth phase intervals of a half-period of the 3D instability. The iso-surfaces represent the same spanwise velocity levels as in figure 5.3 ( $w/U = -0.01$  and  $0.01$ ).

For these supercritical conditions, shear-layer oscillations are also present in the 3D simulations and the interaction between the three-dimensional instabilities and the shear layer is significant. In the downstream half of the cavity, the spanwise structures enter the shear layer and impinge on the downstream edge. Part of the disturbances is swept downstream while the other part goes back into the recirculating flow inside the cavity. In general, the spanwise wavelength  $\lambda/D = 1$  of these structures can still be observed as they are convected downstream of the cavity.

### 5.2.2 Oscillation frequencies

The time-history of the streamwise velocity  $u/U$  and the pressure  $P - P_\infty$  for runs 2M06 and 2M06-3D are compared in figures 5.6 and 5.7. It is interesting to note that both Rossiter modes I and II are initially unstable in the two-dimensional simulation, but through a process of nonlinear amplification and saturation, mode I is selected, while mode II is damped and vanishes. In the three-dimensional simulation, after some transient exhibiting both Rossiter modes I and II, the self-sustained oscillations in the flow saturate into a periodic regime where the Rossiter mode II and the three-dimensional instability can be observed simultaneously. The different mode frequencies are reported in table 5.1.

In figure 5.6, it is clear that the shear-layer oscillations exhibit a low-frequency modulations related to the 3D mode. Similar results are obtained in figure 5.8 for the spanwise velocity inside the shear-layer at  $0.5L$  and  $0.9L$  from the leading edge. The interaction between the two modes increases near the downstream wall of the cavity, where the oscillation amplitude is larger and the centrifugal instability stronger. The low-frequency peaks are observed in the power spectra in figures 5.9(a) and 5.10, respectively. Apart from harmonics, additional peaks are present at the frequencies  $f_{II} - f_{ii}$  and  $f_{II} + f_{ii}$ , corresponding to nonlinear interactions between the Rossiter mode II and the 3D mode  $ii$ . For the spanwise velocity, these two frequencies are particularly energetic and the peak at  $f_{II}$  is noticeably absent in the spectra in figure 5.10. We suspect that there is no peak associated with

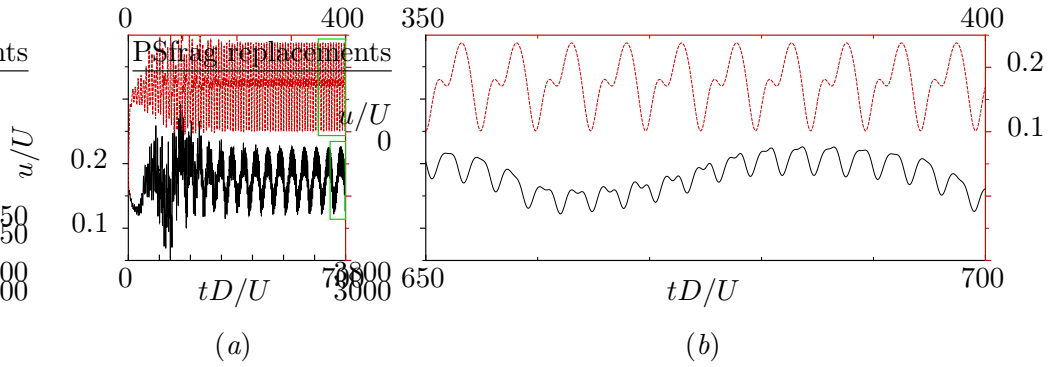


Figure 5.6: (a) Time trace of streamwise velocity at  $(x, y) = (0.5L, 0)$  for 2D run 2M06 (  $---$  ) and 3D run 2M06-3D (  $---$  ) at  $z = 0.25D$ ; (b) Details of the signal in the boxes in (a). To show all the data clearly, the bottom and left axes correspond to the 3D simulation, and the top and right axes to the 2D run.

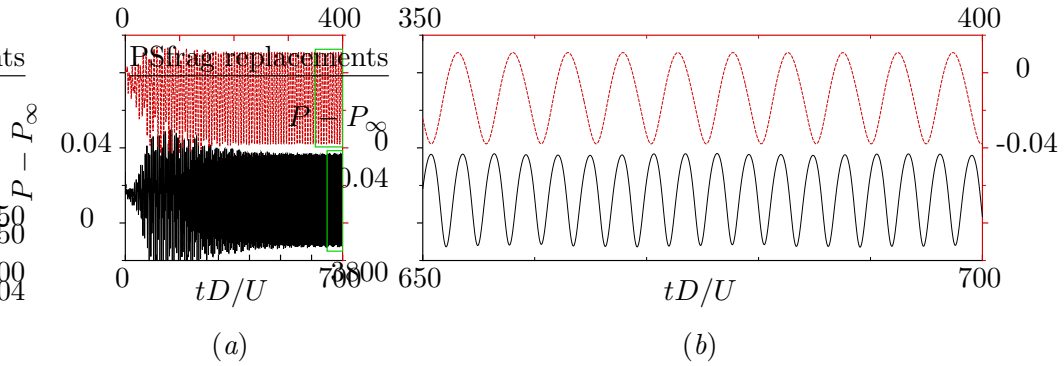


Figure 5.7: (a) Time trace of pressure at  $(x, y) = (0.9L, 0)$  for 2D run 2M06 (  $---$  ) and 3D run 2M06-3D (  $---$  ) at  $z = 0$ ; (b) Details of the signal in the boxes in (a). To show all the data clearly, the bottom and left axes correspond to the 3D simulation, and the top and right axes to the 2D run.

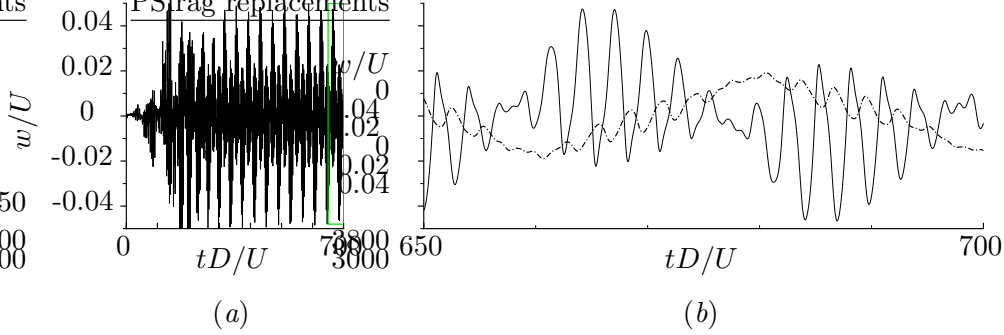


Figure 5.8: (a) Time trace of spanwise velocity at  $(x, y, z) = (0.9L, 0, 0)$  for 3D run 2M06-3D, (b) Details of the signal ( — ) in the box in (a) and of the spanwise velocity at  $(x, y, z) = (0.5L, 0, 0)$  ( - - - )

the Rossiter mode here because there is no mean spanwise velocity in the time-averaged flow. This can be contrasted with the results presented in section § 5.3 where the peak is observed when a steady 3D mode is present.

For the present conditions, the peak associated with the 3D mode is in general about the same energy level or higher than the one for the Rossiter mode in the power spectra of the velocity field components. The low-frequency modulation is less evident in the time trace of the pressure in figure 5.7 and the Rossiter modes are significantly more energetic than the 3D mode in the spectra of the pressure in figure 5.9(b). Here, we argue that the interaction between the Rossiter mode and the three-dimensional instability is stronger for the velocity field than for the acoustic field because of the hydrodynamic nature of the 3D mode. Overall, these results are consistent with the present hypothesis that the 3D modes are related to the centrifugal instability mechanism.

Since the 2D flow is supercritical, linear results for run 2M06 are not available for direct comparison with the three-dimensional mode frequency observed here. However, the low frequency measured here matches the predicted result from the linear stability analysis of run 2M0325 and the 3D mode frequency from run 2M0325-3D. There is no contradiction here, since we showed in § 3.2.1 that the

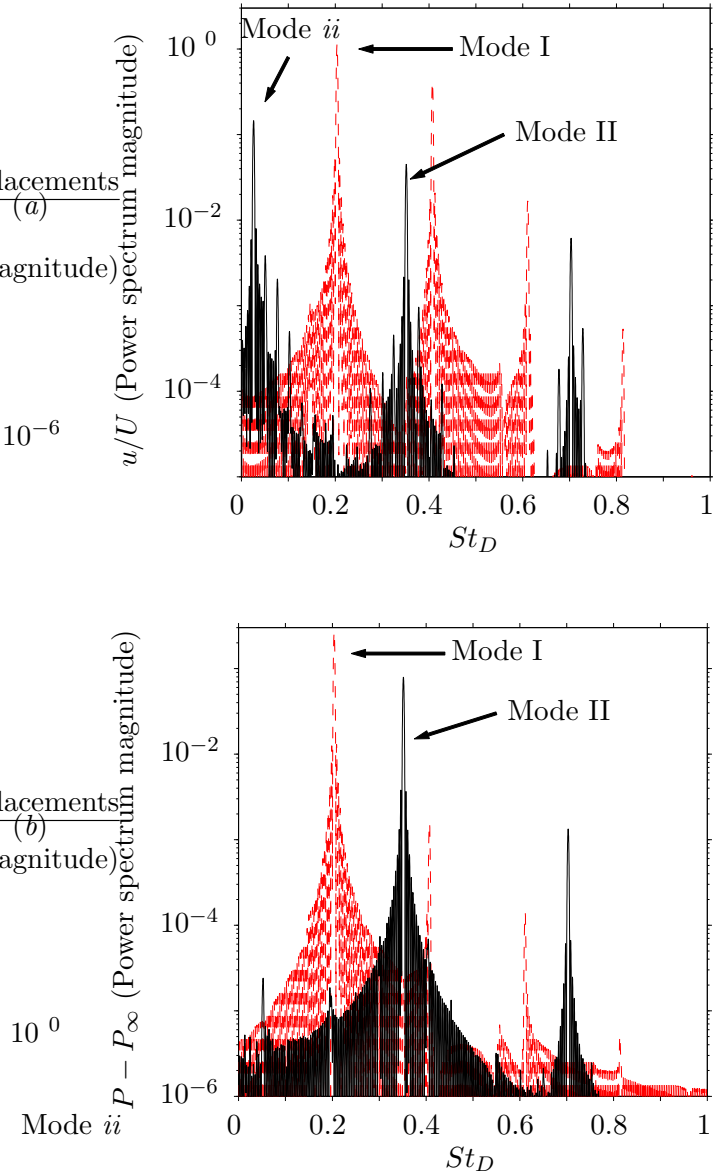


Figure 5.9: Power Spectra of the periodic data presented in figures 5.6 and 5.7: 2D run 2M06 ( - - - - ); 3D run 2M06-3D ( ——— ). The different modes are identified and their harmonics can also be observed. (a) Streamwise velocity, (b) Pressure

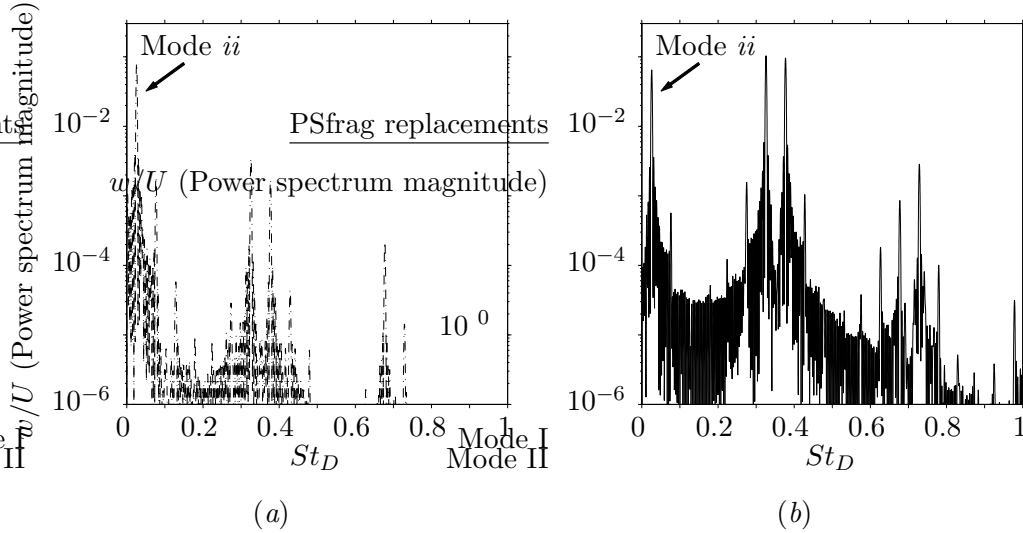


Figure 5.10: Power Spectra of the spanwise velocity presented in figure 5.8 for 3D run 2M06-3D:(a) measurements at  $(x, y, z) = (0.5L, 0, 0)$  ( — — ), (b) measurements at  $(x, y, z) = (0.9L, 0, 0)$  ( — )

Mach number has little influence on the characteristics of the three-dimensional mode. This result is encouraging, as it tends to indicate that linear results from subcritical cases (if such stable conditions exist) could deliver useful insight on the 3D stability at higher Mach number for corresponding supercritical conditions.

### 5.2.3 Shear-layer spreading rate

Another key feature is that the shear-layer oscillation frequency now corresponds to the Rossiter mode II, rather than mode I as is selected in strictly two-dimensional simulations. The higher oscillation frequency of the 3D simulation is clearly observed in figure 5.7(b).

To better assess the instability properties of the shear layer, the vorticity thickness  $\delta_\omega(x) = U / (d\bar{u}(x, y)/dy)_{max}$  is computed, where  $\bar{u}(x, y)$  is the time (and spanwise) average of the streamwise velocity. The vorticity thickness and its slope  $d\delta_\omega/dx$  are typically used to measure the shear-layer spreading rate. Most researchers report that shear layer over open cavities exhibits approximately linear

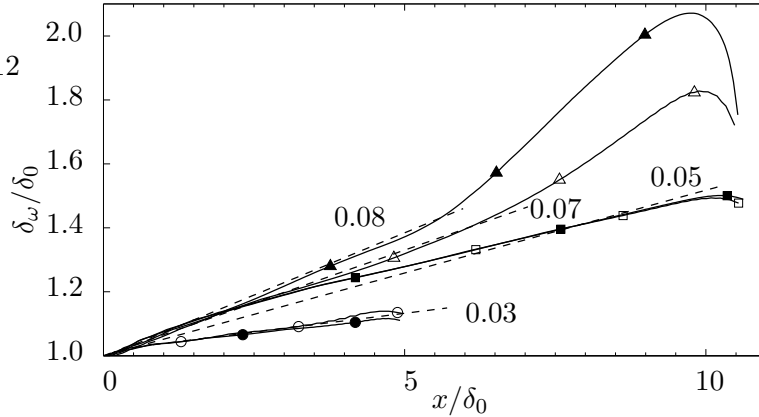


Figure 5.11: Vorticity thickness  $\delta_\omega$  along the shear layer nondimensionalised by the initial vorticity thickness  $\delta_0$ , and average slope  $d\delta_\omega/dx$  (----); runs H1Re300 ( $\bullet$ ) and H1Re300-3D ( $\circ$ ); runs 2M0325 ( $\blacksquare$ ) and 2M0325-3D ( $\square$ ); runs 2M06 ( $\blacktriangle$ ) and 2M06-3D ( $\triangle$ ). For the latter two cases, data for  $x/D > 1$  was not considered in the calculation of  $d\delta_\omega/dx$ .

growth, much like free shear layers. However, the basic physics of these flows differs in two main aspects: that is, the shear layer is subject to a strong acoustic feedback, and the presence of the recirculating vortical flow in the downstream part of the cavity affects the entrainment and alters the shear-layer thickness.

The comparison of the spreading rates in figure 5.11 highlights these key features: for supercritical conditions (such as run 2M06-3D), the shear-layer oscillations lead to a higher initial spreading rate and a sharp increase around  $x/\delta_0 \approx 6$  (i.e.,  $x/D \approx 1$ ), which corresponds to the location of the recirculating region and the region of larger amplitude oscillations. In contrast, for the subcritical run 2M0325-3D with the same initial boundary layer momentum thickness, the spreading rate is approximately linear over the whole cavity and its value is about 25% lower. Also, the influence of the downstream wall is clearly shown for  $x/\delta_0 > 10$  (i.e.,  $x/D > 1.85$ ).

In both runs 2M06 and 2M06-3D, the shear layer initially exhibits linear growth for  $x/\delta_0 < 6$ , but there is a 15% decrease in the spreading rate between the 2D

( $d\delta_\omega/dx \approx 0.08$ ) and 3D ( $d\delta_\omega/dx \approx 0.07$ ) simulations. These results are of the same order as the spreading rates measured in experiments (Sarohia, 1975) and numerical simulations (Rowley *et al.*, 2002*b*). Sarohia’s measurements are based on the momentum thickness  $\theta$  and can be related to vorticity thickness by  $\delta_\omega \approx 4\theta$  (exact equivalence for hyperbolic tangent profiles). As  $L/\theta_0$  is increased from 52.5 to 105.2, Sarohia (1975) observed that the spreading rate  $d\theta/dx$  increased from 0.006 to 0.022, and the cavity oscillation switched from mode I to mode II. Other experimental (e.g., Gharib & Roshko, 1987) and numerical (e.g., Rowley *et al.*, 2002*b*) studies on open cavity flows also report that larger shear-layer spreading rates are obtained as  $L/\theta_0$  is increased, and ultimately lead to higher dominant mode. In the present case, an increase in shear-layer spreading rate does not seem to be the cause of the higher mode observed in the three-dimensional simulation, as the opposite trend can be observed in figure 5.11.

#### 5.2.4 Time-averaged flow properties

The shear-layer measurements are consistent with other observations in the flow field. Here, we argue that the decrease in shear-layer spreading rate is related to the smaller oscillation amplitude and weaker recirculating region in the three-dimensional simulations. As shown in figures 5.6 and 5.7, the oscillation amplitude of the limit cycle slightly decreases between the 2D and 3D simulations. All the other probes located in the shear layer and inside the cavity exhibit the same trend.

Likewise, a decrease in all the Reynolds stresses is observed, especially in the shear layer. Figure 5.12 shows  $u_{rms} = \sqrt{u'u'}/U$ ,  $v_{rms} = \sqrt{v'v'}/U$ , and  $w_{rms} = \sqrt{w'w'}/U$  for the runs 2M06 and 2M06-3D. Here, the superscripts “-” and “'” denote the time averaging and the fluctuating component of the flow variable with respect to the corresponding time-averaged quantity (i.e.,  $u' = u - \bar{u}$ ). The highest levels of  $u_{rms}$  are found in the shear layer in the downstream half of the cavity where the amplitude of oscillation is larger. For  $v_{rms}$ , the highest levels are located near the downstream edge of the cavity because of the impingement process. The maximum amplitude of the *rms* velocity components are respectively 0.13 and

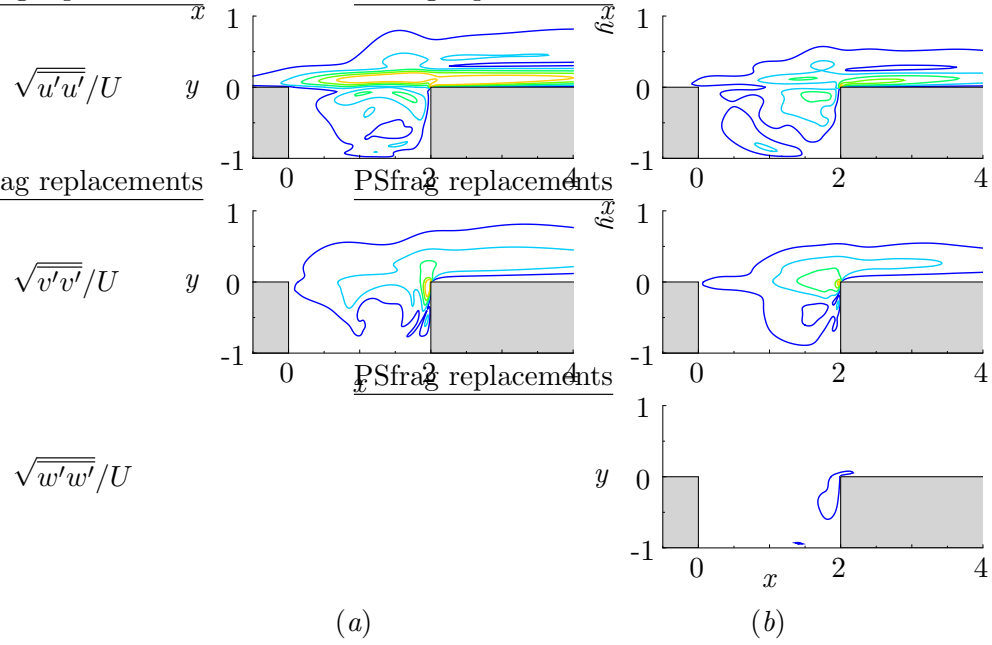


Figure 5.12: Reynolds stresses  $\sqrt{u'u'}/U$ ,  $\sqrt{v'v'}/U$  and  $\sqrt{w'w'}/U$  (from top to bottom): (a) 2D run 2M06; (b) 3D run 2M06-3D. Five equi-spaced contours between 0.02 and 0.1 are represented. The spanwise average is shown for the 3D case.

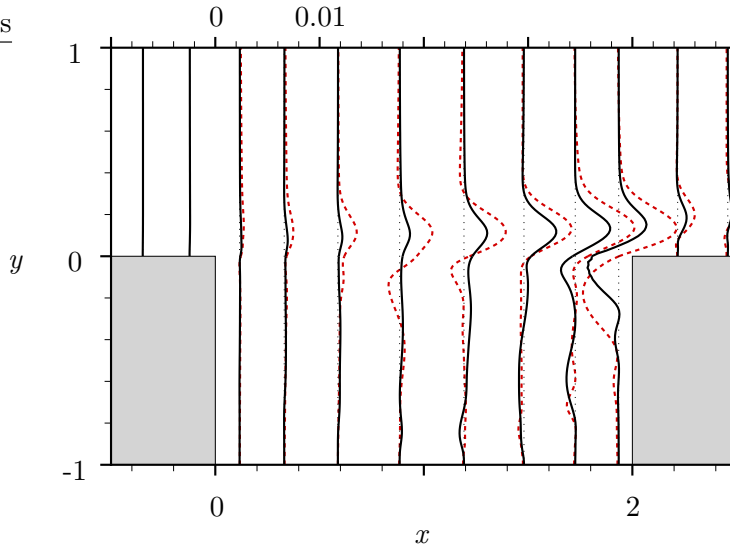


Figure 5.13: Reynolds stress  $\overline{u'v'}/U^2$  for 2D run 2M06 ( - - - ) and 3D run 2M06-3D ( — ). The actual value can be measured from the corresponding dashed line at each location, where the major tick on the horizontal top scale represents 0.01. The other Reynolds stresses  $\overline{u'w'}/U^2$  and  $\overline{v'w'}/U^2$  (not shown) are about three orders of magnitude smaller.

0.17 in the streamwise and normal direction for the 2D simulation. These maxima decrease to 0.1 and 0.12 in the 3D simulation. The quantity  $w_{rms}$  has smaller values than the other *rms* velocities. The maximum amplitude is approximately 0.04 near the downstream wall because of the centrifugal instability mechanism.

Figure 5.13 shows  $\overline{u'v'}/U^2$  for runs 2M06 and 2M06-3D. Again, it is clear that the 2D simulation overestimates the amplitude of the shear-layer oscillations. The mean velocity field inside the cavity is also overestimated: for the three-dimensional computation, the spanwise-averaged velocity magnitude of the primary vortex is less than half of the two-dimensional prediction (see figure 5.14). Overall, the flow variables in the cavity are overestimated by about 5 to 10% of the freestream quantities. Note that, much like the previous case, the contribution of three-dimensional mode cancels out in a time-averaged sense and the time-averaged flow is approximately constant in the spanwise direction.

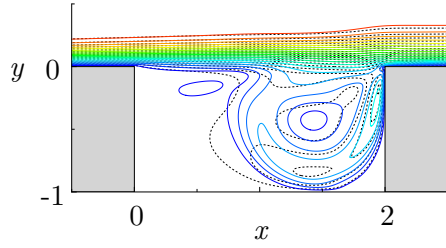


Figure 5.14: Time-averaged velocity field for 2D run 2M06 (color contours) and 3D run 2M06-3D ( ---- ). Nineteen equi-spaced contours of the velocity magnitude between  $\|\mathbf{u}\|/U = 0.05$  and  $0.95$  are represented. The spanwise average of the field is shown for the 3D case.

The sound pressure levels (SPL) for the acoustic field above and inside the cavity in runs 2M06 and 2M06-3D are shown in figure 5.15. While the sound directivity is similar in both cases, with a peak radiation in the far field at about  $135^\circ$  from the downstream direction, the levels are in general lower for the 3D simulation. A noise reduction of about 5 dB can be observed in the far field, and up to 12 dB inside the cavity. This result is related to the decrease in oscillation amplitude previously mentioned. It is also in agreement with the general experimental observation that two-dimensional cavities are slightly louder than their three-dimensional counterparts. The weakened shear-layer coherence caused by turbulence is typically viewed as the key point to explain this experimental trend. A similar argument can be made here, even at lower Reynolds number. As the three-dimensional centrifugal instability establishes itself inside the cavity, the shear layer above develops the same spanwise fluctuations. This result can be seen in the contours of the vorticity magnitude presented in figure 5.17. Spanwise modulations are present in the shear-layer, starting around  $x = D$ . The resulting reduced spanwise coherence of the vortical structures traveling downstream in the shear layer affects the receptivity of the cavity trailing edge, which, in turn, reduces the acoustic scattering, the leading edge reinforcement of disturbances, and the overall effectiveness of the feedback process.

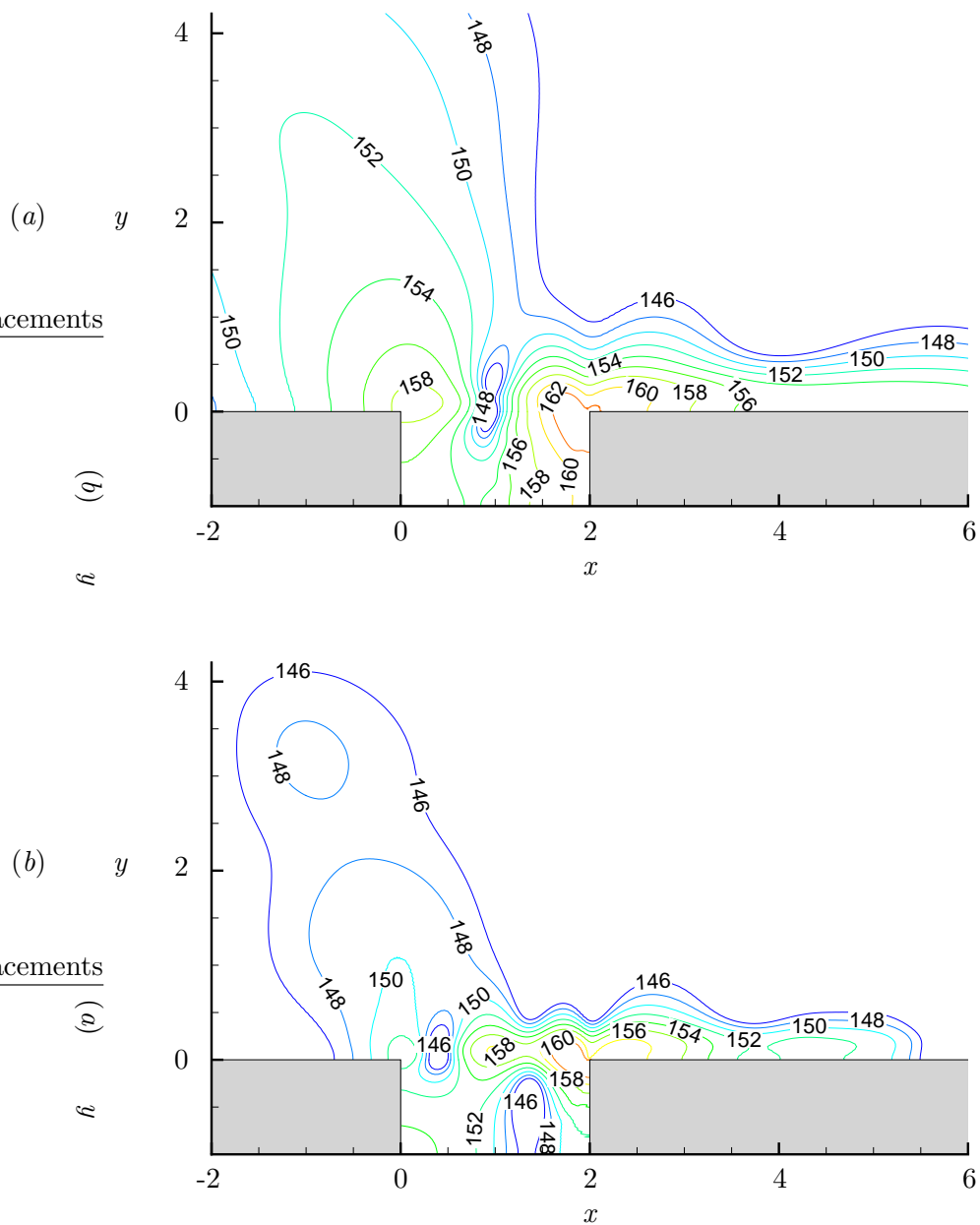


Figure 5.15: Sound pressure levels (SPL): (a) 2D run 2M06; (b) 3D run 2M06-3D. The spanwise average of the SPL is shown in this case.

### 5.2.5 Discussion of the change in oscillation frequency

The change in mode frequency still needs to be addressed. A closer inspection at the spanwise vorticity  $\omega_z = \partial v/\partial x - \partial u/\partial y$  for the two-dimensional simulation 2M06 shows that only one vortex is present at a time in the shear layer across the cavity in agreement with the predicted Rossiter mode I. In contrast, two vortices can in general be observed simultaneously in the vorticity contours along the cavity, in any streamwise cross-section of the three-dimensional simulation 2M06-3D. Looking at the evolution in time of the vorticity in both cases, it appears that the existence of the additional vortex, and therefore the shift in Rossiter mode, is caused by the presence of the three-dimensional instability. Disturbances rotating around the primary vortex in the downstream half of the cavity interact with the shear layer around  $x = 0.5L$ , likely leading to the change in the streamwise wavelength from  $\lambda_x/L = 1$  to  $\lambda_x/L = 0.5$ .

In conclusion, both shear-layer oscillations and 3D mode are observed in the nonlinear simulation for the supercritical conditions of run 2M06-3D. Much like the previous case 2M0325-3D, spanwise structures of wavelength  $\lambda/D = 1$  form inside the cavity and the three-dimensional mode corresponds to mode *ii* predicted by the linear stability analysis. These features can be clearly seen by comparing the flow inside the cavity in figures 5.16 and 5.17. Overall, the 2D simulation overestimates the amplitude of the shear-layer oscillations and of the flow field inside the cavity. Also, the shear-layer oscillations switch from Rossiter mode I (in the 2D simulations) to mode II, and experience a low-frequency modulation caused by the presence of the 3D mode. The results suggest that the interactions between the 2D and 3D modes seem to lead to the selection of that particular Rossiter frequency. Such observation could potentially be used to shed some light on the physics of mode selection in self-sustained oscillations.

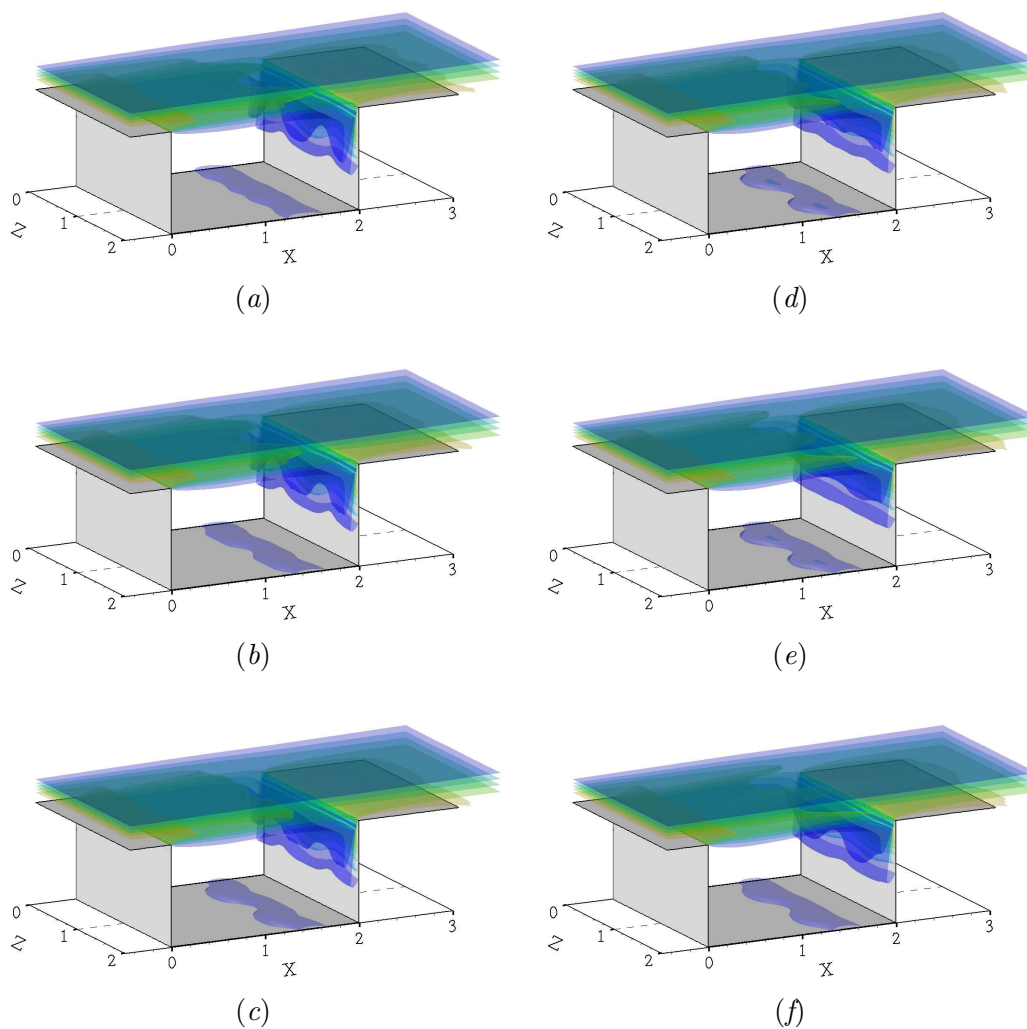


Figure 5.16: Vorticity field for 3D run 2M0325-3D. Six different times (*a-f*) are shown, corresponding to approximately one-sixth phase intervals of a half-period of the 3D instability (same times as in figure 5.3). Five equi-spaced translucent iso-surfaces of the vorticity magnitude are represented for  $||\boldsymbol{\omega}||D/U = 1$  to 5.

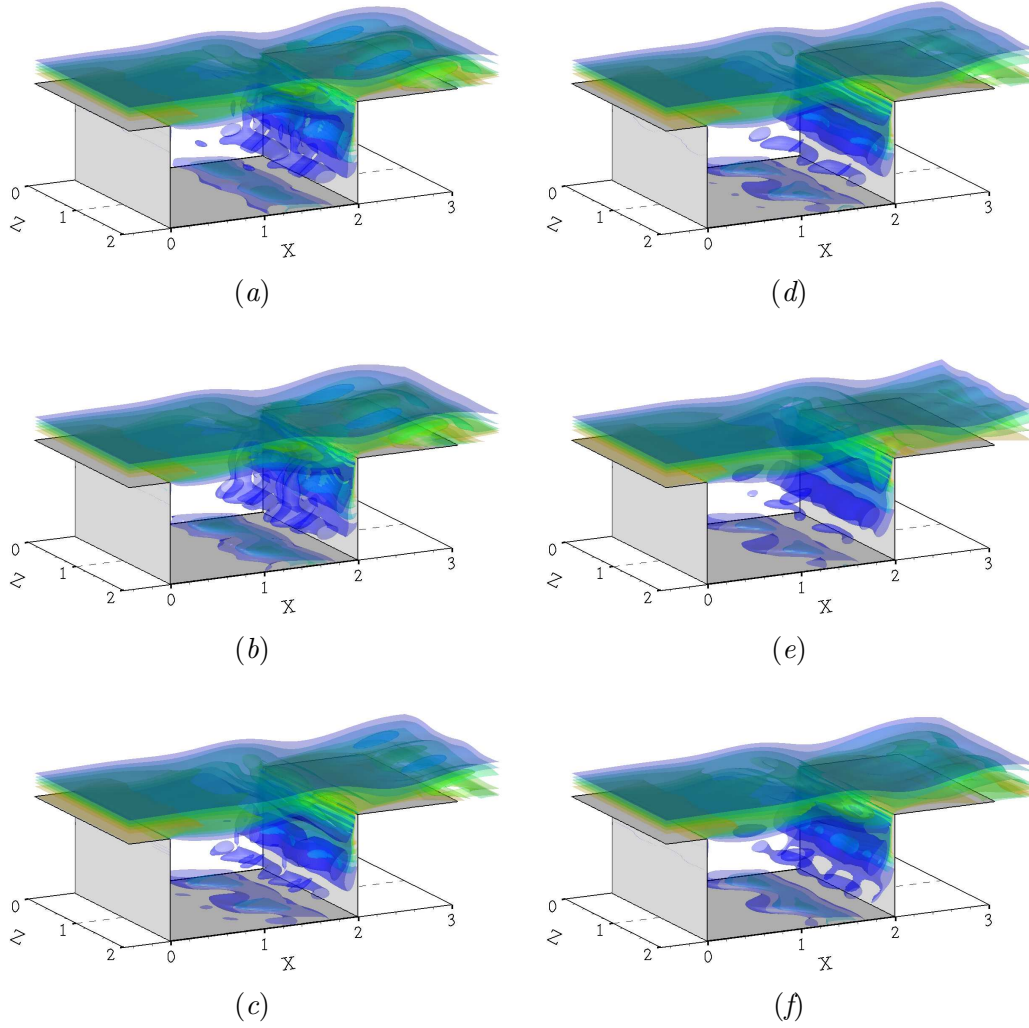


Figure 5.17: Vorticity field for 3D run 2M06-3D. Six different times (*a-f*) are shown, corresponding to approximately one-sixth phase intervals of a half-period of the 3D instability (same times as in figure 5.5). Five equi-spaced translucent iso-surfaces of the vorticity magnitude are represented for  $||\boldsymbol{\omega}||D/U = 1$  to 5.

### 5.3 Multiple three-dimensional modes

As mentioned in § 3.2.1, the linear stability the cavity of aspect ratio  $L/D = 1$  is different: that is, the critical conditions correspond to the steady mode  $i$  of smaller spanwise wavelength ( $\lambda/D \approx 0.5$ ). While the unstable oscillatory mode  $ii$  is still present at higher Reynolds numbers, it is less amplified than the steady mode for the conditions considered (see figure 3.12). From the linear analysis results, it is not possible to determine which mode (or modes) will be amplified in a real flow.

To investigate this question, we consider the run H1Re300 for a cavity of aspect ratio  $L/D = 1$  ( $M = 0.6$ ,  $Re_D = 6960$ ,  $L/\theta_0 = 23.2$ ). This case corresponds again to supercritical conditions, as the two-dimensional flow oscillates in Rossiter mode I. The 3D nonlinear simulation H1Re300-3D is then performed. According to the linear stability results in table 4.1, both mode  $i$  and  $ii$  should be unstable, as  $Re_D = 6960$  is higher than their respective critical Reynolds number.

#### 5.3.1 Oscillation frequencies

Figure 5.18 shows the time-history of the streamwise velocity  $u/U$  for runs H1Re300 and H1Re300-3D. Unlike the previous supercritical conditions in § 5.2, there is no change in the shear-layer oscillation mode: the frequency is  $St_D \approx 0.31$  in both cases, corresponding to Rossiter mode I. A low-frequency modulation is also observed and measured in the power spectrum of the 3D simulation, presented in figure 5.19. This low frequency  $St_D = 0.008$  matches the linear stability prediction for mode  $ii$  (see table 5.2).

The same features are observed in figure 5.20 for the spanwise velocity at  $0.5L$  and  $0.9L$  from the leading edge. In the power spectra in figure 5.21, peaks at the frequencies  $f_I - f_{ii}$  and  $f_I + f_{ii}$  corresponding to nonlinear interactions between the Rossiter mode I and the 3D mode  $ii$  can be identified. Here, it is interesting to note that these frequencies are less energetic than in the previous supercritical case presented in § 5.2.2 and that the peak associated with the Rossiter mode I is also present. These results are further discussed in § 5.3.3.

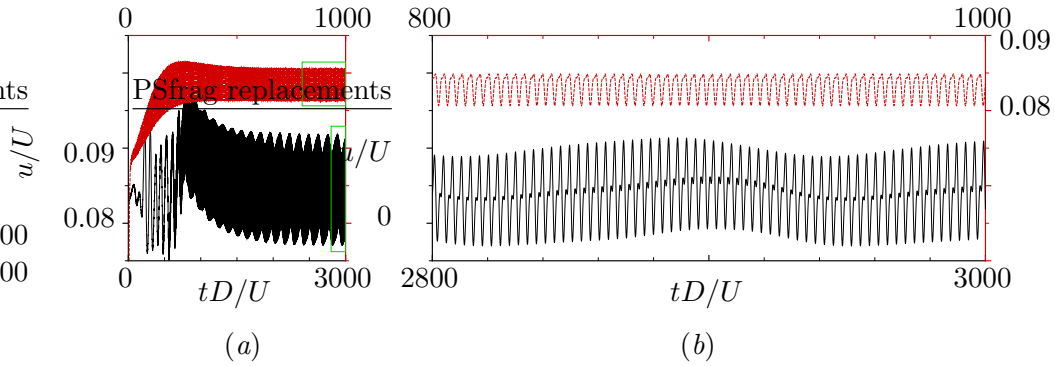


Figure 5.18: (a) Time trace of streamwise velocity at  $(x, y) = (0.5L, 0)$  for 2D run H1Re300 ( - - - ) and 3D run H1Re300-3D ( — ) at  $z = 0$ ; (b) Details of the signal in the boxes in (a). To show all the data clearly, the bottom and left axes correspond to the 3D simulation, and the top and right axes to the 2D run.

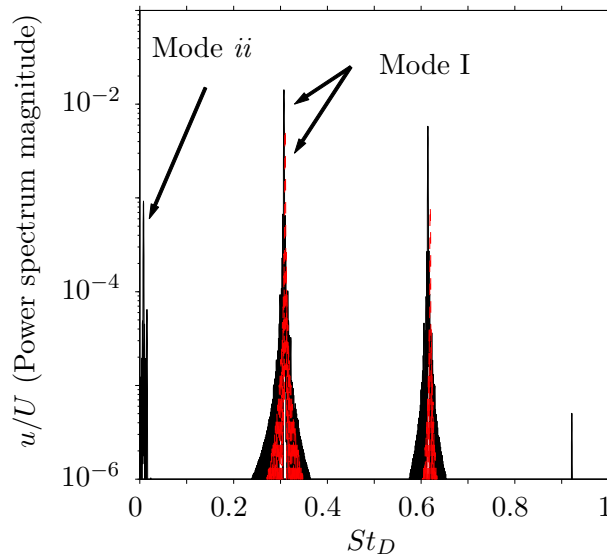


Figure 5.19: Power spectra of the streamwise velocity presented in figure 5.18; 2D run H1Re300 ( - - - ): 3D run H1RE300-3D ( — ). The different modes are identified and their harmonics can also be observed

Run	H1M03Re300			H1Re300		
	2D subcritical			2D supercritical		
$L/D$	1			1		
$Re_D$	6960			6960		
$L/\theta_0$	23.2			23.2		
$M$	0.3			0.6		
	$St_D$	Mode	$\lambda/D$	$St_D$	Mode	$\lambda/D$
Rossiter prediction	0.366	I	$\infty$	0.319	I	$\infty$
	0.854	II	$\infty$	0.745	II	$\infty$
2D DNS	0.357†	I	$\infty$	0.310	I	$\infty$
3D Linear Stability	0	$i$	0.4	n.a.		
	0.007	$ii$	1	n.a.		
	0.361†	I	$\infty$	n.a.		
3D DNS	not computed			0	$i$	0.4
				0.008	$ii$	0.4
				0.307	I	$\infty$

Table 5.2: Comparison of the dominant mode prediction for 2D and 3D runs with  $L/D = 1$ . † For subcritical conditions, the Rossiter modes are damped but the oscillation frequency can still be measured from the early times. The linear stability results are not available (n.a.) for supercritical conditions.

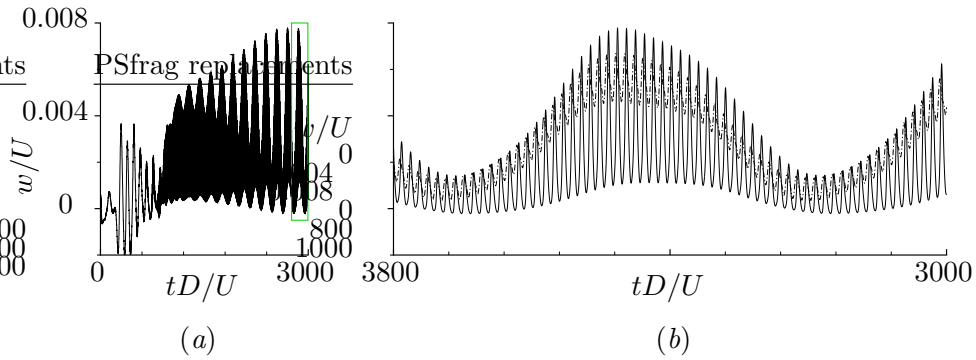


Figure 5.20: (a) Time trace of spanwise velocity at  $(x, y, z) = (0.9L, 0, 0)$  for 3D run H1Re300-3D; (b) Details of the signal ( — ) in the box in (a) and of the spanwise velocity at  $(x, y, z) = (0.5L, 0, 0)$  ( - - - )

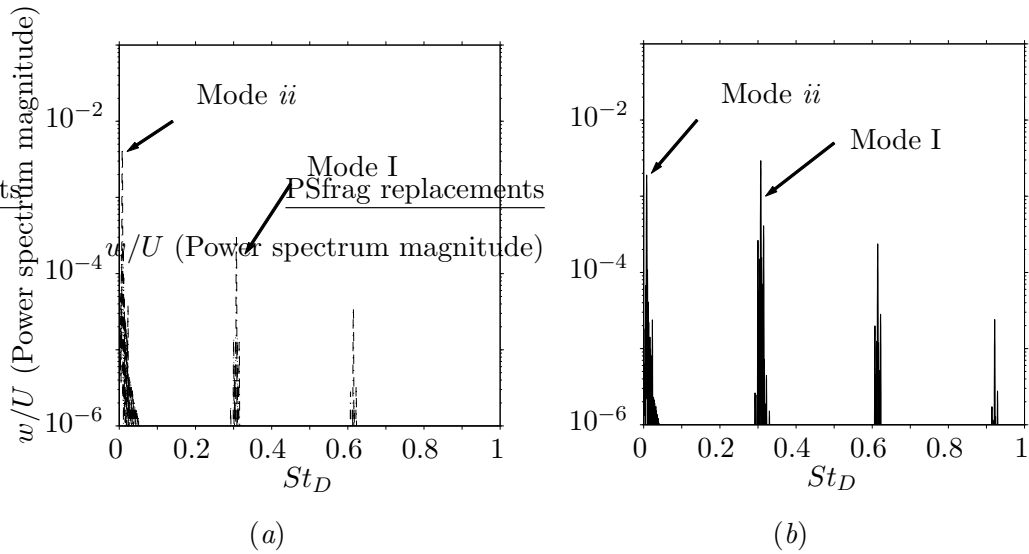


Figure 5.21: Power spectra of the spanwise velocity presented in figure 5.20 for 3D run H1Re300-3D: (a) measurements at  $(x, y, z) = (0.5L, 0, 0)$  ( - - - ); (b) measurements at  $(x, y, z) = (0.9L, 0, 0)$  ( — )

### 5.3.2 Evidence of the steady three-dimensional mode

The formation of spanwise structures is again observed inside the cavity, with spanwise wavelength  $\lambda/D = 0.4$ . Spectral analysis in the spanwise direction confirms this particular wavelength.

In figure 5.22, it is clear that two different instabilities can be identified: first, a *steady* instability leading to the formation of stationary cellular pattern near the upstream and bottom walls; and on top of it, an *unsteady* instability leading to the growth and decay of disturbances rotating inside the primary vortex. Here, because of the similarity in spanwise wavelength, we identified the steady mode with mode  $i$  from the linear analysis results. As for the unsteady mode, in addition to its matching frequency, it is also visually similar to mode  $ii$  from run 2M0325-3D in figure 5.3, but its wavelength is 0.4 rather than the anticipated  $\lambda/D = 1$ .

As our linear analysis only captures the leading eigenvalue at a given spanwise wavelength, it is possible that mode  $ii$  does have a positive linear growth rate at  $\lambda/D = 0.4$  that is not measured because the growth rate of mode  $i$  is larger. Under the present conditions, we suspect that both mode  $i$  and  $ii$  are selected.

### 5.3.3 Time-averaged flow

As a result of the presence of the steady mode, the time-averaged flow exhibits the same spanwise modulation of wavelength 0.4. This result can be clearly observed in the time-averaged velocity and vorticity fields presented in figure 5.23. The velocity magnitude inside the cavity remains small and its spanwise average is comparable to the result of the 2D simulation (less than 1% difference).

We can now interpret the peak at  $f_I$  in the spectra of the spanwise velocity in figure 5.21 as  $f_I - f_i$ , corresponding to the nonlinear interactions between the Rossiter mode I and the 3D steady mode  $i$  of frequency  $f_i = 0$ . This frequency is also more energetic than the frequencies  $f_I - f_{ii}$  and  $f_I + f_{ii}$  associated with the 3D steady mode  $i$ . This observation tends to confirm the linear stability results that mode  $i$ , rather than mode  $ii$ , is the dominant mode at these conditions.

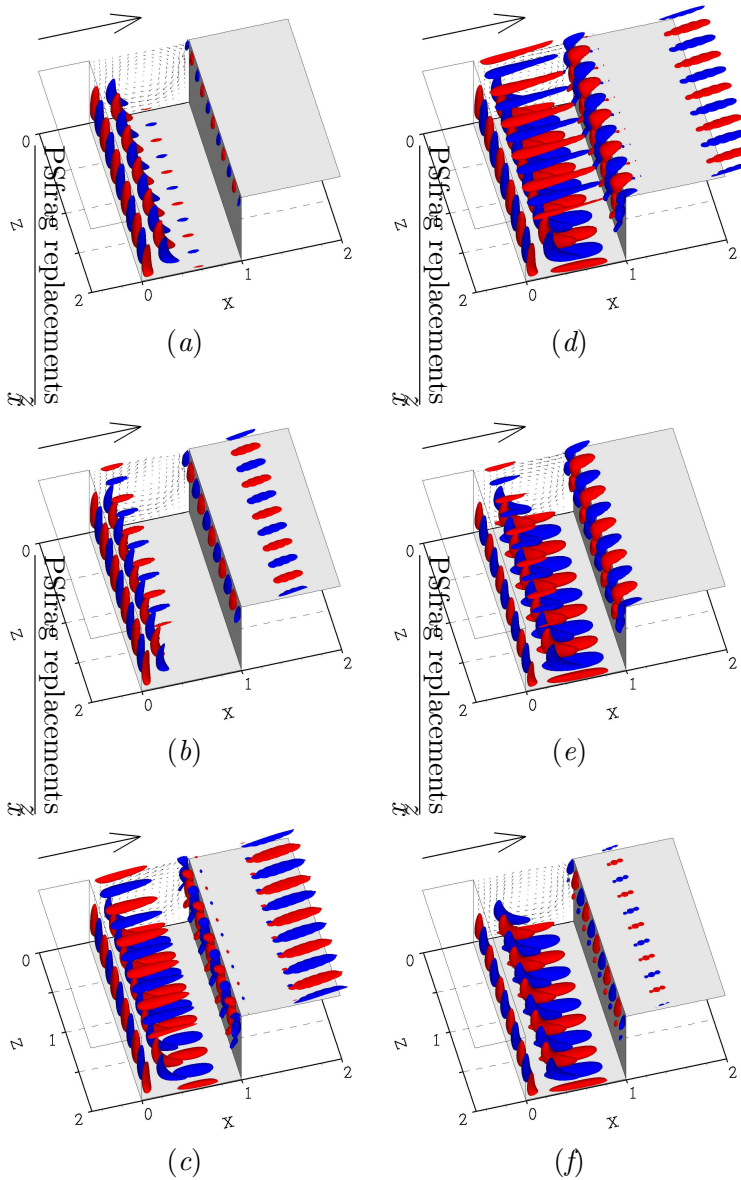


Figure 5.22: Visualisation of the spanwise structures in 3D run H1Re300-3D. Six different times (*a-f*) are shown, corresponding to approximately one-sixth phase intervals of a period of the 3D instability. The iso-surfaces represent the spanwise velocity levels  $w/U = -0.005$  and  $w/U = 0.005$ . The whole spanwise extent of the cavity is shown and the wavelength  $\lambda/D = 0.4$  of the instability is clear. The upstream parts of the cavity walls has been removed to show the data clearly. The velocity vectors in the streamwise cross-section at  $z = 0$  are shown inside the cavity and once in the freestream for comparison

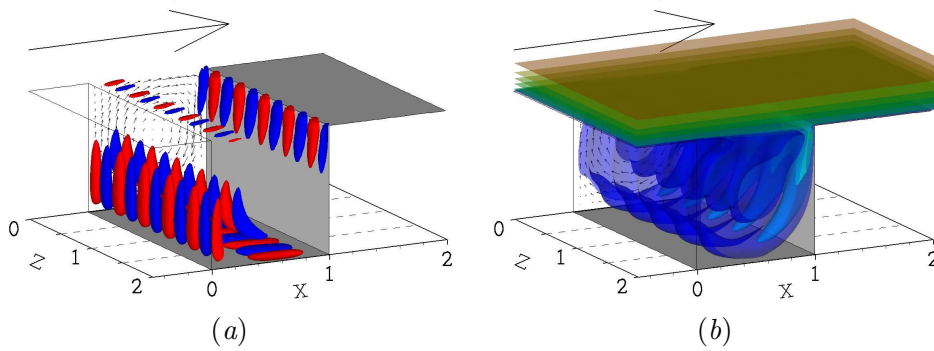


Figure 5.23: Time-averaged flow field for run H1Re300-3D:(a) Iso-surfaces of the spanwise velocity  $w/U = -0.005$  and  $w/U = 0.005$ ; (b) Four equi-spaced translucent iso-surfaces of velocity magnitude between  $\|\mathbf{u}\|/U = 0.025$  and  $0.1$  inside the cavity, and five between  $\|\mathbf{u}\|/U = 0.1$  and  $0.9$  above the cavity

Overall, the amplification caused by the steady mode is weak but we suspect that it accounts for the small increase in amplitude of shear-layer oscillations, as seen in figure 5.18.

In conclusion, for the supercritical conditions of run H1Re300-3D, the non-linear 3D simulation shows again the coexistence of shear-layer oscillations and three-dimensional instabilities. In this case, both oscillatory and non-oscillatory 3D modes are present in the flow. This steady mode is consistent with mode  $i$  identified in our linear stability analysis, and is reminiscent of instabilities reported in square lid-driven cavity flows and discussed in § 4.2.2. The unsteady 3D mode corresponds again to mode  $ii$  but its spanwise wavelength is  $\lambda/D = 0.4$ , the dominant wavelength for the steady mode, rather than 1 as previously observed. Also, the presence of the 3D steady mode causes a spanwise modulation of the time-averaged flow of the same wavelength 0.4, and an increase in oscillations amplitude. These features are not captured by the 2D simulation.

## Chapter 6

# Connection with Previous Experimental and Numerical Results

### 6.1 General remarks on cavity flow experiments

Measurements of the three-dimensional mode in cavity flow experiments face several challenges. The first difficulty arises from the influence of the side walls and end effects inherent to any experimental configuration. Ahuja & Mendoza (1995) conducted an extensive set of cavity experiments and suggested that the parameter  $L/W$ , the cavity length to width ratio, provided a transition between two- and three-dimensional flow. For  $L/W < 1$  they classified the cavity as two-dimensional, as the flow was found to be uniform over much of the span with a coherent shear layer spanning most of the cavity width, and for  $L/W > 1$  as three-dimensional. However, their classification was based on the observation of three-dimensionality in the mean flow for  $L/W > 1$ , most likely caused by end-effects and significant spillage of flow over the sides into the cavity, and therefore not related to the three-dimensional instability we identify.

Additionally, the presence of so-called “wall jet” and “sidewall-induced three-dimensional vortices” has also been reported in backward-facing step flows in both experimental (e.g., Armaly *et al.*, 1983) and numerical studies (e.g., Williams & Baker, 1997). While these flow structures are generated by the three-dimensional nature of the experimental setup and are not representative of any global instability

of the two-dimensional base flow, their effect was shown to stretch up to several step heights in the spanwise direction away from the sidewalls. In their most recent work on lid-driven cavities, Albensoeder & Kuhlmann (2006) established the extent of the sidewall effect both numerically and experimentally. For a square lid-driven cavity of spanwise aspect ratio 6.55, they showed that the presence of the sidewall suppressed the three-dimensional instability except for a symmetric region of span approximately 2 at the center of the cavity.

For wider cavities, experimental evidence of three-dimensionality have been observed by several researchers. In water channel experiments, Rockwell & Knisely (1980) identified a spanwise wavy structure emerging in the shear layer near the cavity trailing edge. A hydrogen bubble technique was used to visualise the spanwise structure in the cavity, shown in figure 6.1. Under the experiment conditions, they observed self-sustained oscillations in the streamwise direction (corresponding to Rossiter modes) as well as “severe but relatively ordered spanwise distortion,” which makes this case a typical supercritical condition as discussed in § 5.2. They associated the three-dimensional structure with the “large-scale recirculation vortex between the free shear layer and the walls of the cavity.” Precise values of the spanwise wavelengths are not reported. This experiment is discussed in more detail in appendix C.

In another water channel experiment, Ward (1973) investigated the inception of cavitation in a rectangular cavity as a function of the aspect ratio  $L/D$ . Cavitation can occur when the local pressure is less than the saturation pressure of the liquid, which leads to the formation of vapor bubbles in the flow. Under certain conditions, three-dimensional flows were observed within the cavity, as shown in figure 6.2. For a cavity of aspect ratio 1.27, a steady periodic wave form develops inside the cavity, and is sketched in figure 6.3 as type II. In this case, three and a half periods are present in the experiment, which corresponds to a spanwise wavelengths of  $\lambda/D \approx 2.9$ . This value is larger than our typical results of  $0.4 \leq \lambda/D \leq 1$ . also, the side-view of the cavitation shows “an oval shape” that does not appear to be strongly related with the recirculating vortical flow near the downstream

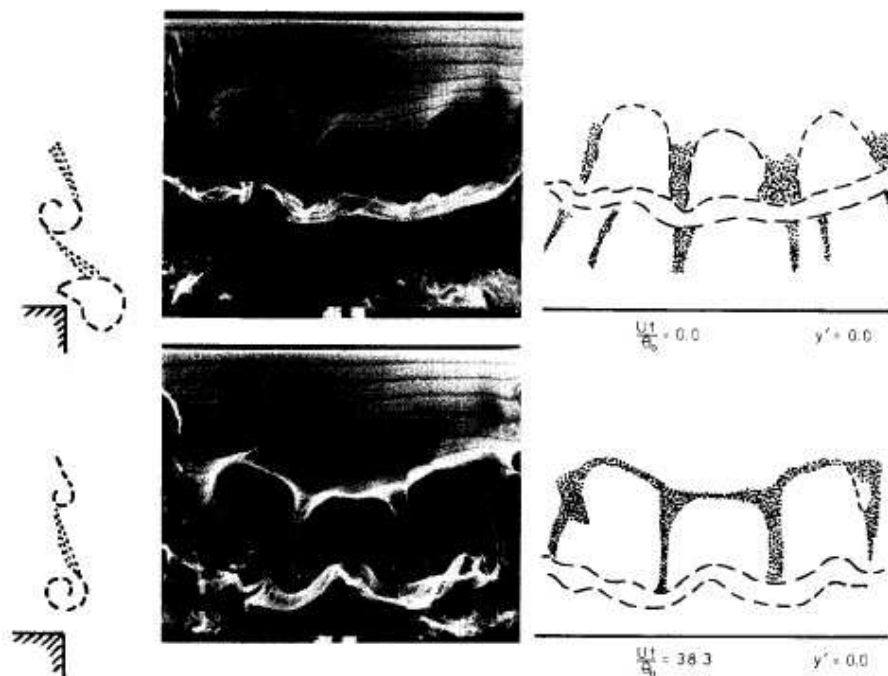


Figure 6.1: Experimental visualisation of the spanwise structures. This corresponds to figure 8 in the article by Rockwell & Knisely (1980), “Sequence showing evolution of cells in sheet of timelines caused by longitudinal vortices.” Reprinted with permission from D. Rockwell and C. Knisely, Observations of the three-dimensional nature of unstable flow past a cavity, 23(3) 425-431 1980. Copyright 1980, American Institute of Physics.

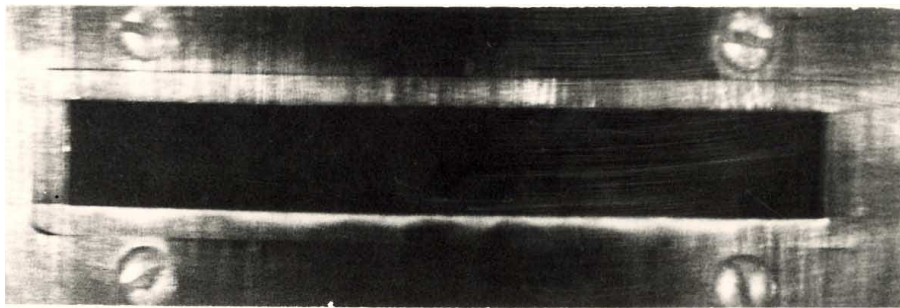
corner of the cavity. A different instability, referred as type III in figure 6.3, is observed when the aspect ratio is decreased to  $L/D \approx 1$ . In this case, the cavitation is centered inside the primary vortex. This location corresponds to the zone of minimum pressure in our simulations, where cavitation could occur. From the bottom picture in figure 6.2, we estimated the number of periods in the experiment to 12, which leads to spanwise wavelengths of  $\lambda/D \approx 0.6$ , similar to our results for the  $L/D = 1$  cavity.

Likewise, the high Reynolds number wind tunnel experiments by Maull & East (1963) show, under certain conditions, regular “cells” across the span of the internal cavity flow at low Mach numbers. They did not report any Rossiter mode oscillation, so their results could be considered representative of the subcritical conditions discussed in §5.1. For their cavity of aspect ratio  $L/D = 2$ , the cells are found to be steady in time and have a larger wavelength of about  $4D$ , compared to our oscillating structure of wavelength  $D$ . Their conclusions are drawn from oil flow visualisations of surface streamlines at the bottom of the cavity and the spanwise static pressure distribution measurements.

While there is qualitative agreement with our findings, the results from these early experiments highlight some of the additional challenges related to the measurement of the three-dimensional instability. That is, the three-dimensional mode is in general weaker than the Rossiter mode and mainly active within the cavity, while most measurements focus on the shear layer. Also, the unsteady three-dimensional mode can be difficult to capture in the mean measurements because of its oscillatory nature about the mean flow.

## 6.2 Interpretation of low-frequency modulation in experiments

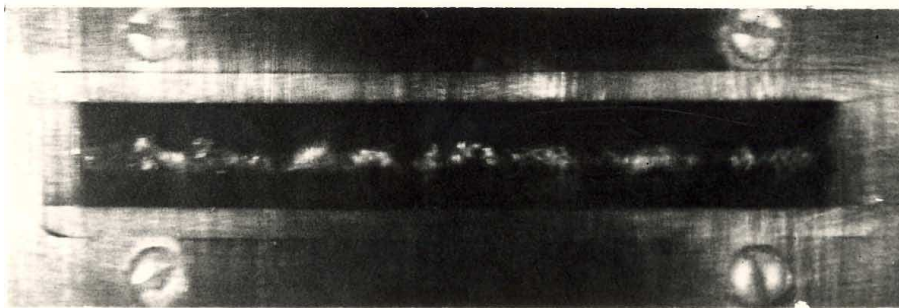
One characteristic feature of the unsteady three-dimensional mode that has actually been measured in experiment is its oscillation frequency. As previously discussed, this frequency is about an order of magnitude lower than the typical



a)  $\frac{d}{b} = 0.019$  ,  $\sigma_{IM} = .386$



b)  $\frac{d}{b} = 0.788$  ,  $\sigma_{IM} = .449$



c)  $\frac{d}{b} = 1.045$  ,  $\sigma_{IM} = .621$

Figure 6.2: Visualisation of the slot cavitation. This corresponds to figure 1 in the article by Ward (1973), "Slot cavitation." Here,  $d/b = D/L$  and  $\sigma_{IM}$  is the mean value of the incipient cavitation index.

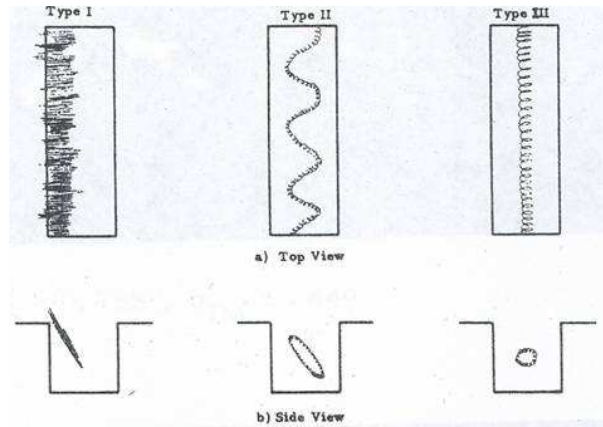


Figure 6.3: Schematic of the different flow types in the slot cavitation experiment. This corresponds to figure 4 in the article by Ward (1973), “Flow types. Flow direction right to left.”

Rossiter mode frequencies. As a result, the low-frequency components in the spectrum of oscillating flows are often not measured because of lack of resolution, and when they are, we believe these frequencies tend to be overlooked or misinterpreted as caused by the experimental setup (such as fan noise, etc.). Based on our results, we present here a different interpretation of the low-frequency modulation observed in experiments: namely, that it is caused by the centrifugal instability.

### 6.2.1 Water channel experiments

Neary & Stephanoff (1987) performed a set of water channel experiments for a three-dimensional cavity of aspect ratios  $L/D = 3.5$  and  $W/D = 21$ , with laminar incoming boundary layer ( $L/\theta_0 \approx 80$ ). These conditions are comparable to our run series TK4M03. Indeed, the visualisation (in their figure 3) of the steady base flow for subcritical conditions at Reynolds number  $Re_D = 908$  shows striking resemblances with our results in figure 4.1(c) obtained at  $Re_D = 980$  and  $L/\theta_0 = 60$ . Under certain flow regime, their experimental results showed the presence of a transverse wave on the primary vortex of the cavity prior to the development of a fully turbulent state. As the Reynolds number is increased, stronger interac-

tions between the shear layer and primary vortex are observed, with rapid growth and decay of the pressure oscillations. This feature indicates a Reynolds number dependence of the three-dimensional mode similar to our linear results.

Confirmation of the low frequency of the three-dimensional oscillation we obtain is also suggested by their observations. In their work, they identify a primary frequency  $f_1$  that corresponds to the (Rossiter) shear-layer structures and a secondary frequency  $f_2$  that they associate with the three-dimensional waviness. The frequency  $f_2$  is close to  $f_1$ , but a reexamination of time-histories of pressure actually show long-period modulation of the frequency  $f_1$ . Thus it would appear to us that the  $f_2$  frequency is really just an interaction between a low frequency  $f_{3D}$  and the primary frequency  $f_1$ . From the reported frequencies values for their so-called “regime II,” the frequency  $f_{3D} \approx f_1 - f_2$  was estimated to  $f_{3D}D/U = 0.023$ . The value obtained here at  $Re_D = 2560$  is in excellent agreement with the frequency  $St_D = 0.026$  of the three-dimensional instability identified in the linear analysis of run TK4M03Re65.

### 6.2.2 Moderate Mach number experiments

More recently, Cattafesta III *et al.* (1998) and Kegerise *et al.* (2004) investigated the presence of multiple distinct peaks in the pressure spectrum of oscillating cavity flows, in particular at low frequency. They performed an extensive set of experimental measurements for two cavity configurations:  $L/D = 2$ ,  $M = 0.4$  and  $L/D = 4$ ,  $M = 0.6$ . The other parameters were fixed at  $L/W = 3$ ,  $Re_L = 1.5 \cdot 10^6$ , and the incoming boundary layer was turbulent with  $L/\theta_0 \approx 275$  (*private communication with the authors*). For both conditions, their detailed frequency analysis of the unsteady pressure signals inside the cavity showed the presence of multiple Rossiter modes, in good agreement with expected frequencies.

More importantly, they reported that the Rossiter modes experienced low-frequency amplitude modulation. While they were able to interpret other peaks in the spectrum as quadratic nonlinear interactions between Rossiter modes, they concluded that these interactions were not the cause of the low-frequency compo-

ment, as they showed that the low-frequency mode was not significantly coupled with the Rossiter modes. Based on their conclusions and our results, we argue here that the low-frequency mode observed in their experiment corresponds to the three-dimensional centrifugal instability identified in our work. The reported frequency for the cavity  $L/D = 2$  at  $M = 0.4$  is  $f_{3D} \approx 20\text{Hz}$ , or  $f_{3D}D/U \approx 0.011$ . Keeping in mind that an increase in Reynolds number was shown to cause moderate decrease of the three-dimensional mode frequency, and that the boundary layer properties had little effect on the mode features, this result compares well with the range of frequencies  $0.015 \leq St_D \leq 0.026$  obtained for cavities with the same aspect ratio at  $M = 0.325$ .

### 6.3 Visual evidence of the three-dimensional mode

While these comparisons are encouraging, the most convincing experimental evidence of the three-dimensional centrifugal instability we identified in our simulations is the recently published work from Faure *et al.* (2007). Independently and simultaneous with our numerical studies, they performed low speed experiments for open cavities of aspect ratio  $L/D = 0.5$  to 2 at medium range Reynolds numbers, with laminar incoming boundary layers ( $D/\theta \approx 35$ , approximately constant, according to a private communication with the authors). Smoke is used for flow visualisations. The cases with cavities of aspect ratio 1 and 2 are of particular interest since their experiment conditions (apart from the Mach number) match the range of parameters in our study with (fortuitously) striking accuracy.

For  $L/D = 1$  ( $R = 1$  in their notation), they report weak shear-layer oscillations and a single vortex filling the whole cavity (figure 6.4). As the Reynolds number is increased (through an increase of the external velocity  $U_e$ ), they observe the formation of “mushroom-like counter-rotating cells” near the upstream wall and symmetrically at the downstream wall. Their visualisation of the flow (presented in figure 6.5), at a horizontal cross-section inside the cavity clearly shows a periodic spanwise pattern similar to our results. The inner spanwise flow caused by the

sidewalls is also detected, but the cavity span to depth ratio  $W/D = 6$  is large enough that the central section of the experiment exhibits periodic structures away from the sides.

They report that these structures were not stationary and could not be identified for an external velocity below a certain critical value corresponding to  $Re = 4030$ . This result matches the critical conditions  $Re = 4060$  we estimated for cavities with  $L/D = 1$  at low Mach number (see table 4.1). Additionally, for an external velocity  $U_e = 2.09$  m/s ( $Re = 6960$  matching exactly the Reynolds number used in our simulations), their measure of the distance between two pairs of structures gives a spanwise wavelength  $\lambda = 0.022$  m or  $\lambda/D = 0.44$ , again matching our conclusions from the linear analysis ( $\lambda/D = 0.4$  for run H1M03Re300) and the full three-dimensional simulation ( $\lambda/D = 0.4$  for run H1Re300-3D). The experimental flow field at these conditions is not shown, but good qualitative agreement is obtained between our 3D numerical results in figure 6.6 and their visualisations at lower Reynolds number in figure 6.5.

Similar results are reported for the  $L/D = 2$  cavity, but the structures are very unsteady in that case and the wavelength was not measured. The visualisation of a cross-section of the flow suggests a larger wavelength than for the previous case, as fewer structures are present. These observations are consistent with our findings that only an oscillatory three-dimensional mode is present for longer cavity. Coupled with larger oscillations of the shear layer, the mode is more difficult to capture accurately. In contrast, the weaker shear-layer oscillation and the presence of both steady and oscillatory modes in smaller cavities lead to a clearer visualisation of the instability.

As for the instability mechanism, Faure *et al.* (2007) did relate the three-dimensional structures to the primary vortex inside the cavity, and interpreted them in terms of Görtler vortices. Görtler problem is a classical example of centrifugal instability (e.g., Drazin & Reid, 1981), and is typically studied for the onset of instability in boundary layers along a concave wall. While the two mechanisms are related, we argue here that the origin of three-dimensional modes is the

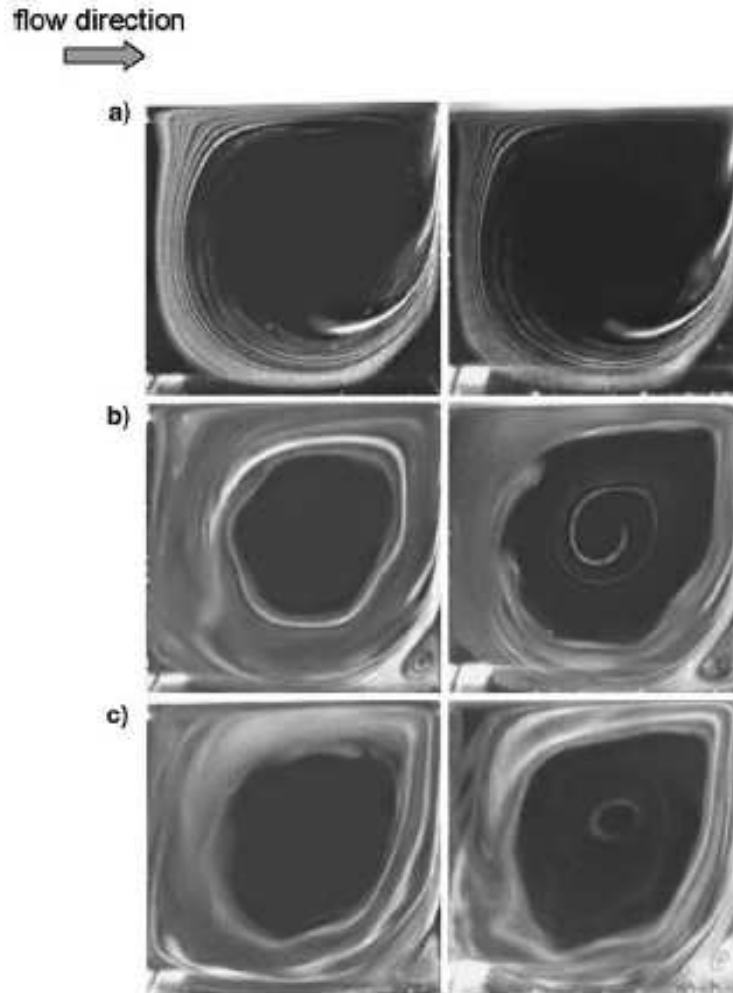


Figure 6.4: Experimental visualisation of the primary vortex for the  $L/D = 1$  cavity. This corresponds to figure 10 in the article by Faure *et al.* (2007), “Visualization in two parallel vertical planes (*left*  $z = 0$ , *right*:  $z = 30\text{mm}$ ) for the same time and  $R = 1$ . a)  $U_e = 0.69\text{ m/s}$  ( $Re = 2300$ ); a)  $U_e = 1.21\text{ m/s}$  ( $Re = 4030$ ); a)  $U_e = 1.60\text{ m/s}$  ( $Re = 5330$ ).” Reproduced with the authors’ permission.

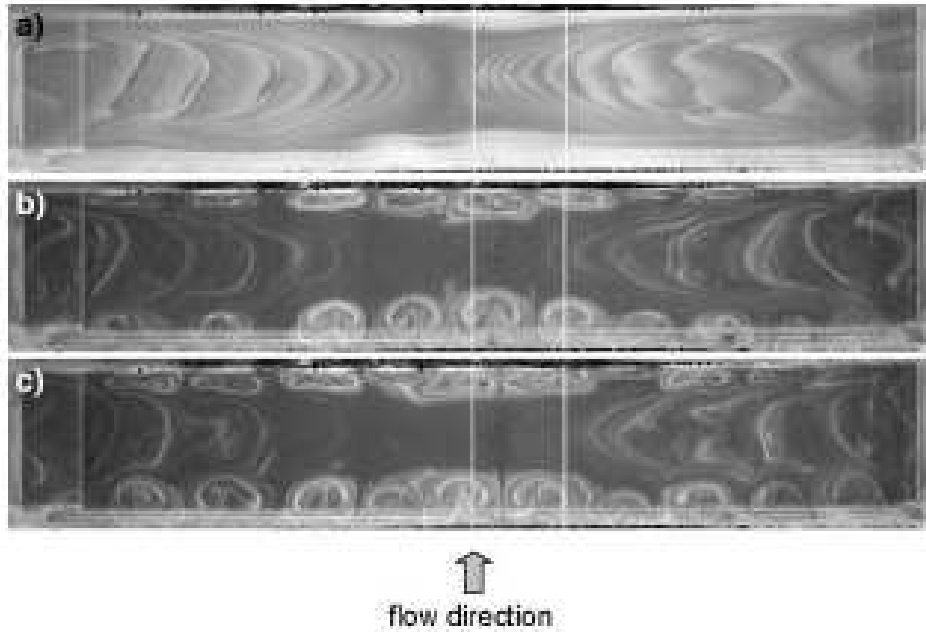


Figure 6.5: Experimental visualisation of the spanwise structures for the  $L/D = 1$  cavity. This corresponds to figure 11 in the article by Faure *et al.* (2007), “Visualization in a horizontal plane for  $R = 1$  and  $y = -15$  mm. a)  $U_e = 0.69$  m/s ( $Re = 2300$ ); a)  $U_e = 1.21$  m/s ( $Re = 4030$ ); a)  $U_e = 1.60$  m/s ( $Re = 5330$ ).” Reproduced with the authors’ permission. The white lines are the vertical visualisation planes in figure 6.4.

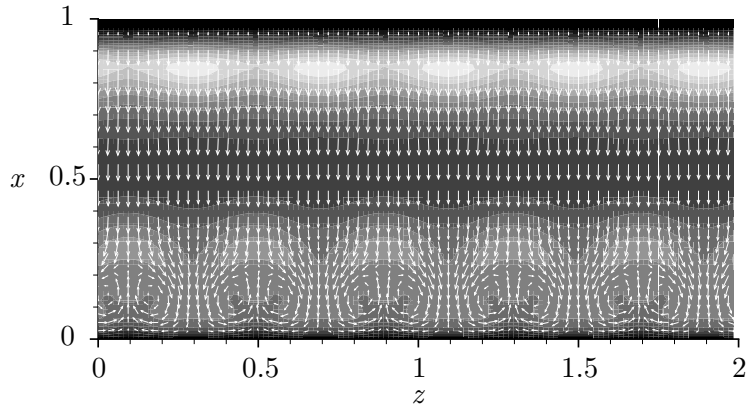


Figure 6.6: Visualisation of the spanwise structures of run H1Re300-3D in the cross section  $y/D = -0.6$  for comparison with figure 11 by Faure *et al.* (2007). The gray shadings represent equally spaced contours of the velocity magnitude between  $\|\mathbf{u}\|/U = 0.005$  and  $0.06$ . The in-plane velocity vectors are also shown.

generic centrifugal instability connected with the recirculating vortical flow inside the cavity, rather than instabilities in the boundary layers on the cavity walls.

## 6.4 Connection with previous numerical simulations

Evidence of the three-dimensional centrifugal instability is also found in recent numerical work by Podvin *et al.* (2006) and Chang *et al.* (2006) for incompressible flows over open cavities. Similar to our work, both studies focused on a cavity of aspect ratio  $L/D = 2$  with laminar incoming boundary layer and periodic conditions in the spanwise direction. In both cases, the formation of spanwise structures and the low-frequency modulation are reported.

### 6.4.1 Large eddy simulations

Chang *et al.* (2006) performed Large Eddy Simulations (LES) at  $Re_D = 3360$ , with  $L/\theta_0 = 69.5$ . Under these conditions, they reported that the shear layer oscillates with frequency  $St_D = 0.51$ , corresponding to the second mode, and that “very

low-frequency modulations are clearly observed” in time history of the velocity. From the time series in their figure 6, we estimated the modulation frequency to  $St_D = fD/U \approx 0.025 - 0.03$ . These values are similar to the results in our compressible simulations at  $M = 0.6$  with comparable conditions (i.e., run 2M06-3D at  $Re_D = 1500$ , with  $L/\theta_0 = 52.8$ ): that is, a Rossiter mode II of frequency 0.35 (compressibility effects account for the decrease in frequency) and a three-dimensional mode of frequency 0.026. They also observed a small peak associated with these low-frequency oscillations in the power spectra (in their figure 7) for approximately the same Strouhal numbers. The measurements are made for the vertical velocity in the shear layer near the downstream corner, which could account for the relatively low energy levels of the mode compared to the fundamental shear-layer mode. While they suspected these features were “a consequence of the shear layer interaction with the trailing-edge and with the recirculating motions inside the cavity,” we identify the centrifugal instability mechanism as the cause of the low-frequency modulation.

Spanwise coherent structures, referred as “spanwise vortices,” are also observed in their work, but values of the spanwise wavelength are not reported. Based on the visualisation of these structures in their figure 8(b), (c), and (d), approximately six pairs of these spanwise vortices can be accounted for along the cavity span, which is  $W/D = 6$  in their case. Therefore, the estimated spanwise wavelength of the instability is  $\lambda/D \approx 1$  and agrees with our results.

#### 6.4.2 Proper orthogonal decomposition results

Podvin *et al.* (2006) investigated a cavity of width to depth ratio  $W/D = 4$  at  $Re_D = 4000$ , with  $L/\theta_0 \approx 75$ , using proper orthogonal decomposition (POD). They related the first two most energetic POD modes to the shear-layer instabilities, and the next three modes (significantly less energetic) to “fluctuating vortex motions inside the cavity.” The visualisation of these latter modes in their figure 4 shows strong similarity with the three-dimensional eigenmode in figure 3.14. They reported that all five modes exhibit a spanwise fluctuation of wavelength

$\lambda/D \approx 1.4$ , which is comparable to our results. They suggested this particular wavelength corresponds to a secondary instability of the shear layer. Here, we again interpret the wavelength selection in terms of the centrifugal instability mechanism.

The oscillation frequency for the first two shear-layer modes was measured at 13.5 Hz, which corresponds to a second mode with  $fD/U = 0.56$ . The higher-order modes have an identical low oscillation frequency, and the precise value is not reported. From the time spectra in their figure 8, we estimated the frequency to 0.5 Hz or  $fD/U = 0.021$ , again in agreement with the three-dimensional mode frequency.

## Chapter 7

### Concluding Remarks

#### 7.1 Summary

Two- and three-dimensional global instabilities of compressible flow over open cavities were studied using Direct Numerical Simulations (DNS). We consider cavities that are homogeneous in the spanwise direction (corresponding to cavities that are wide compared to their depth or length) at subsonic Mach numbers. A DNS code was developed to solve the full compressible linear or nonlinear Navier–Stokes equations for both 2D and 3D flows.

First, the onset of self-sustained oscillations is characterized for two-dimensional cavities over a large portion of the parameter space (varying Reynolds number, Mach number, cavity aspect ratio, and incident shear-layer thickness). These instabilities, commonly referred to as shear-layer modes, correspond to the typical flow/acoustic feedback mechanism originally described by Rossiter (1964). For 2D stable flows, a linear stability analysis was conducted and identified for the first time, three-dimensional instabilities taking the form of disturbances growing in the recirculating vortical flow within the cavity. It should be noted that these instabilities would not be accessible to classical linear stability theory of parallel flows.

For cavities of aspect ratio  $L/D = 2$  and 4, the three-dimensional instability has a spanwise wavelength scaling with  $D$ , the cavity depth, and a frequency

of oscillation about an order of magnitude smaller than typical two-dimensional shear-layer (Rossiter) oscillations. We showed that the three-dimensional mode frequency is related to the time for disturbances to advect around the recirculating region.

A steady mode of smaller spanwise wavelength  $0.4D$  was also identified for a shorter cavity with  $L/D = 1$ . We argued that the specific properties of the three-dimensional mode for the square cavity are related to the primary vortex that occupies the whole cavity in that particular configuration.

The mode properties are, by and large, unaffected by Mach number over a subsonic range up to 0.6. It is not expected that they would be significantly altered by compressibility even for cavities with much larger  $M$ , since the instability is active within the cavity where the flow speed is much lower than the freestream value. In contrast, the influence of the Reynolds number is significant, as the growth rate of the three-dimensional mode increases with  $Re$ . Critical conditions for the onset of the three-dimensional instability were estimated.

Rayleigh's circulation criterion was computed for the two-dimensional steady base flow and showed that, in the inviscid limit, the flow will develop a three-dimensional centrifugal instability in the primary vortex inside the cavity. Therefore, we argued that the main mechanism behind these global three-dimensional instabilities is the generic centrifugal instability associated with the closed streamlines in the recirculating vortical flow near the downstream cavity wall. Such vortices are ubiquitous in both the low Reynolds number flows considered here and also (in a time-averaged sense) at much higher Reynolds numbers. The centrifugal instability is similar to the one previously identified in flows over a backward-facing step, lid-driven cavity, and Couette flows. Inspired by the specific features of these flows, different scalings for the properties of the centrifugal instabilities are considered. The results show reasonable agreement of the rescaled data.

Direct numerical simulations of the full Navier–Stokes equations were performed and confirmed the three-dimensional features of the flow. Oscillating (and, for the square cavity, steady) cellular patterns formed in the recirculating zone

inside the cavity. These observations were in agreement with the results of linear stability analysis, both in terms of spanwise structure and oscillation frequency. Comparison with recent experiments by Faure *et al.* (2007) at low Reynolds number also confirmed our findings.

For supercritical conditions, the (Rossiter) shear-layer oscillations exhibit a low-frequency modulation due to the presence of the three-dimensional instability. Similar modulation and low-frequency components in the spectrum of oscillating cavity flows are reported in both incompressible and compressible experiments. Evidence of that low frequency was also found in previous numerical studies. We argue that these observations are related to the centrifugal instability we identified.

## 7.2 Potential applications for flow control

As different distinctive properties of the three-dimensional centrifugal instability have been observed in both high Reynolds number flows and experiments with subsonic speed up to  $M = 0.6$ , we conclude that three-dimensional modes are likely to exist in open cavity flows for practical applications and be relevant in the area of cavity control.

Currently, there are two different approaches being advocated for control of cavity oscillations. The first (e.g., Stanek, 2005) attempts to reduce broadband noise in cavity oscillations in an open-loop way by forcing the flow near the cavity leading edge at relatively high frequency. If there are three-dimensional instabilities in the flow, then information about the wavelength and growth rates of these structures could be used (with appropriate scaling arguments) to suggest optimal spanwise variation of actuator inputs in order to excite the instabilities or suppress them.

The second area of application to cavity control is in the suppression of tones. Here the basic 2D instabilities are the target for tonal noise reduction via closed-loop control. Three-dimensional instabilities are, however, relevant, since they could represent a limiting factor in the efficacy of such control effects. In addition,

sensors are sometimes placed within cavities and thus knowledge of additional large-scale unsteadiness will help guide sensor placement and data processing.

Thus it appears that there may be an untapped potential to inherently three-dimensional effects in cavity flows. It is our hope that the results presented here will help future work on control to exploit these effects.

## Appendix A

### Simulation Parameters

The flow parameters and stability results of the different 2D and 3D linear simulations are presented in tables A.1, A.2, A.3, A.4 and A.5.

For supercritical conditions (i.e., shear-layer mode), the oscillation frequency  $St_L = fL/U$  of the dominant mode is reported. Recall that the linear stability results are not available for such conditions.

For the three-dimensional centrifugal instability, the spanwise wavelength  $\lambda/D$  and the oscillation frequency  $St_D = \omega D/2\pi U$  of the mode with the largest linear growth rate are reported.

Run	Parameter					Stability				
	nonlinear		linear			nonlinear		linear		
	2D	$St_L$	3D	$\lambda/D$	$St_D$	2D	$St_L$	3D	$\lambda/D$	$St_D$
	$L/D$	$M$	$L/\theta_0$	$Re_\theta$	$Re_D$					
H1M03Re150	1	0.3	23.2	150	3480	NO		NO		
H1M03Re300	1	0.3	23.2	300	6960	NO		CI	0.4	0
H1M04Re300	1	0.4	23.2	300	6960	NO		–		
H1M04Re450	1	0.4	23.2	450	10440	NO		–		
H1M05Re300	1	0.5	23.2	300	6960	NO		–		
H1M05Re450	1	0.5	23.2	450	10440	SL	0.330			
H1	1	0.6	23.2	86.3	2000	NO		NO		
H1Re110	1	0.6	23.2	110	2550	NO		NO		
H1Re140	1	0.6	23.2	140	3250	NO		NO		
H1Re200	1	0.6	23.2	200	4640	NO		CI	0.5	0
H1Re300	1	0.6	23.2	300	6960	SL	0.310			

Table A.1: Parameters and stability for the run series H1. Abbreviations for stability are: NO = No Oscillations, SL = Shear-Layer mode, CI = three-dimensional Centrifugal Instability, – = not computed.

Run	Parameter					Stability				
	nonlinear		linear							
	2D	$St_L$	3D	$\lambda/D$	$St_D$					
	$L/D$	$M$	$L/\theta_0$	$Re_\theta$	$Re_D$					
2M01	2	0.1	52.8	56.8	1500	NO		CI	1	0.025
2M01Re80	2	0.1	52.8	80	2110	NO		CI	1	0.023
2M03Re35	2	0.3	52.8	35	925	NO		NO		
2M03	2	0.3	52.8	56.8	1500	NO		CI	1	0.025
2M03Re65	2	0.3	52.8	65	1715	NO		CI	1	0.025
2M03Re80	2	0.3	52.8	80	2110	SL	0.799			
2M0325	2	0.325	52.8	56.8	1500	NO		CI	1	0.025
2M033Re60	2	0.33	52.8	60	1585	NO		–		
2M035	2	0.35	52.8	56.8	1500	NO		CI	1	0.026
2M035Re60	2	0.35	52.8	60	1585	SL	0.475			
2M0365	2	0.365	52.8	56.8	1500	SL	0.470			
2M038Re50	2	0.38	52.8	50	1320	NO		CI	1	0.025
2M04Re50	2	0.4	52.8	50	1320	SL	0.457			
2M04	2	0.4	52.8	56.8	1500	SL	0.462			
2M045Re50	2	0.45	52.8	50	1320	SL	0.438			
2M05Re35	2	0.5	52.8	35	925	SL	0.426			
2M06	2	0.6	52.8	56.8	1500	SL	0.407			
2M06-K†	2	0.6	80	37.5	1500	SL	0.723			

Table A.2: Parameters and stability for the run series 2M. Abbreviations for stability are: NO = No Oscillations, SL = Shear-Layer mode, CI = three-dimensional Centrifugal Instability, – = not computed †These particular flow parameters match the conditions of the experiment by Krishnamurty (1956), apart from the Reynolds number. The simulation is performed for validation purposes.

Run	Parameter					Stability					
	nonlinear		linear								
	2D	$St_L$	3D	$\lambda/D$	$St_D$						
	$L/D$	$M$	$L/\theta_0$	$Re_\theta$	$Re_D$						
TK2M0325	2	0.325	30.1	56.8	855	NO		NO			
TK2M0325Re80	2	0.325	30.1	80	1205	NO		NO			
TK2M0325Re100	2	0.325	30.1	100	1505	NO		NO			
TK2M0325Re140	2	0.325	30.1	140	2110	NO		CI	1	0.015	
TK2M0325Re200	2	0.325	30.1	200	3010	NO		–			
TK2M0325Re400	2	0.325	30.1	400	6025	NO		–			
TK2M04Re300	2	0.4	30.1	300	4520	NO		–			
TK2M04Re400	2	0.4	30.1	400	6025	SL	0.402				
TK2M05Re200	2	0.5	30.1	200	3010	NO		–			
TK2M05Re300	2	0.5	30.1	300	4520	SL	0.383				
TK2M05Re400	2	0.5	30.1	400	6025	SL	0.379				
TK2M06	2	0.6	30.1	56.8	855	NO		NO			
TK2M06Re80	2	0.6	30.1	80	1205	NO		NO			
TK2M06Re140	2	0.6	30.1	140	2110	NO		CI	1	0.016	
TK2M06Re200	2	0.6	30.1	200	3010	NO		–			
TK2M06Re300	2	0.6	30.1	300	4520	SL	0.362				
TK2M06Re400	2	0.6	30.1	400	6025	SL	0.366				

Table A.3: Parameters and stability for the run series TK2. Abbreviations for stability are: NO = No Oscillations, SL = Shear-Layer mode, CI = three-dimensional Centrifugal Instability, – = not computed.

Run	Parameter					Stability				
						nonlinear		linear		
	$L/D$	$M$	$L/\theta_0$	$Re_\theta$	$Re_D$	2D	$St_L$	3D	$\lambda/D$	$St_D$
TK4M03	4	0.3	60.2	50	755	NO		NO		
TK4M03Re65	4	0.3	60.2	65	980	NO		CI	1.25	0.026
TK4M03Re80	4	0.3	60.2	80	1205	SL	0.814			
TK4M04Re40	4	0.4	60.2	40	600	NO		–		
TK4M04	4	0.4	60.2	50	755	SL	0.784			
TK4M04Re65	4	0.4	60.2	65	980	SL	0.780			
TK4M05Re30	4	0.5	60.2	30	450	NO		–		
TK4M05	4	0.5	60.2	50	755	SL	0.743			
TK4M06Re30	4	0.6	60.2	30	450	NO		NO		
TK4M06Re40	4	0.6	60.2	40	600	SL	0.712			
TK4M06	4	0.6	60.2	50	755	SL	0.708			

Table A.4: Parameters and stability for the run series TK4. Abbreviations for stability are: NO = No Oscillations, SL = Shear-Layer mode, CI = three-dimensional Centrifugal Instability, – = not computed.

Run	Parameter					Stability				
						nonlinear		linear		
	$L/D$	$M$	$L/\theta_0$	$Re_\theta$	$Re_D$	2D	$St_L$	3D	$\lambda/D$	$St_D$
4M03Re200	4	0.3	30.1	200	1505	NO		NO		
4M03Re400	4	0.3	30.1	400	3010	NO		CI	1.25	0.011

Table A.5: Parameters and stability for the run series 4M. Abbreviations for stability are: NO = No Oscillations, SL = Shear-Layer mode, CI = three-dimensional Centrifugal Instability, – = not computed.

## Appendix B

### Linear Stability Experiments

To fully ascertain the effect of Mach number and Reynolds number on the three-dimensional instability, we perform a set of numerical experiments to assess the differing influence of the basic (steady) two-dimensional flow and the Reynolds and Mach numbers. To do this, we focus on cavities of aspect ratio  $L/D = 2$  and construct different cases as follows:

1. Using the methods outlined in chapter 2, we vary the Reynolds and Mach numbers in both computing the steady base flow (from 2D DNS) and in solving for the three-dimensional disturbances. This is the default procedure for the linear stability analysis.
2. We *artificially* increase the Reynolds and/or Mach number acting on the disturbances only, while holding the steady base flow constant. While these simulations are non-physical, they are useful in assessing the flow physics. For the cases where we change the disturbance Reynolds number, the base flow is held strictly constant. For the cases where we change the Mach number, we also *rescale* the basic cavity flow by assuming that the base flow is essentially incompressible, and rescaling the flow velocity to the higher Mach number.

## B.1 Influence of the Mach number

As the Mach number is varied over the range  $0.1 < M < 0.6$  for subcritical conditions, we observe only minor changes in the 2D (steady) base flow, and the linear stability results for the three-dimensional flow are similar. To verify that the mode properties are in fact independent of the Mach number, we performed 3D linear simulations with a fixed base flow  $\bar{\mathbf{q}} = \bar{\mathbf{q}}_{2M01}$  obtained for run 2M01 at  $M = 0.1$ . Under the conditions of run 2M01, the flow is 3D unstable, with growth rate and frequency reported in table B.1. Before a perturbation at a Mach number  $M'$  different than  $M = 0.1$  can be added to the base flow  $\bar{\mathbf{q}}_{2M01}$ , it must be appropriately rescaled to  $\bar{\mathbf{q}}'_{2M01}$  as follow:

$$\bar{u}' = \bar{u} \frac{M'}{M} \quad \bar{v}' = \bar{v} \frac{M'}{M} \quad \bar{\rho}' = (\bar{\rho} - 1) \frac{M'}{M} + 1 \quad \bar{P}' = (\bar{P} - \frac{1}{\gamma}) \frac{M'}{M} + \frac{1}{\gamma}.$$

The three-dimensional stability analysis is then conducted for 3D disturbances at Mach number  $M' = 0.3$  and  $M' = 0.6$ , with the corresponding modified base flow  $\bar{\mathbf{q}}'_{2M01}$ . These simulations are denoted 2M01toM03 and 2M01toM06 and all the parameters used are summarized in table B.1. The comparison with run 2M01 shows that the Mach number has no influence on the three-dimensional instability: the flow remained 3D unstable with the results of the rescaled simulations matching the initial run in term of growth rate and frequency.

A similar parametric study was conducted for 3D stable flow conditions. The 2D basic (steady) flow  $\bar{\mathbf{q}}_{2M03Re35}$  of run 2M03Re35 ( $M = 0.3$ ) was modified to get  $\bar{\mathbf{q}}'_{2M03Re35}$ . Perturbations at  $M' = 0.6$  and  $M' = 0.8$  were then added, for a cavity of spanwise wavelength  $\lambda/D = 1$ . Again the rescaled simulations 2M03Re35toM06 and 2M03Re35toM08 exhibit the same features as the original run even at these high Mach numbers and remain stable with similar damping rate and frequency as run 2M03Re35. Note that, under all the conditions considered here, the flows at Mach number  $M' = 0.6$  and  $M' = 0.8$  would already be two-dimensional unstable.

run	2D parameters				2D base	3D parameter	Eigenvalue	
	$L/D$	$M$	$L/\theta_0$	$Re_\theta$	flow	modified	$\sigma_D$	$St$
2M01	2	0.1	52.8	56.8	$\bar{\mathbf{q}}_{2M01}$		0.0083	0.0255
2M01toM03	-		-	-	$\bar{\mathbf{q}}'_{2M01}$	0.3	0.0085	0.0254
2M01toM06	-		-	-	$\bar{\mathbf{q}}'_{2M01}$	0.6	0.0084	0.0254
2M03Re35	2	0.3	52.8	35	$\bar{\mathbf{q}}_{2M03Re35}$		-0.0151	0.0280
2M03Re35toM06	-		-	-	$\bar{\mathbf{q}}'_{2M03Re35}$	0.6	-0.0152	0.0280
2M03Re35toM08	-		-	-	$\bar{\mathbf{q}}'_{2M03Re35}$	0.8	-0.0155	0.0280

Table B.1: Results of the parametric study of the Mach number influence on the linear stability of 3D perturbations of spanwise wavelength  $\lambda/D = 1$ . Here the superscript “ ’ ” indicates that the 2D base flow has been rescaled to the modified Mach number  $M'$

## B.2 Influence of the Reynolds number

Unlike the Mach number, the Reynolds number does affect the basic (steady) 2D flow and the properties of the three-dimensional mode, in terms of both growth/damping rate and oscillation frequency. To separate the Reynolds number effect from the influence of the basic flow, a similar analysis is performed. In this parametric study, a perturbation at a different Reynolds number (denoted by the superscript “ ’ ”) is added to the two-dimensional base flow  $\bar{\mathbf{q}}_{2M03}$  obtained for run 2M03 ( $L/D = 2$ ,  $M = 0.3$ ,  $L/\theta_0 = 52.8$ ,  $Re_\theta = 56.8$ ). Three different Reynolds numbers ( $Re'_\theta = 65$ ,  $Re'_\theta = 50$  and  $Re'_\theta = 35$ ) are considered and the spanwise wavelength of these perturbations is  $\lambda/D = 1$ . Rescaling is not needed in this case, and the resulting simulations are denoted 2M03toRe65, 2M03toRe50, and 2M03toRe35.

The growth/damping rates and frequency of the corresponding three-dimensional instabilities are reported in table B.2. Here, the flow is artificially stabilized/amplified by reducing/increasing the Reynolds number. For these test cases, it is interesting

run	2D parameters				2D base	3D parameter	Eigenvalue	
	$L/D$	$M$	$L/\theta_0$	$Re_\theta$	flow	modified	$\sigma_D$	$St$
2M03Re35	2	0.3	52.8	35	$\bar{\mathbf{q}}_{2M03Re35}$		-0.0151	0.0280
2M03	2	0.3	52.8	56.8	$\bar{\mathbf{q}}_{2M03}$		0.0079	0.0249
2M03Re65	2	0.3	52.8	65	$\bar{\mathbf{q}}_{2M03Re65}$		0.0124	0.0247
2M03toRe35	-	-	-		$\bar{\mathbf{q}}_{2M03}$	35	-0.0244	0.0252
2M03toRe50	-	-	-		$\bar{\mathbf{q}}_{2M03}$	50	0.0007	0.0250
2M03toRe65	-	-	-		$\bar{\mathbf{q}}_{2M03}$	65	0.0148	0.0248

Table B.2: Results of the parametric study of the Reynolds number influence on the linear stability of 3D perturbations of spanwise wavelength  $\lambda/D = 1$

to note that, while the Reynolds number significantly affects the stability of the dominant mode by changing the growth rate, the frequencies remained identical and similar to the original case 2M03. This feature has to be contrasted with the observations from figures 3.10 3.11, and 3.12 that the frequency decreases with Reynolds number, when full 3D linear stability analysis simulation are conducted with the appropriate corresponding 2D base flow  $\bar{\mathbf{q}}$ . However, there is no contradiction there. This indicates that the mode frequency is strongly connected to the 2D steady base flow  $\bar{\mathbf{q}}$  and is only indirectly affected by the Reynolds number through the dependence of  $\bar{\mathbf{q}}$  on  $Re$ .

To clarify this point, the results from the run 2M03Re35 are compared to the experimental run 2M03toRe35 in table B.2. Again, It is important to point out here that the only difference between these two runs is the use of a different 2D base flow ( $\bar{\mathbf{q}}_{2M03Re35}$  versus  $\bar{\mathbf{q}}_{2M03}$ ) for the 3D linear stability analysis. Both simulations lead to the same stability result: the flow is 3D stable. The differences in damping rate and frequency are then caused by the difference in 2D base flow. Similar observations can be made with runs 2M03Re65 and 2M03toRe65 in table B.2.

The following conclusions can then be drawn from these numerical experiments: Firstly, the growth/damping rate of the dominant mode is directly driven by the

Reynolds number and is, to some lesser extent, dependent on the base flow. Secondly, the Reynolds number influences the mode frequency only through its effect on the two-dimensional base flow  $\bar{\mathbf{q}}$ . Finally, within the domain of 2D stability, the three-dimensional mode is essentially independent of the Mach number.

## Appendix C

### Extension of the Linear Stability to Supercritical Conditions

As previously mentioned, one limitation of the three-dimensional linear stability analysis described in chapter 2 is that it relies on the existence of a 2D steady base flow  $\bar{\mathbf{q}}(x, y)$ . In most experimental conditions and practical application, such time-independent flow does not exist, as self-sustained oscillations develop and eventually saturate. However, the recirculating vortical flow in the downstream part of the cavity is still present for these supercritical conditions, in a time-averaged sense. In an attempt to extend the present methods to such supercritical flows, we examine the linear stability of  $\bar{\mathbf{q}}$  defined as the time-averaged two-dimensional base flow.

#### C.1 Two-dimensional simulation of Rockwell experiment

We consider the water channel experiments by Rockwell & Knisely (1980) for a three-dimensional cavity of aspect ratio  $L/D = 1.08$  and  $W/D = 3.76$ . This particular case is chosen here for two reasons. Firstly, it corresponds to supercritical conditions where three-dimensional structures have been reported, as discussed in § 6.1. Secondly, the experimental conditions are within the parameter range of our direct numerical simulations, in terms of Reynolds number.

A low Mach number ( $M = 0.3$ ) two-dimensional simulation is performed, with the other flow parameters matching the experimental conditions ( $L/D = 1$ ,  $Re_\theta = 106$  and  $L/\theta_0 = 142$ ). In this case, the Reynolds number based on the cavity depth is  $Re_D \approx 15000$  and a fine mesh is required to resolve all of the flow structure. The grid is increased from 96 to 576 points along the cavity length and depth, for a total of about 1.1 million grid points.

The resulting two-dimensional flow is presented in figure C.1. As expected at this relatively high Reynolds number, a wide range of small-scale structures are present in the flow. Unlike the supercritical conditions at  $Re_D = 1500$  presented in figure 3.1, the shear-layers breaks down at approximately  $x = 0.25L$  and periodic shedding of vortical disturbances can be observed. The time trace of the pressure, streamwise and normal velocity at  $(x, y) = (0.5L, 0)$  are shown in figure C.2(a), (b) and (c) respectively. After some transient, the self-sustained oscillations in the flow saturate into a periodic regime with dominant frequency  $St = 1.526$ . This frequency corresponds approximately to the Rossiter mode III ( $St = 1.341$  in equation 1.1 with  $n = 3$ ). In general, the visualisation of the vorticity contours confirms the presence of three vortices along the cavity length simultaneously. Precise values of the oscillation frequencies in the experiment are not reported, but the numerical results are consistent with the side-view illustration in figure C.5.

From figure C.1, it is clear that a recirculating vortical flow similar to the one observed in subcritical conditions is present in the cavity. The time-averaged velocity field for run **Rkw** is shown in figure C.3. Much like the square cavities considered in chapters 3 and 4, the primary vortex occupies the whole cavity in the present case and has properties similar to a solid-body rotation away from the walls.

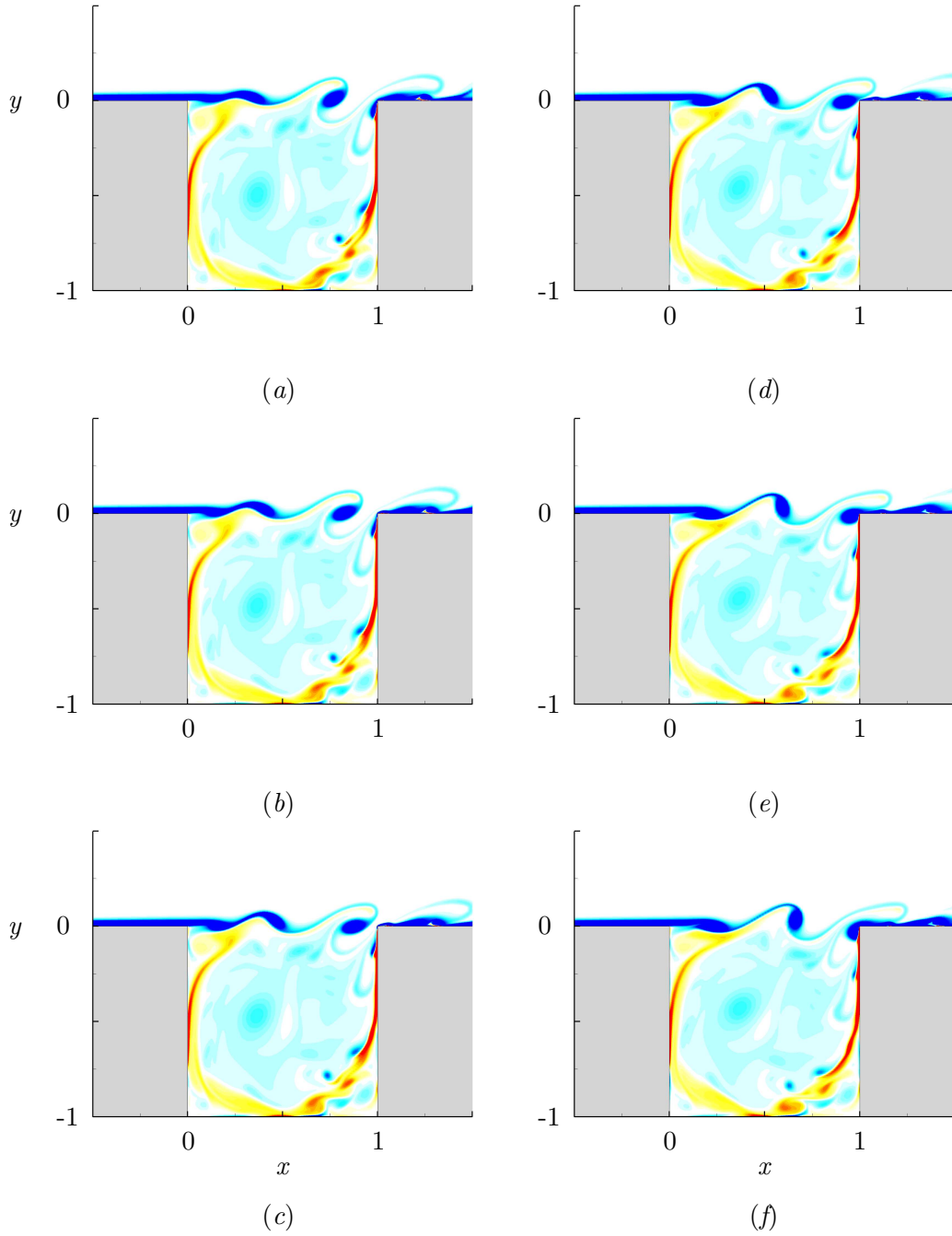


Figure C.1: Vorticity field for the run Rkw at six different times (*a-f*) corresponding to approximately a one sixth of a period of oscillation; 30 equi-spaced contours of the vorticity magnitude between  $\omega_z D/U = -15$  and 15 are shown.

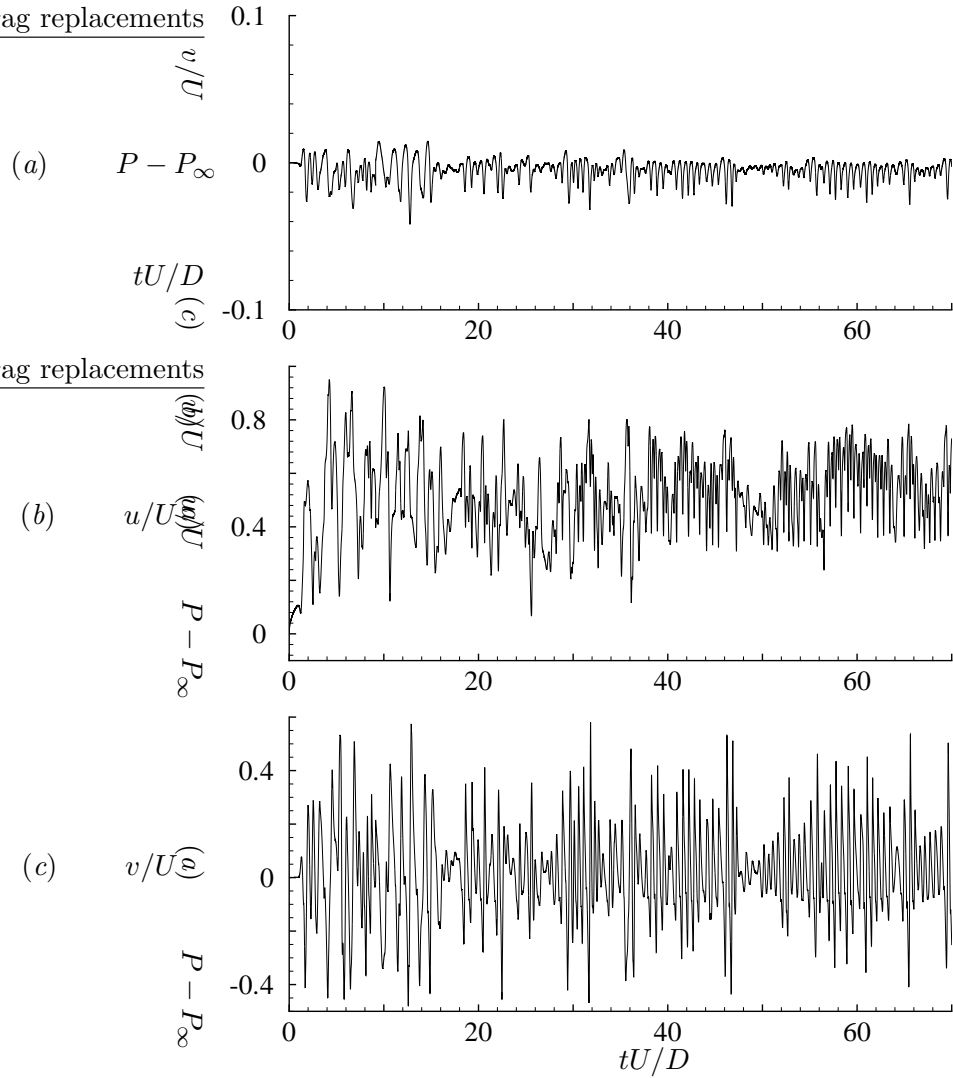


Figure C.2: Time trace at  $(x, y) = (0.5L, 0)$  for run Rkw: (a) pressure; (b) stream-wise velocity; (c) normal velocity

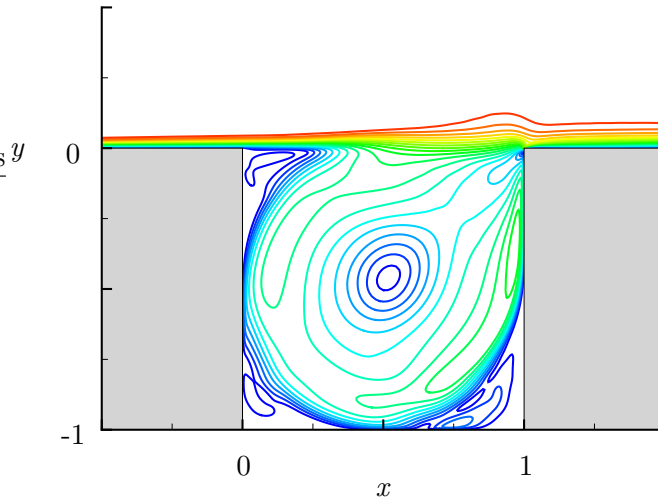


Figure C.3: Time-averaged velocity field for run **Rkw**. Nineteen equi-spaced contours of the velocity magnitude between  $\|\mathbf{u}\|/U = 0.05$  and  $0.95$  are represented.

## C.2 Linear stability results

Figure C.4 shows the streamlines and Rayleigh discriminant of the two-dimensional time-averaged base flow for run **Rkw**. The region of potential centrifugal instability covers all the outward streamlines of the primary vortex inside the cavity and is comparable to the results for the subcritical run **H1Re200** in figure 4.1,

The linear stability of this time-averaged base flow is then investigated. In this case, perturbations of spanwise wavelength ranging from  $\lambda/D = 0.05$  to  $16$  are considered. We find that all the disturbances have a positive linear growth rate and are therefore unstable. However, the perturbation with  $\lambda/D = 0.125$  has a growth rate larger than for the other wavelength and is designated as the most unstable mode. Unlike the steady mode  $i$  of wavelength  $0.4$  previously identified as the dominant mode for square cavities, this mode is oscillatory with frequency  $St = 0.046$ . These properties are significantly different from characteristics of the centrifugal modes discussed in chapter 3.

In their water channel experiments, Rockwell & Knisely (1980) identified a spanwise wavy structure and estimated the spanwise wavelengths  $\lambda_z$  to “approx-

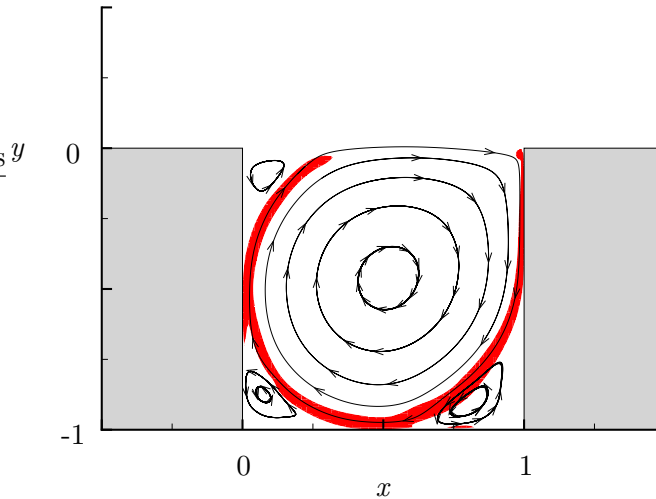


Figure C.4: Streamlines and Rayleigh discriminant of 2D time-averaged base flow for run Rkw. The red flooded region indicates where  $\eta$  is greater than 5% of its maximum value.

mately 1 to 0.5 streamwise wavelength” depending on the location in the cavity. Precise values of the wavelengths or the frequencies are not reported. Since the 2D simulation shows that the flow oscillates in Rossiter mode III, the streamwise wavelength is approximately  $D/3$ , leading to a spanwise wavelength of  $\lambda_z = 0.333D$  to  $0.167D$  for the three-dimensional instabilities. Therefore, there is some qualitative agreement between the experimental data and our linear results. The three-dimensional nonlinear simulation was not performed because the flow parameters considered here, while matching the experimental conditions, are beyond the limit of current computer resources for DNS.

We also consider the linear stability of the two-dimensional time-averaged base flow for the supercritical runs 2M06 and H1Re300, as both linear and nonlinear data is available for direct comparison in these cases. The results match for run H1Re300, but are significantly different for run 2M06, in terms of both spanwise wavelength of instability and oscillation frequency.

Overall, our attempt to extend the linear stability analysis to supercritical flows

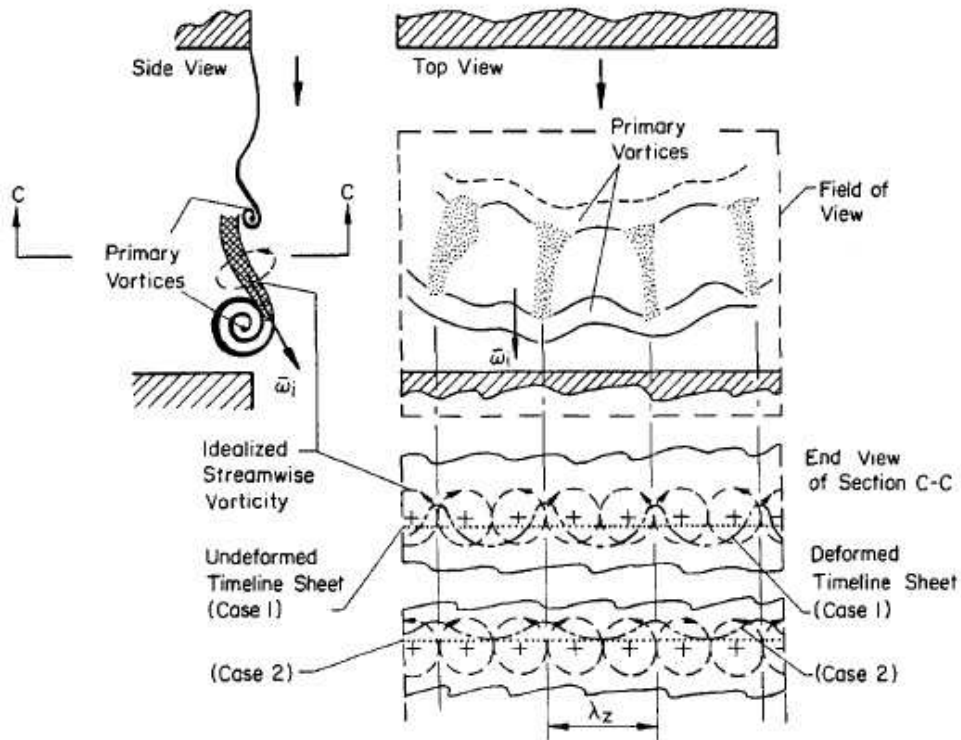


Figure C.5: Schematics of the shear-layer oscillations and spanwise structures. This corresponds to figure 3 in the article by Rockwell & Knisely (1980), “Illustration of mechanism of interaction between primary and secondary (longitudinal) vorticity.” Here, the term “primary vortices” corresponds to vortical disturbances in the shear layer, and not the recirculating vortical flow inside the cavity. Reprinted with permission from D. Rockwell and C. Knisely, Observations of the three-dimensional nature of unstable flow past a cavity, 23(3) 425-431 1980. Copyright 1980, American Institute of Physics.

lead to mixed results. Some cases showed good agreement while others did not predict the correct instability. Here, the Navier–Stokes equations are linearised with respect to the two-dimensional time-averaged base flow  $\bar{\mathbf{q}}$  that is not an exact solution of the equations. We suspect that this approximation may not be appropriate to identify the 3D instabilities accurately. As discussed in chapter 5, the linear stability results from corresponding subcritical cases (if such stable conditions exist) seem more reliable for delivering the properties of the 3D modes for supercritical conditions.

## Appendix D

### Preliminary Results on 3D Wake Mode

As mentioned in the introduction, another mode of cavity flow oscillation, commonly referred to as “*wake mode*,” has been observed in a few experiments (e.g., Gharib & Roshko, 1987) and several two-dimensional numerical simulations (e.g., Fuglsang & Cain, 1992; Cain *et al.*, 2000; Rowley *et al.*, 2002*b*; Larsson *et al.*, 2004). Since experimental evidence of the wake mode is limited for the classical 3D rectangular cavity typically used to model practical applications, this mode is not the main focus of the present work. However, it is of interest here because three-dimensionality has been shown to play a role in suppressing it. For instance, Shieh & Morris (2000) and Suponitsky *et al.* (2005) showed that two-dimensional cavity flows oscillating in wake mode return to shear-layer mode when random three-dimensional inflow disturbances are introduced. We present here some preliminary results from ongoing work on the connections between the 3D centrifugal instabilities and the presence/suppression of the wake mode.

#### D.1 Two-dimensional wake mode

The wake mode is characterized by the periodic shedding of a large vortex (about the size of the cavity) from the cavity leading edge, resulting in a significant increase in drag. Detailed description of the wake mode properties can be found in the article by Rowley *et al.* (2002*b*).

As they predict the flow transition to wake mode for longer cavities and larger

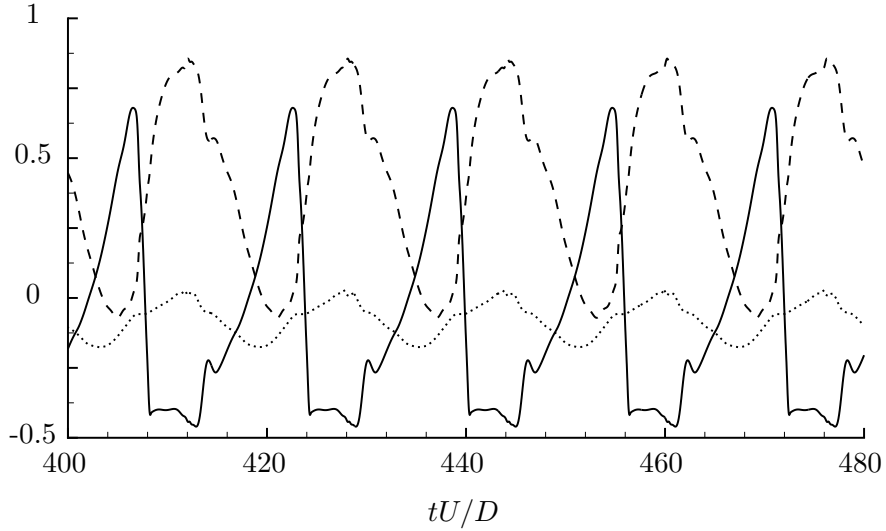


Figure D.1: Time trace at  $(x, y) = (0.5L, 0)$  for run **4M06wake**: ( ---- ) streamwise velocity  $u/U$ , ( ——— ) normal velocity  $v/U$ , ( ..... ) pressure  $P - P_\infty$

Mach and Reynolds number, we consider run **2M06** and increase the aspect ratio to  $L/D = 4$  while keeping the other parameters constant. As expected, the resulting simulation **4M06wake** ( $L/D = 4$ ,  $M = 0.6$ ,  $L/\theta_0 = 105.6$ ,  $Re_D = 1500$ ) shows that the 2D flow oscillates in wake mode. The time-trace of the pressure, the streamwise and normal velocities are presented in figure D.1, and are significantly different from the typical shear-layer mode results. The amplitude of oscillation is larger and the frequency is lower. The power spectrum in figure D.2 shows that the oscillation frequency is  $St_D = 0.063$ . This value is identical to those obtained by Rowley *et al.* (2002b) for  $L/D = 4$  cavities with Mach number within the range  $0.4 < M < 0.8$ . In particular,  $St_D = 0.064$  for their run *L4* with similar flow conditions. The power spectrum levels are about two orders of magnitude higher in this case, compare to the shear-layer mode. Overall, the large-scale shedding in the wake mode is a more violent event than the shear-layer oscillations.

The increase in drag is also observed. The instantaneous drag coefficient  $C_d$  (figure D.3) is computed by integrating the skin friction drag over the bottom of the cavity, and the pressure drag over the vertical walls at the leading and trailing edges of the cavity. The usual nondimensionalisation by  $1/2\rho U^2 A$  is used, where

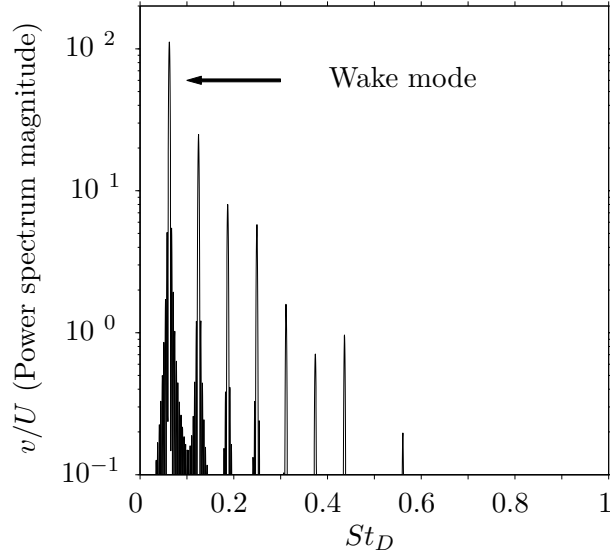


Figure D.2: Spectrum of the normal velocity for run 4M06wake. The wake mode frequency is identified and the harmonics can also be observed

$A$  is the area of integration. As anticipated, the main contribution comes from the pressure drag, resulting in an estimated average drag coefficient of  $\overline{C_d} \approx 0.3$ . This result is similar to the value  $\overline{C_d} = 0.227$  reported by Rowley *et al.* (2002b) for run  $L4$ . This value is about 15 times higher than the average drag computed for a cavity of same aspect ratio 4 with the flow oscillating in shear-layer mode.

The time-averaged flow (figure D.4) for the wake mode in run 4M06wake contrasts with the typical 2D base flow discussed throughout the present work. On average, there is no recirculating vortical flow in the downstream part of the cavity. The same conclusion actually holds for the instantaneous flow field. The mean flow above the cavity is significantly deflected upward and the maximum velocity magnitude inside the cavity reaches approximately 40% of the freestream value.

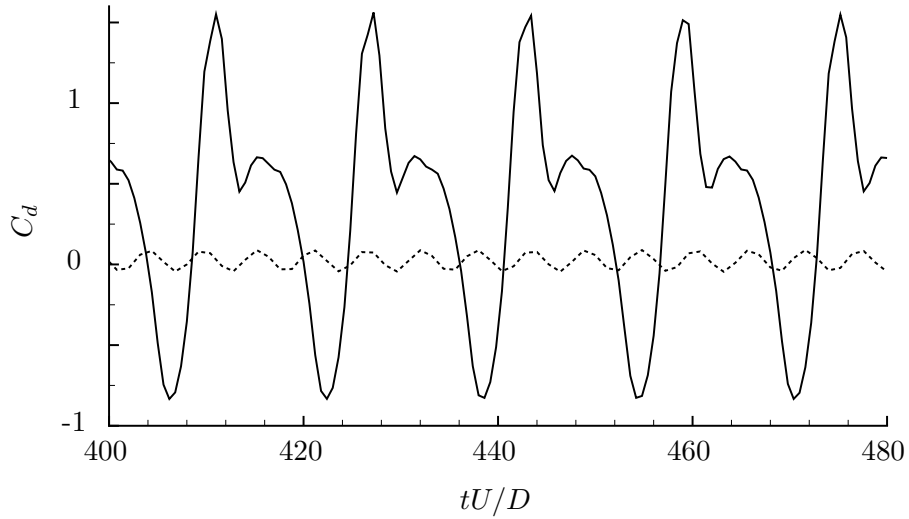


Figure D.3: Time trace of the drag coefficient: ( — ) 2D run `4M06wake` in wake mode, ( ---- ) 2D run `TK4M06Re40` in shear-layer mode

## D.2 Three-dimensional simulations

The same procedure described in chapter 5 is followed here to performed the full three-dimensional nonlinear simulations. The initial condition is the time-averaged flow field extracted from run `4M06wake` by averaging the periodic data. Two homogeneous 3D cavity of spanwise extent  $\Lambda/D = 2$  and  $\Lambda/D = 1.25$  are considered. In the first configuration, the mesh contains about 11 million grid points, with ( $N_x = 240$ ,  $N_y = 60$ ,  $N_z = 128$ ) points across the cavity in the streamwise, depth, and spanwise directions, respectively. The number of points in the span is reduce by half in the second configuration.

### D.2.1 Flow field without spanwise disturbances

First, a three-dimensional simulation is performed on the small grid without any spanwise disturbances (run `4M06wake-3D`). As expected, the 3D flow remains uniform in the spanwise direction and oscillates in wake mode. The mode frequency and properties are identical to the results of the 2D simulation. The visualisation of the flow field is presented in figure D.5.

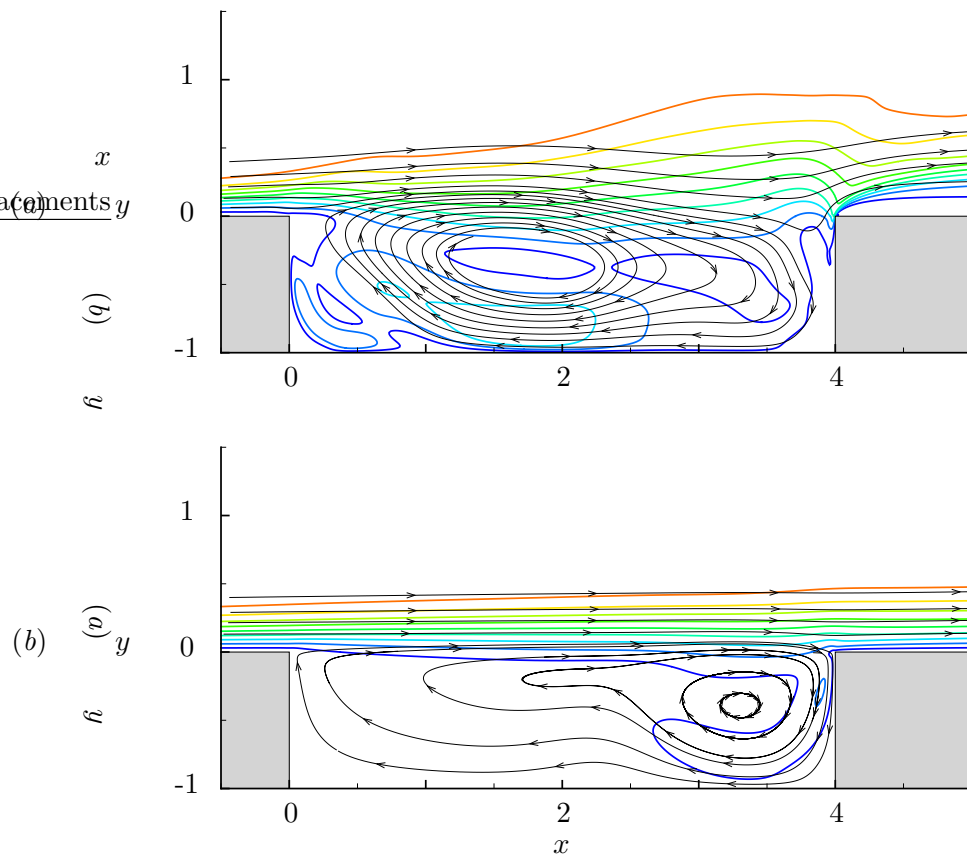


Figure D.4: Time-averaged velocity field and streamlines for  $L/D = 4$  cavities: (a) 2D run 4M06wake in wake mode, (b) 2D run TK4M06Re40 in shear-layer mode. Nine equi-spaced contours of the velocity magnitude between  $\|\mathbf{u}\|/U = 0.1$  and 0.9 are represented.

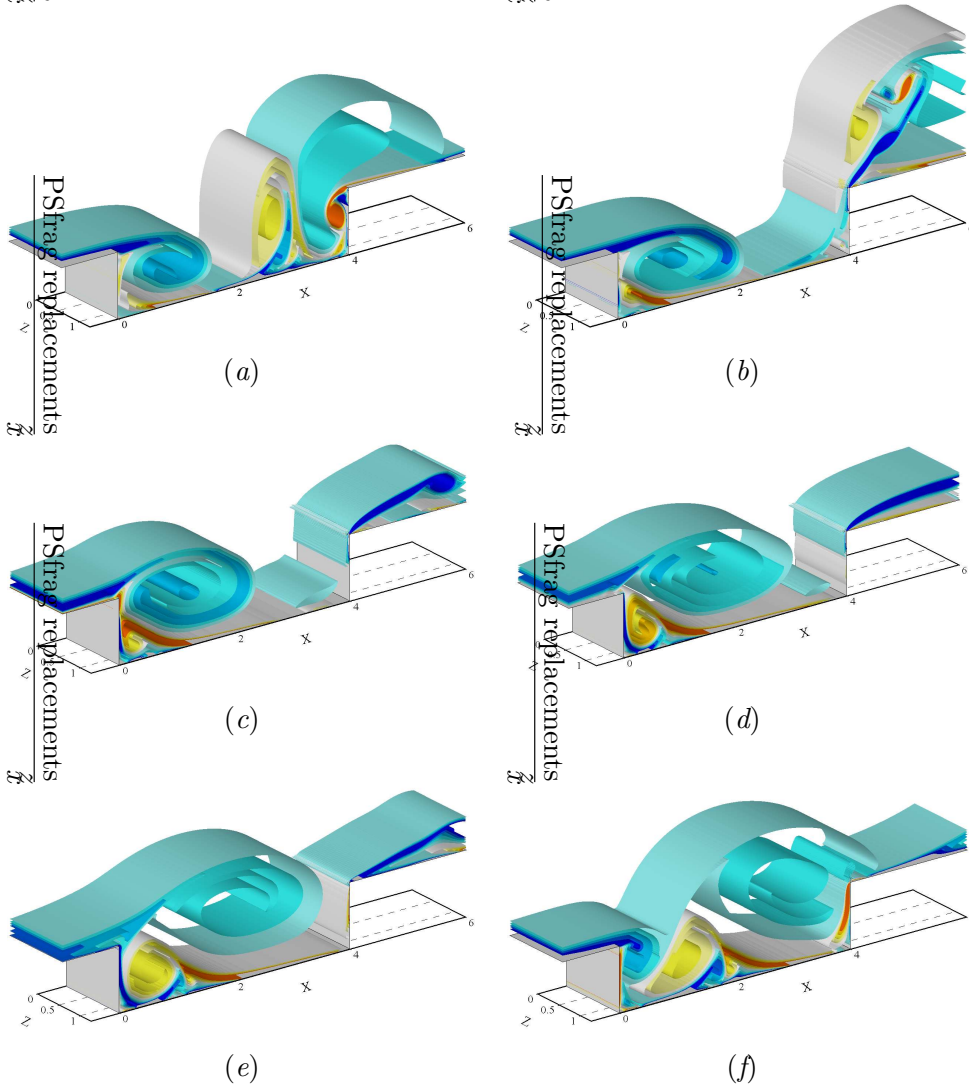


Figure D.5: Visualisation of the wake mode in 3D run 4M06wake-3D. Six different times (*a-f*) are shown, corresponding to approximately one-sixth phase intervals of a period of the instability. The iso-surfaces represent ten equi-spaced levels of the spanwise component of vorticity between  $\omega_z D/U = -5$  and 5. The whole spanwise extent of the cavity is shown and the flow is clearly uniform in the spanwise direction.

## D.2.2 Flow field with spanwise disturbances

Small perturbations of spanwise wavelength  $\lambda/D = 1.25$  are added to the time-averaged flow field from run 4M06wake. This particular wavelength is chosen because it corresponds to the most unstable mode for  $L/D = 4$  cavities, according to the linear stability analysis presented in chapter 3. The 3D simulation, referred to as 4M06-3D, is performed on both large and small grids, and lead to similar results.

With the initial spanwise disturbances, the flow does not oscillate in wake mode but instead transitions to the classical Rossiter mode. Figure D.6 shows the evolution of the vorticity field for run 4M06-3D. The shear-layer oscillations and the formation of the recirculating vortical flow near the downstream wall of the cavity can be observed.

The time trace of the velocities and pressure are presented in figure D.7: the smaller oscillation amplitude and higher frequency contrast with the wake mode results in figure D.1. The corresponding power spectra (in figure D.9(a)) show that the dominant frequency is  $St_D = 0.186$ . This value matches the prediction from Rossiter's formula for mode II ( $St_D = 0.186$  with  $n=2$  in equation 1.1). It is also consistent with the observation that, in general, two vortices are present simultaneously in the shear layer along the cavity (see figure D.6).

Unlike the previous cases in chapter 5, a dominant spanwise wavelength for the 3D instability cannot be clearly identified: a wide range of small-scale structures are present in the flow in figure D.6. Likewise, a low-frequency modulation of the shear-layer oscillation is not evident. However, the time trace in figure D.8 and the power spectrum in D.9(b) do suggest the presence of 3D mode of frequency  $St_D \approx 0.01$ . This value is similar to the prediction  $St_D \approx 0.011$  from the linear stability analysis for the run series 4M03 (see appendix A). Here, we suspect that the 3D simulation needs to be continued, as the flow has not reached a periodic limit cycle yet.

Different initial conditions may need to be considered as well. In retrospect, the choice of the time-averaged flow field of the wake mode as initial condition can be reexamined. Because the time-averaged field is significantly different from

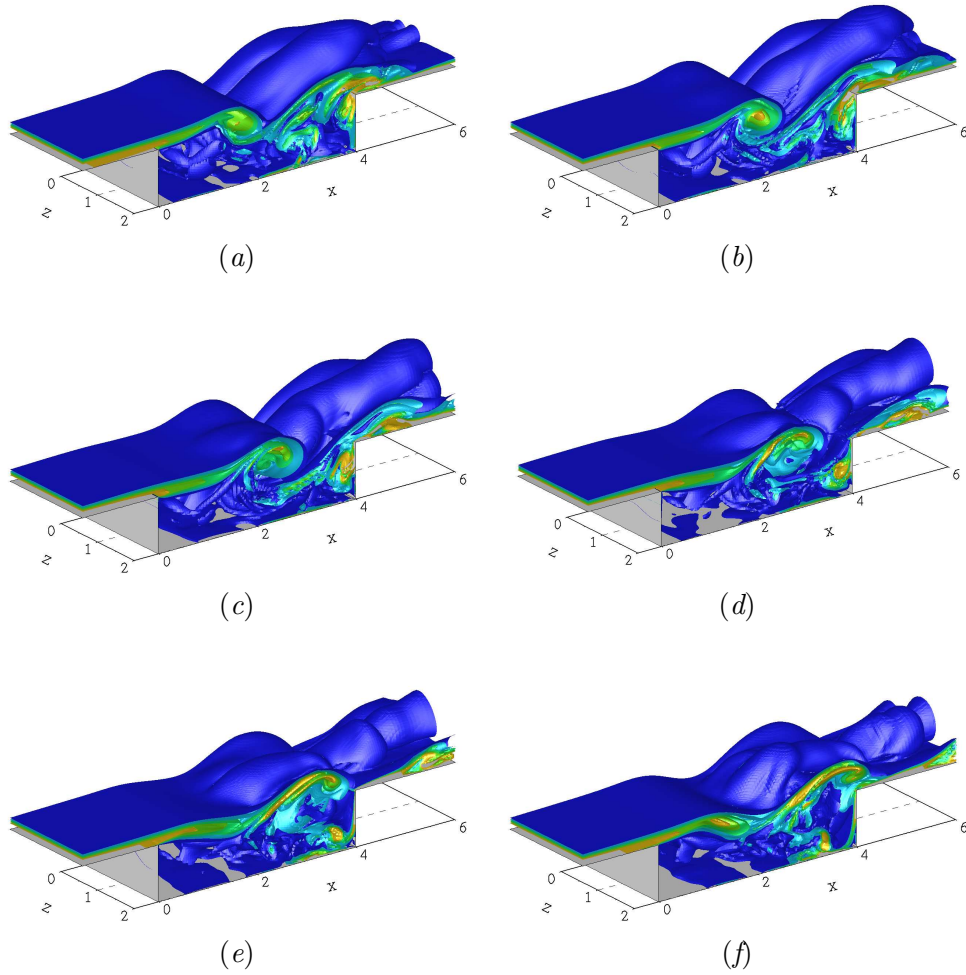


Figure D.6: Visualisation of the 3D run 4M06-3D. Six different times (*a-f*) are shown, corresponding to approximately one-sixth phase intervals of a period of the instability. The iso-surfaces represent five equi-spaced levels of the vorticity magnitude between  $\|\omega\|D/U = 1$  and 5.

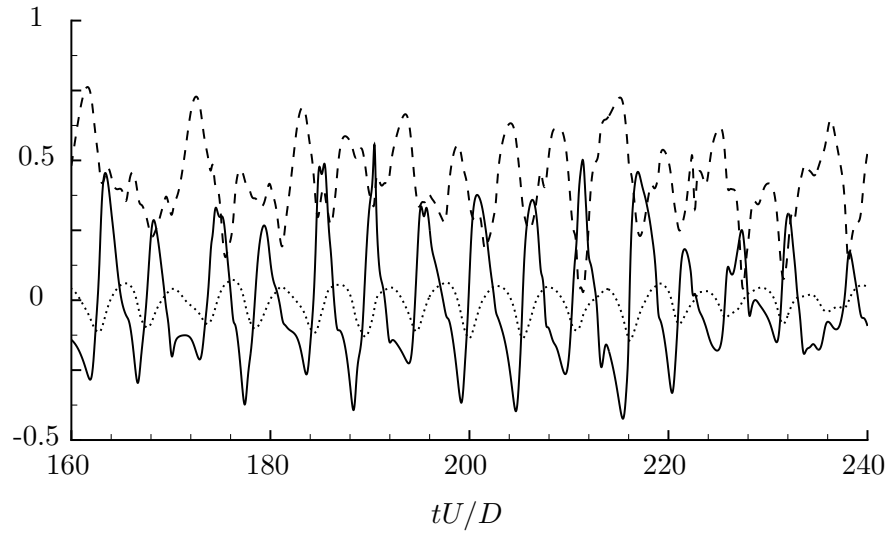


Figure D.7: Time trace at  $(x, y, z) = (0.5L, 0, 0)$  for run 4M06-3D; ( ---- ) stream-wise velocity  $u/U$ ; ( — ) normal velocity  $v/U$ ; ( ..... ) pressure  $P - P_\infty$

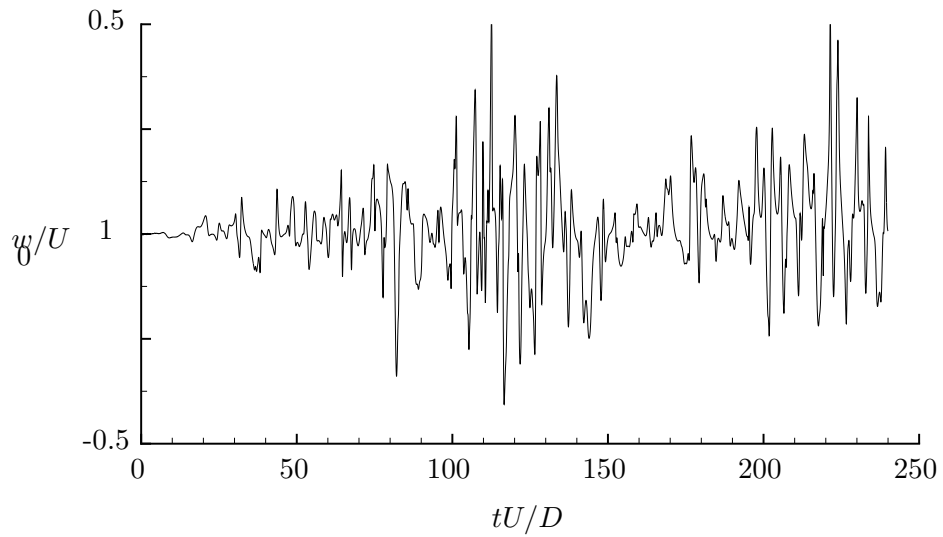


Figure D.8: Time trace of the spanwise velocity at  $(x, y) = (0.5L, 0, 1.5D)$  for run 4M06-3D

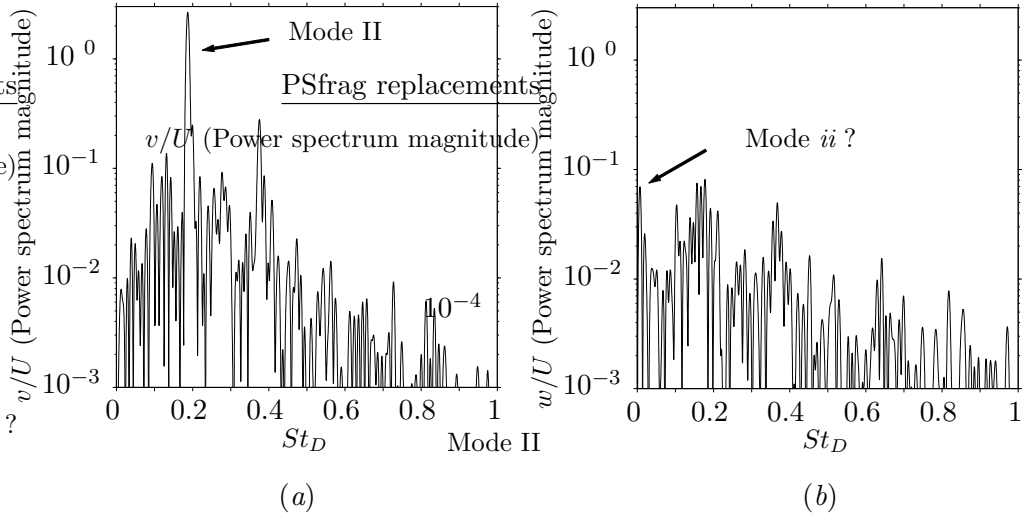


Figure D.9: Spectra at  $(x, y, z) = (0.5L, 0, 0)$  for run 4M06-3D: (a) normal velocity  $v/U$ , (b) spanwise velocity  $w/U$ . The Rossiter wake mode frequency is identified and the possible peak of the 3D mode is suggested.

any instantaneous solution of the flow equations, it introduces additional disturbances that can possibly increase the duration of a transient flow and delay the development of the different modes. Future works include 3D simulations with perturbations added to the flow field in wake mode from run 4M06wake-3D. Simulations with an incoming boundary layer nonuniform in the spanwise direction (and zero flow inside the cavity) will also be performed.

Overall, the results are consistent with the conclusions of previous numerical studies that 3D disturbances seem to suppress the wake mode for rectangular homogeneous cavities. The resulting flow oscillates in the typical shear-layer mode but is highly three-dimensional. At this stage, it is not possible to conclude whether the 3D centrifugal instability is present or not, and if it causes the transition from wake to shear-layer mode. Additional three-dimensional simulations are underway to give more conclusive answers to these questions.

## Bibliography

- AHUJA, K. K. & MENDOZA, J. 1995 Effects of cavity dimensions, boundary layer and temperature on cavity noise with emphasis on benchmark data to validate computational aeroacoustic codes. *Tech. Rep.* CR-4653. NASA.
- AIDUN, C. K., TRIANTAFILLOPOULOS, N. G. & BENSON, J. D. 1991 Global stability of a lid-driven cavity with throughflow: Flow visualization studies. *Phys. Fluids A* **3**, 2081–2091.
- ALBENSOEDER, S. & KUHLMANN, H. C. 2006 Nonlinear three-dimensional flow in the lid-driven square cavity. *J. Fluid Mech.* **569**, 465–480.
- ALBENSOEDER, S., KUHLMANN, H. C. & RATH, H. J. 2001 Three-dimensional centrifugal-flow instabilities in the lid-driven-cavity problem. *Phys. Fluids* **13** (1), 121–135.
- ALVAREZ, J. & KERSCHEN, E. 2005 Influence of wind tunnel walls on cavity acoustic resonances. AIAA Paper 2005-2804.
- ALVAREZ, J., KERSCHEN, E. & TUMIN, A. 2004 A theoretical model for cavity acoustic resonances in subsonic flow. AIAA Paper 2004-2845.
- ARMALY, B.F, DURST, F., PEREIRA, J. C. F. & SCHÖNUNG, B. 1983 Experimental and theoretical investigation of backward-facing step flow. *J. Fluid Mech.* **127**, 473–496.
- BARKLEY, D., GOMES, G. M & HENDERSON, R. D. 2002 Three-dimensional instability in flow over a backward-facing step. *J. Fluid Mech.* **473**, 167–190.

- BAYLY, B. J. 1988 Three-dimensional centrifugal-type instabilities in inviscid two-dimensional flows. *Phys. Fluids* **31** (1), 56–64.
- BENSON, J. D. & AIDUN, C. K. 1992 Transition to unsteady nonperiodic state in a through-flow lid-driven cavity. *Phys. Fluids A* **4**, 2316–2319.
- BURNES, R. & COLONIUS, T. 2007 Cavity-enhanced mixing and flame-holding in high Reynolds number flows. work in progress.
- CAIN, A., D., RUBIO A., BORTZ, D. M., BANKS, H. T. & SMITH, R. C. 2000 Optimizing control of open bay acoustics. AIAA Paper 2000-1928.
- CATTAFFESTA III, L. N., GARG, S., KEGERISE, M. S. & JONES, G. S. 1998 Experiments on compressible flow-induced cavity oscillations. AIAA Paper 98-2912.
- CATTAFFESTA III, L. N., SHUKLA, D., GARG, S. & ROSS, J. A. 1999 Development of an adaptive weapons-bay suppression system. AIAA Paper 99-1901.
- CHANG, K., CONSTANTINESCU, G. & PARK, S. 2006 Analysis of the flow and mass transfer processes for the incompressible flow past an open cavity with a laminar and a fully turbulent incoming boundary layer. *J. Fluid Mech.* **561**, 113–145.
- CHATELLIER, L., LAUMONIER, J. & GERVAIS, Y. 2006 Theoretical and experimental investigation of low Mach number turbulent cavity flows. *Experiments in Fluids* **36**, 728–740.
- COLONIUS, T. 2001 An overview of simulation, modeling, and active control of flow/acoustic resonance in open cavities. AIAA Paper 2001-0076.
- COLONIUS, T., LELE, S. K. & MOIN, P. 1993 Boundary conditions for direct computation of aerodynamic sound. *AIAA J.* **31**(9), 1547–1582.

- DING, Y. & KAWAHARA, M. 1999 Three-dimensional linear stability of incompressible viscous flow using the finite element method. *Int. J. Num. Meth. Fluids* **31**, 451–479.
- DIPRIMA, R.C., EAGLES, P.M. & NG, B.S. 1984 The effect of radius ratio on the stability of Couette flow and Taylor vortex flow. *Phys. Fluids* **27** (10), 2403–2411.
- DRAZIN, P.G. & REID, W.H. 1981 *Hydrodynamic stability*. Cambridge University Press.
- FAURE, T. M., ADRIANOS, P., LUSSEYRAN, F. & PASTUR, L. 2007 Visualizations of the flow inside an open cavity at medium range Reynolds numbers. *Experiments in Fluids* **42**, 169–184.
- FREUND, J.B. 1997 Proposed inflow/outflow boundary condition for direct computation of aerodynamic sound. *AIAA J.* **35**(4), 740–742.
- FRIGO, M. & JOHNSON, S. G. 1997-2007 FFTW library <http://www.fftw.org>.
- FUGLSANG, D. F. & CAIN, A. B. 1992 Evaluation of shear layer cavity resonance mechanisms by numerical simulation. AIAA Paper 92-0555.
- GHARIB, M. 1983 The effect of flow oscillations on cavity drag, and a technique for their control. PhD thesis, California Institute of Technology.
- GHARIB, M. & ROSHKO, A. 1987 The effect of flow oscillations on cavity drag. *J. Fluid Mech.* **177**, 501–530.
- GLOERFELT, X., BAILLY, C. & JUVE, D. 2003 Direct computation of the noise radiated by a subsonic cavity flow and application of integral methods. *J. Sound Vib.* **266**, 119–146.
- GUDMUNDSSON, K. & COLONIUS, T. 2006 Linear stability analysis of chevron jet profiles. In *Proceedings of FEDSM 2006-98485*.

- HELLER, H. H. & BLISS, D. B. 1975 The physical mechanism of flow induced pressure fluctuations in cavities and concepts for their suppression. AIAA Paper 75-491.
- KEGERISE, M.A., SPINA, E.F., GARG, S. & CATTAFESTA III, L. N. 2004 Mode-switching and nonlinear effects in compressible flow over a cavity. *Phys. Fluids* **16** (3), 678–687.
- KRISHNAMURTY, K. 1956 Sound radiation from surface cutouts in high-speed flow. PhD thesis, California Institute of Technology.
- LARCHEVÊQUE, L., SAGAUT, P., LÊ, T. & COMTE, P. 2004 Large-eddy simulation of a compressible flow in a three-dimensional open cavity at high Reynolds number. *J. Fluid Mech.* **516**, 265–301.
- LARSSON, J., DAVIDSON, L., OLSSON, M. & ERIKSSON, L. 2004 Aeroacoustic investigation of an open cavity at low Mach number. *AIAA J.* **42**(12), 2462–2473.
- LEHOUCQ, R., MASCHHOFF, K., SORENSEN, D. & YANG, C. 1996–2007 ARPACK software <http://www.caam.rice.edu/software/ARPACK/>.
- LELE, S. K. 1992 Compact finite difference scheme with spectral-like resolution. *J. Comput. Phys.* **103**, 16–42.
- MAULL, D. J. & EAST, L. F. 1963 Three-dimensional flow in cavities. *J. Fluid Mech.* **16**, 620–632.
- NEARY, M.D. & STEPHANOFF, M.D. 1987 Shear-layer-driven transition in a rectangular cavity. *Phys. Fluids* **30** (10), 2936–2946.
- PODVIN, B., FRAIGNEAU, Y., LUSSEYRAN, F. & GOUGAT, P. 2006 A reconstruction method for the flow past an open cavity. *J. Fluids Eng.* **128**, 531–540.
- POINSOT, T. J. & LELE, S. K. 1992 Boundary conditions for direct simulations of compressible viscous flows. *J. Comput. Phys.* **101**, 104–129.

- PRESS, W. H., TEUKOLSKY, S. A., VETTERLING, W. T. & FLANNERY, B. P. 1992 *Numerical Recipes in Fortran (second edition)*. Cambridge University Press.
- RAMANAN, N. & HOMSY, G. M. 1994 Linear stability of lid-driven cavity flow. *Phys. Fluids* **6**(8), 2690–2701.
- RIZZETTA, D. P. & VISBAL, M. R. 2003 Large-eddy simulation of supersonic cavity flowfields including flow control. *AIAA J.* **41-8**, 1452–1462.
- ROCKWELL, D. & KNISELY, C. 1980 Observations of the three-dimensional nature of unstable flow past a cavity. *Phys. Fluids* **23** (3), 425–431.
- ROCKWELL, D. & NAUDASCHER, E. 1978 Review-self-sustaining oscillations of flow past cavities. *J. Fluids Eng.* **100**, 152–165.
- ROSSITER, J. E. 1964 Wind-tunnel experiments on the flow over rectangular cavities at subsonic and transonic speeds. *Tech. Rep.* 3438. ARC.
- ROWLEY, C.W. 2001 Modeling, simulation, and control of cavity flow oscillations. PhD thesis, California Institute of Technology.
- ROWLEY, C.W. & WILLIAMS, D.R. 2006 Dynamics and control of high-Reynolds-number flow over open cavities. *Annual Review of Fluid Mechanics* **38**, 251–276.
- ROWLEY, C.W., WILLIAMS, D.R., COLONIUS, T., MURRAY, R.M., MACMARTIN, D.G. & FABRIS, D. 2002a Model-based control of cavity oscillations, part ii: System identification and analysis. AIAA Paper 2002-0972.
- ROWLEY, C.W., WILLIAMS, D.R., COLONIUS, T., MURRAY, R.M. & MACMYNOWSKI, D.G. 2006 Linear models for control of cavity flow oscillations. *J. Fluid Mech.* **547**, 317–330.
- ROWLEY, C. W., COLONIUS, T. & BASU, A.J. 2002b On self-sustained oscillations in two-dimensional compressible flow over rectangular cavities. *J. Fluid Mech.* **455**, 315–346.

- SAROHIA, V. 1975 Experimental and analytical investigation of oscillations in flows over cavities. PhD thesis, California Institute of Technology.
- SHIEH, C. M. & MORRIS, P. J. 2000 Parallel computational aeroacoustic simulation of turbulent subsonic cavity flow. AIAA Paper 2000-1914.
- STANEK, M. J. 2005 A numerical study of the effect of frequency of pulsed flow control applied to a rectangular cavity in supersonic crossflow. PhD thesis, University of Cincinnati.
- SUPONITSKY, V., AVITAL, E. & GASTER, M. 2005 On three-dimensionality and control of incompressible cavity flow. *Phys. Fluids* **17-104103**.
- TAM, CHRISTOPHER K. W. & BLOCK, PATRICIA J. W. 1978 On the tones and pressure oscillations induced by flow over rectangular cavities. *J. Fluid Mech.* **89** (2), 373–399.
- THEOFILIS, V. 2003 Advances in global linear instability of non-parallel and three-dimensional flows. *Progress in Aerospace Sciences* **4**, 249–315.
- THEOFILIS, V. & COLONIUS, T. 2003 An algorithm for the recovery of 2- and 3D biglobal instabilities of compressible flow over 2D open cavities. AIAA Paper 2003-4143.
- THEOFILIS, V., DUCK, P. W. & OWEN, J. 2004 Viscous linear stability analysis of rectangular duct and cavity flows. *J. Fluid Mech.* **505**, 249–286.
- THOMPSON, K. W. 1990 Time-dependent boundary conditions for hyperbolic systems, II. *J. Comput. Phys.* **89**, 439–461.
- WARD, T. 1973 Slot cavitation. In *Cavitation and polyphase flow forum*. ASME.
- WILLIAMS, P. T. & BAKER, A. J. 1997 Numerical simulations of laminar flow over a 3D backward-facing step. *Int. J. Numer. Meth. Fluids* **24**, 1159–1183.